Origin of Th/U variations in chondritic meteorites

Thesis by
Julia S. Goreva

In Partial Fulfillment of the Requirements
For the Degree of

Doctor of Philosophy

California Institute of Technology
Pasadena, California
2001

(Submitted December 20, 2000)

Acknowledgments

I will not be able to thank everybody who filled the void around me during my tenure at Caltech. But I would like to point out several people who contributed the most to what I have become.

First of all, I would like to thank my adviser professor Don S. Burnett. I have enjoyed working with him during last few years immensely; I would not have become what I am now without his guidance and support. In particular, he formulated the problem this thesis is dealing with, and strategically maneuvered me through all my ups and downs with patience, technical expertise and always provided moral support. I thank him for exposing me to his unlimited enthusiasm and multi-faceted interests.

I would like to thank my other adviser, George R. Rossman, who introduced me to the mineral spectroscopy, and under whose supervision I have done work included at the end of this thesis as Attachments. I have benefited from his talent of being a navigator rather than a driver. I would like to thank George for his curiosity, for the spark in his eyes and his open door.

I am thankful to many people who have helped me out around various Caltech labs: Mihai Ducea and Jim Chen (radiogenic isotope clean lab), Ken Farley and Yaniv Dibowski (ICPMS), Paul Carpenter (electron microscopy), Liz Aredondo (mineral spectroscopy), and others.

Thanks to NASA grant NAG5-4319 for the financial support of the meteorite work, and to the White Rose Foundation for the support of the rose quartz work.

I have made a number of wonderful friends at Caltech, who brightened my days (years) here. But two of them became especially close to me and deserve special appreciation. I thank Ronit Kessel for hours of serious talks, meaningless chats and silly laughs. And for hundreds of gallons of coffee we had together. And I express my endless gratitude to Mihai Ducea, who has been for me a source of inspiration, support and encouragement. I thank Mihai for his friendship and love, and for becoming part of my life.

I thank my mother Natalia Goreva and my brother Georgiy Gorev for their optimism, constant support, and for letting me move to the other hemisphere in pursuit of my goals.

Finally, I would like to dedicate this thesis to my grandfather, Korolev Valeriy G., whose boundless devotion to science established three generations of geologists in our family.

Abstract

Isotope dilution thorium and uranium analyses of the Harleton chondrite show a larger scatter than previously observed in equilibrated ordinary chondrites (EOC). The linear correlation of Th/U with 1/U in Harleton (and all EOC data) is produced by variations in the chlorapatite to merrillite mixing ratio. Apatite variations control the U concentrations. Phosphorus variations are compensated by inverse variations in U to preserve the Th/U vs. 1/U correlation. Because the Th/U variations reflect phosphate sampling, a weighted Th/U average should converge to an improved solar system Th/U. We obtain Th/U=3.53 ($1_{-\mathrm{mean}}$=0.10), significantly lower and more precise than previous estimates.

To test whether apatite also produces Th/U variations in CI and CM chondrites, we performed P analyses on the solutions from leaching experiments of Orgueil and Murchison meteorites.

A linear Th/U vs. 1/U correlation in CI can be explained by redistribution of hexavalent U by aqueous fluids into carbonates and sulfates.

Unlike CI and EOC, whole rock Th/U variations in CMs are mostly due to Th variations. A Th/U vs. 1/U linear correlation suggested by previous data for CMs is not real. We distinguish 4 components responsible for the whole rock Th/U variations: (1) P and actinide-depleted matrix containing small amounts of U-rich carbonate/sulfate phases (similar to CIs); (2) CAIs and (3) chondrules are major reservoirs for actinides, (4) an easily leachable phase of high Th/U, likely carbonates produced by CAI alteration. Phosphates play a minor role as actinide and P carrier phases in CM chondrites.

Using our Th/U and minimum galactic ages from halo globular clusters, we calculate relative supernovae production rates for $^{232}Th/^{238}U$ and $^{235}U/^{238}U$ for different models of r-process nucleosynthesis. For uniform galactic production, the beginning of the r-process nucleosynthesis must be <13 Gyr. Exponentially decreasing production is also consistent with a 13 Gyr age, but very slow decay times are required (<35 Gyr), approaching the uniform production. The 15 Gyr Galaxy requires either a fast initial production growth (infall time constant <0.5 Gyr) followed by very slow decrease (decay time constant >100 Gyr), or the fastest possible decrease (≈8 Gyr) preceded by slow infall (≈7.5 Gyr).

Table of Contents

List of Tables

List of Figures

Chapter 1: Introduction

1.1 Background and motivation

The actinide elements (Th, U; Pu for meteoritic materials) are most famous because of the chronological applications associated with their radioactivity. This has the consequence that their unique and interesting chemical properties are often overlooked. In this work we re-emphasize actinide chemistry. We performed an analytical study to understand mechanisms of actinide element fractionation in meteoritic materials. In turn this enabled us to obtain a solar system Th/U with significantly improved accuracy for cosmochronological applications.

The relative abundance of Th and U is close to 3.7 (by atom) in a wide variety of planetary materials, resulting in this value as being regarded as a solar system constant.

Th and U are highly incompatible elements that are strongly depleted in the terrestrial upper mantle (e.g., Collerson and Kamber, 1999). In addition to overall depletion, both the lithospheric mantle and asthenospheric mantle can maintain domains with highly variable Th/U ratio, partial melting of which contributes to the variability of Th/U in the crust (Asmerom, 1999). Uranium has 2 common oxidation states (+4 and +6), whereas thorium has only one (+4). Therefore, oxygen fugacity as well as fluid content and magma composition affects the Th/U ratio (e.g., Keppler and Wyllie, 1990). As a result of these, and potentially other mechanisms, reported ratios for crustal igneous rocks vary greatly from at least as low as 1 in oceanic tholeiites to as high as 7 in a labradorite-andesine alkali basalt from Guadeloupe Island (e.g, Tatsumoto, 1966). Such a big spread in Th/U ratios makes it difficult to infer Th/U ratio of the bulk silicate Earth from crustal rocks.

Beyond merely assuming that the relative terrestrial abundances of refractory lithophile elements are chondritic, the principal evidence for the applicability of Th/U=3.7 for the bulk Earth comes from ^{208}Pb/^{206}Pb data beginning with Patterson (1955). From the ^{208}Pb/^{206}Pb ratio in a variety of ancient terrestrial rocks, the calculated Th/U ratio of the bulk Earth is 3.9±0.1 (Manhes *et al.*, 1979). The Th/U deduced from the lead isotope compositions of conformable lead ore deposits is 3.85 (e.g., Stacey and Kramers, 1975). Based on the Pb-isotope study of komatiites and ophiolites, Allegre et al. (1986) infer the Th/U ratio of the bulk silicate Earth to be 4.2.

The Th/U ratios in lunar rocks and regolith cluster strongly around 3.7 (Korotev, 1998). Because the Moon is an extremely dry and moderately reducing environment, the fO_2 effects on Th/U are minimal. Assuming only tetravalent U, the whole planet Th/U ratio is seen in crustal rocks.

The 9 samples of 5 different SNC meteorites show a range in Th/U from 3.75 to 4.4 (Chen and Wasserburg, 1985 and Chen et al. 1993). Given the apparently oxidizing conditions of Martian materials, it may be difficult to infer a Th/U for Mars from SNC meteorites. In April, 2001 the Mars Odyssey spacecraft will be launched with a gamma-ray spectrometer aboard. Because of the poor quality of the uranium data, the gamma-ray spectrometer will only obtain an average U and Th data for the Mars surface. The gamma-rays escaping into the space come from depths of at most several tens of g/cm^2, which is ~10 to 20 cm in a regolith (Boynton et al., 1992). Therefore, the Th/U average of the Martian surface will come mostly from the surface dust. Since the dust appears to be oxidized (i.e., red), we expect the Th/U ratio from Odyssey data to be lower than the actual mars Th/U.

The discussed evidence for the constancy of Th/U in a wide variety of planetary materials suggests a limited range of fractionation mechanisms, making it conceivable that an accurate average solar system ratio can be obtained.

Whole rock Th/U variations in carbonaceous chondrites

The CI carbonaceous chondrites are normally regarded as providing the best source of average solar system elemental abundances. Thus, Anders and Ebihara (1982) (later adopted by Anders and Grevesse,1989) based their estimation of Th and U solar abundances on CI chondrites, to a large extent on Orgueil, the most extensively studied CI meteorite. U and Th analyses used by Anders and Ebihara (1982) are mostly done by the neutron activation (NAA) technique, which has relatively poor accuracy for U and Th. Moreover, a significant number of data points were rejected. The mean chondritic Th/U ratio inferred from Anders and Ebihara's solar abundances is 3.7±0.4 (1σ).

Recent, high precision, analyses show surprisingly large, up to factor of 4, intersample variations in Th/U within CI type chondrites (Rocholl and Jochum;1993). These variations are unique to Th/U, and not seen in other refractory lithophile elements. Given these variations, use of CI compositions for precise U and Th solar abundances becomes questionable.

Rocholl and Jochum (1993) also noticed large variations in other groups of carbonaceous chondrites. These authors observed very interesting systematic decreases in Th/U with U concentrations for CI, CM2 and CV3 chondrites (Figure 1.1). Individual carbonaceous chondrite groups display similar trends in Th/U vs. U. In the sequence CI, CM, CV, there is a shift of the correlation curve towards higher U concentrations. Compared to CI chondrites, which display a concentration range of a factor of 6, CV chondrites show a much lower range of U of about a factor of 2 corresponding to smaller Th/U variations. Figure 1.1 shows high precision isotope dilution TIMS and SIMS analyses (filled symbols) as well as radiochemical neutron activation analysis (RNAA, open symbols).

Th/U variations in ordinary chondrites

Ordinary chondrites appear to have average solar abundances of refractory lithophile elements. Figure 1.2 (from Larimer and Wasson, 1988) is a plot of refractory lithophile element ratios versus the ratio of Al (refractory) to Si (more volatile). In this plot carbonaceous, ordinary and enstatite chondrites can be distinguished by Al/Si ratio, because the abundance of more volatile Si varies. But the refractory-element ratios plotted along the y-axis are constant within each group of chondrites to within ±15% total spread. The analyses presented in Figure 1.2 are collected by the same analyst, G.W. Kallemeyn, using INAA, and much of the scatter of the data is expected in bulk analyses obtained by this method. Refractory element ratios are remarkably constant within, as well as between, various chondrite groups. The average agrees with CI, which is accepted as the average solar value. The largest scatter in refractory-element ratios, observed in enstatite chondrites, probably reflects inhomogeneous samples, rather than refractory lithophile element fractionation. For ordinary chondrites, Sm/Al≈$2.74*10^{6}$(±8% total spread), Sc/Al≈$4.3*10^{4}$(±12%), Ca/Al≈74(±10%). Th and U are both refractory lithophile elements, so based on the arguments above, Th/U ratios of the bulk ordinary and CI chondrites should be the same and $Th/U_{OC}=Th/U_{solar}$.

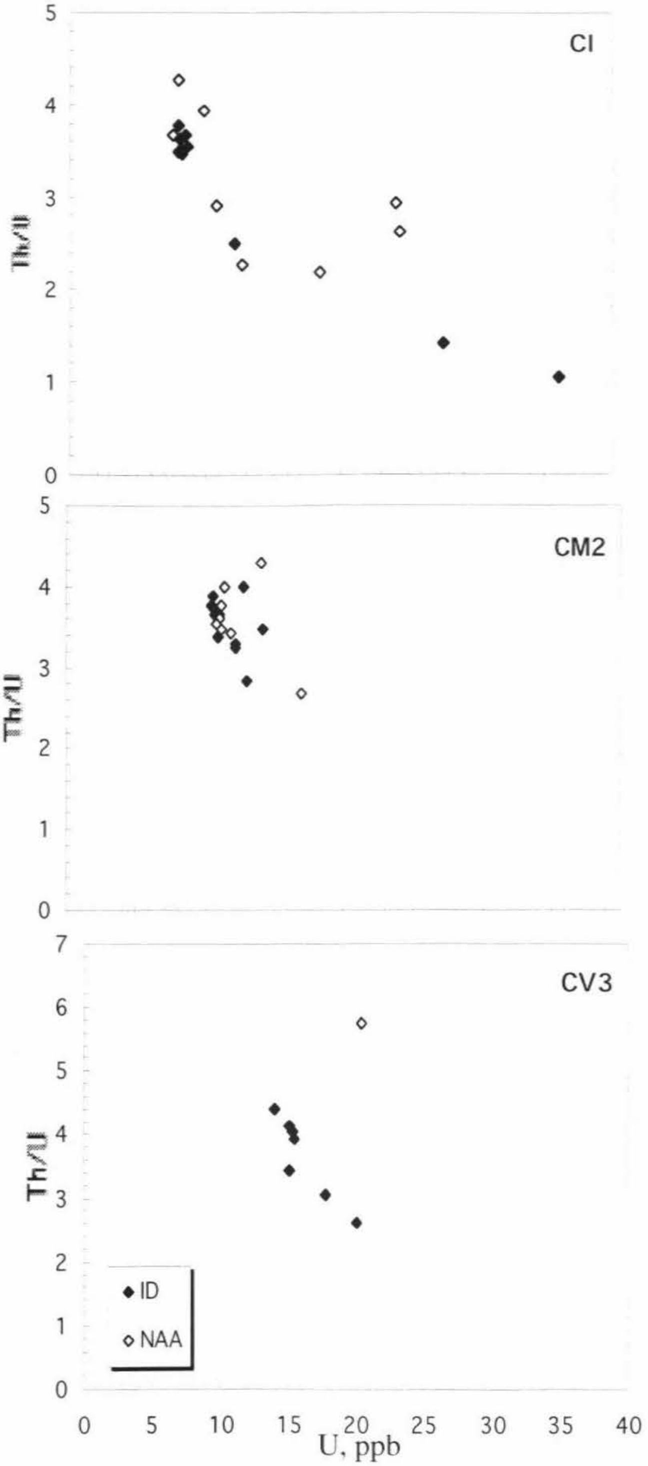

Figure 1.1 Th/U vs. U diagram for CI, CM2 and CV3 types carbonaceous chondrites. ID-isotope dilution TIMS, SIMS data from Rocholl and Jochum (1993), Tatsumoto et al. (1973,1976), Chen et al. (1993), Chen and Tilton (1976). All groups display negative correlation Th/U vs. U. In the sequence CI - CM2 - CV3, there is a shift of a correlation curve towards higher U concentrations.

Restricting the discussion to high accuracy measurements of Th/U in ordinary chondrites by isotopic dilution, prior to this work the literature data show a strong clustering of analyses around 3.6. However, 4 independent analyses of two L6 ordinary chondrites, Harleton and Glatton, show ratios around 6 (Unruh, 1982; Chen *et al*., 1993, and private communication) suggesting a bimodal distribution (Figure 1.3). The bimodal Th/U distribution is surprising for primitive materials such as chondrites, especially in light of Figure 1.2.

The objectives of the ordinary chondrite study are: (1) check the apparent bimodal distribution with additional high accuracy measurements of Th/U in ordinary chondrites, (2) understand the fractionation mechanisms causing the variations, (3) interpret the variations in terms of ordinary chondrite petrogenesis.

Unexplained intersample variations provide a quantitative measure of the uncertainty in estimates of solar abundances. Abundance variations for which the mechanisms are understood can be interpreted in terms of an original unfractionated set of solar abundances.

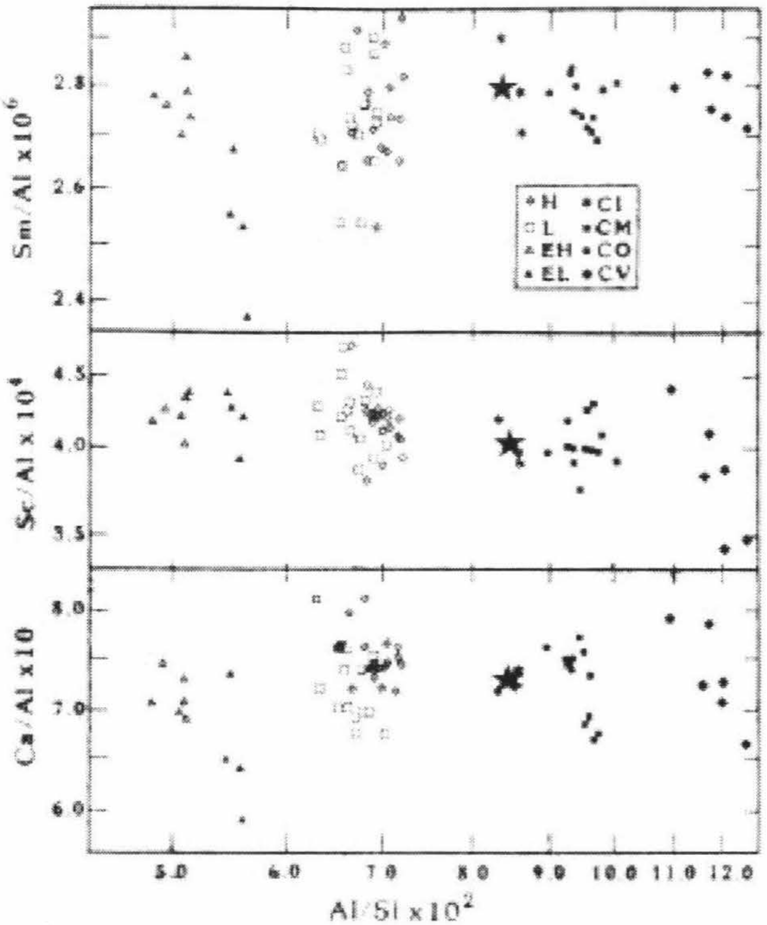

Figure 1.2 Refractory-element ratios, represented by element/Al ratios in chondrites (from Larimer and Wasson, 1988), based on the data by Kallemeyn and Wasson 1981, 1982, 1986.

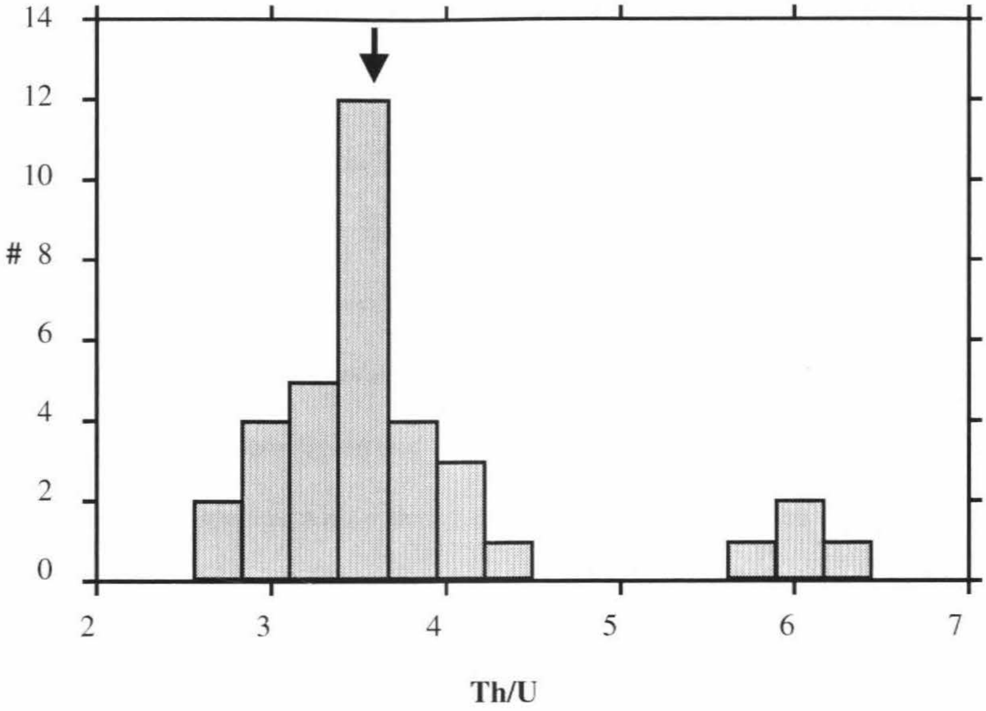

Figure 1.3 Whole rock ID Th and U literature data for ordinary chondrites, showing bi-modal distribution of Th/U ratio. Arrow indicates Anders and Grevesse (1989) value.

Nucleochosmochronlogy models

Why do we need to establish more precise relative Th and U abundances in the solar system?

In the classic paper on nucleosynthesis by Burbidge, Burbidge, Fowler, and Hoyle ("B2FH," Burbidge et al. 1957), it was recognized that a model age for the galaxy could be derived from the solar system Th/U and $^{235}U/^{238}U$. The rephrasing of the problem as "cosmochronology" recognizes that there both the age of the galaxy and the time dependence of the rate of r-process nucleosynthesis are involved.

Assuming the time interval between the termination of galactic nucleosynthesis inputs into the solar system region and the formation of meteorites is negligible, for every nuclear radioactive species with a decay constant λ_i, the abundance N_i at time T (time before the formation of the Solar system) is defined as a solution of the growth equation:

$$N_i = \int_0^T P_i(t) e^{-\lambda_i (T-t)} dt .$$

There are two unknowns in the equation above: net production "history," or change in the production rate with time (representing supernova input to the interstellar medium and loss of mass in star formation), and T. Considering two ratios of two species, such as $^{235}U/^{238}U$ and $^{232}Th/^{238}U$, one would have two equations with two unknowns, setting constraints on T and $P_i(t)$, although $P_i(t)$ can have several parameters.

Schramm and Wasserburg (1970) (summarized in Podosek and Swindle, 1988) showed that long-lived isotopes define a "mean age of the elements," regardless of the time-dependent model used, i.e., the average time of production from the beginning of the galaxy to 4.55 Gyr ago.

This is an important result, but cosmochronology modeling has continued because of the interest in the age of the galaxy and the r-process production rates separately.

All models are quite sensitive to the assumed solar system Th/U abundance ratio. The reason for the sensitivity is that the r-process Th/U production rate ratio is $P_{232}/P_{238} \approx 1.9$ (Podosek and Swindle, 1988), whereas 4.6 Gyr ago the solar system Th/U abundance ratio was 2.3 (assuming 3.8 today). All of galactic evolution is tied up in the difference between 1.9 and 2.3. The precision of the calculated relative production rates (order of 30% for the uranium ratio and 15% for the Th/U ratio) makes it difficult to distinguish between different models. However, in light of a new, improved Th/U solar system ratio we are able to test the compatibility of different models, specifically with different estimations of relative production rates.

1.2. Thesis outline

This thesis has been organized in six chapters, including this introduction; two other chapters were written as separate manuscripts and included as Appendix 1 and 2.

Chapter 2 describes sample preparations and analytical techniques used in this study. Chapter 3 presents results for the study of uranium and thorium distributions in equilibrated ordinary chondrites, proposing a new, improved solar system Th/U ratio. Most of this chapter is a manuscript in press, to be published in the January 2001 issue of *Meteoritics and Planetary Science*. Chapter 4 is a study of actinide distributions in carbonaceous chondrites. Its main focus is leaching experiments, aimed to distinguishing the carrier phases for U, Th and P. Chapter 5 discusses different nucleocosmochronological models in light of an improved Th/U ratio.

Appendices I and II contain the results of a project unrelated to the main subject of this thesis, a study, that started as a part of the qualifying exam requirements in the Division of Geological and Planetary Sciences at Caltech. This work was done under the supervision of Dr. George G. Rossman. Appendix I presents Part I of the study of nanofibrous inclusions in the massive rose quartz, resolving a long-standing problem of the source of rose quartz coloration. This Appendix is a manuscript in press, to be published in the *American Mineralogist*, April 2001. Appendix II addresses questions, raised in the Appendix I, by performing detailed single-crystal HR-TEM and AEM study of the structure of this nanofibers, determining a new phase, the polymorph of dumortierite. This manuscript is Part II of the rose quartz study, yet to be submitted to the American Mineralogist.

Chapter 2: Analytical techniques

2.1 Sample preparation

In this work whole rock analyses as well as leaching experiments of meteorites were performed. Following the method of Shinotsuka and Ebihara 1997, we performed inductively-coupled mass spectrometry (ICPMS) analyses on dissolved samples without chemical separation of U and Th even though our samples were up to 100x larger than these authors. In addition, we used the isotope dilution method to increase the precision of our results. A detailed procedure for the sample dissolution is described below. Procedures for the leaching experiments are described in the Chapter 4 for specific applications.

Chips of chondrites, usually weighing about 1 gram, are surface cleaned with a dental drill, ultrasonically cleaned in spectroscopic grade methanol, and crushed to submillimeter grain size with stainless steel tools. Sample handling is done in a laminar flow clean bench. Chemical procedures are carried out in the geochemical clean lab of J. Saleeby. Spike amounts are estimated to give $^{232}Th/^{230}Th$ and $^{238}U/^{235}U$ ratios around 1. Procedural blanks are run with each set of samples. For dissolution, samples are mixed with a $^{230}Th+^{235}U$ spike solution and treated for 10 hours in a 30 cc open Teflon beaker with a mixture of concentrated acids (10 ml HF, 2 ml HNO_3 and a few drops of $HClO_4$) at room temperature. The beaker is heated on a hot plate at 150^{O}C with a screw-cup on, periodically hand shaken until the solution is clear. This step usually takes 3 to 4 days. The solution is evaporated to a thick paste and taken up with 10 ml 10% HNO_3. To assure dissolution, the sealed beaker is ultrasonically agitated for 10 min and then heated on a hot plate (80°C) for 1 hour. The solution is centrifuged. After $HF+HNO_3+HClO_4$ treatment, there is always a visible solid residue, fine metallic black specks of, presumably, chromites. The residue is treated with 0.5 ml conc. $HClO_4$ in an open Teflon beaker at room temperature for 10 hours. The walls of the beaker are washed with H_2O, evaporated almost to dryness, and the residue dissolved in a known amount of 10% nitric acid.

All final solutions were combined and diluted to 20ml 10% HNO3. For ordinary chondrites, this gives solutions of about 0.5 ppb U and 2 ppb Th. Amounts of spike and standard solutions are measured both gravimetrically and volumetrically. Amounts of reagents are measured volumetrically with digital pipettors, so that the final 20 ml volume is accurately (on the order on 1-2%) known.

The mixed Th-U spike was calibrated against two different commercial standard solutions (^{235}U-depleted) as well as natural U solution (courtesy of J.Chen). Results from the different standards agreed to within 1 %. Table 1.1 presents U+Th mixed spike concentrations.

Table 1.1 U and Th mixed spike concentrations.

Isotope	Concentration, ng/g
^{230}Th	17.03
^{232}Th	1.509
^{235}U	3.265
^{238}U	0.0052

Uncertanty is <1% 1σ for masses 230, 232 and 235; ~3% for mass 238.

A standard solution (Specpure® Alfa ÆSAR) is always analyzed along with the spiked samples, giving independent measurements of U and Th concentrations. Agreement of the Th analyses is usually better than a few percent. This suggests that co-precipitation losses of other unspiked lithophile elements are not important. Over the period of 3 years, changes in concentrations of standard solutions where not observed based on the periodic analyses freshly mixed standard and spike solutions.

Procedural blanks (contamination from acids used for digestion plus sample handling), were measured using the same mixtures of concentrated acids as for samples. These were evaporated and re-dissolved in 7% nitric acid for analyses. The procedural blanks are at the level of the background 7% HNO_3 solution ($\approx$10ppq, corresponding to ~10^{-13} g, negligible).

Reagents

Spectroscopic grade methanol was used for cleaning of the samples and as a cutting lubricant. The cleanest commercially available concentrated nitric (HNO_3), hydrofluoric (HF), hydrochloric (HCl), perchloric ($HClO_4$) and acetic (HAc, CH_3CO_2H) acids (Seastar Chemicals Inc., Th, U<0.001ppb) were used at every step of the sample preparation. For diluton, 4x distilled, 2x deionized H_2O (Bi-18, from D.A. Papanasstassiou, Caltech) was used. Ammoniacal EDTA (ethylenediaminetetraacetate, $(-O_2CH_2)_2NCH_2CH_2N(CH_2CO_2-)_2$), used in the leaching experiments, was prepared by adding EDTA acid powder, to the 0.1M NH_3 solution (concentrated Seastar HN_3 diluted with Bi-18 H_2O) until pH = 9.

2.2 Inductively coupled mass-spectrometry

Atomic emission spectrometry, using the inductively coupled plasma source (ICP-AES) was extensively used for multi-element analysis at trace levels at the end of the 1960s. However, soon it was recognized that AES analysis of trace elements in rock samples presents a number of problems because of insufficient sensitivity. For example, REE are measured using a time-consuming cation separation and preconcentration procedure. These problems stimulated a search for alternative methods of trace element analysis, while preserving the ease of sample introduction and speed of analysis of ICP-AES. Spark source mass spectrometry (SSMS), based on analyzing ions from the application of a discharge to a solid sample, was already extensively used for trace element analysis, but relatively poor precision, and low sample turnaround rates made it clear that a new ICP technique with higher ion pressures was required for adequate analysis. It appeared that an inert gas plasma might prove to be a good ion source (Gray, 1989 for review).

In ICPMS, the sample is introduced to a region where the gas temperature is approaching 10,000 K, increasing the degree of ionization of even elements with high ionisation potentials. Positive ions, generated in the plasma, are extracted via a differentially pumped gas-vacuum interface, into a mass analyzer designed to scan a wide mass spectrum very rapidly.

Since the introduction of the first commercial inductively coupled mass spectrometry (ICP-MS) instruments in 1983, the technique has gained rapid and wide acceptance for the analysis of geological, environmental, medical, biological and industrial samples. Measurements can be made rapidly and with minimal sample pre-treatment, making the technique both cost effective and versatile.

An ICP mass spectrometer for aqueous solution analysis is shown schematically in Figure 2.2.1. The sample solution is continuously pumped into the inlet system. The flow of the solution into and out of the inlet system is usually controlled by peristaltic pumps. The solution passes into a nebulizer that disperses the sample using a stream of argon gas. A sample solution mist forms and passes through a spray chamber, where the larger sample droplets are removed by collision with chamber walls. A drain pump constantly removes excess sample solution. The sample aerosol passes from the spray chamber into the center tube of a horizontally mounted ICP torch consisting of three concentric quartz tubes. The end of the torch is situated inside the 4-turn load coil, through which a radio frequency current is passed. The outermost concentric tube of the torch carries the plasma gas (argon). Conduction in the argon gas is initiated with a high-voltage spark, allowing energy to be transferred from the coil to the torch. The RF magnetic field produced by the coil causes oscillatory motion of free electrons within the argon gas. Further collisions of electrons and Ar atoms within the intense RF field produces additional ionization generating an approximately steady-state argon plasma. In the center of the plasma, the temperature ranges from 8,000 to 10,000 K. The carrier gas flows through the innermost tube of the torch and delivers the sample to the plasma. This gas supply is mass flow controlled, which contributes to good signal stability. The sample aerosol is instantaneously ionized. Argon plasmas are good source of positive ions (mostly singly charged) and over 60% of the elements have an ionization efficiency of greater than 97%. The differentially pumped interface region, which transmits ions from the atmospheric pressure plasma into the mass spectrometer, consists of two co-axial conical apertures (made of nickel or platinum), the sampling cone and the skimmer cone. This set of cones allows ions to pass into mass spectrometer, leaving behind most of the uncharged particles. The region between the cones is evacuated by a rotary pump, whereas turbo pumps maintain high vacuum in the focusing region behind the skimmer.

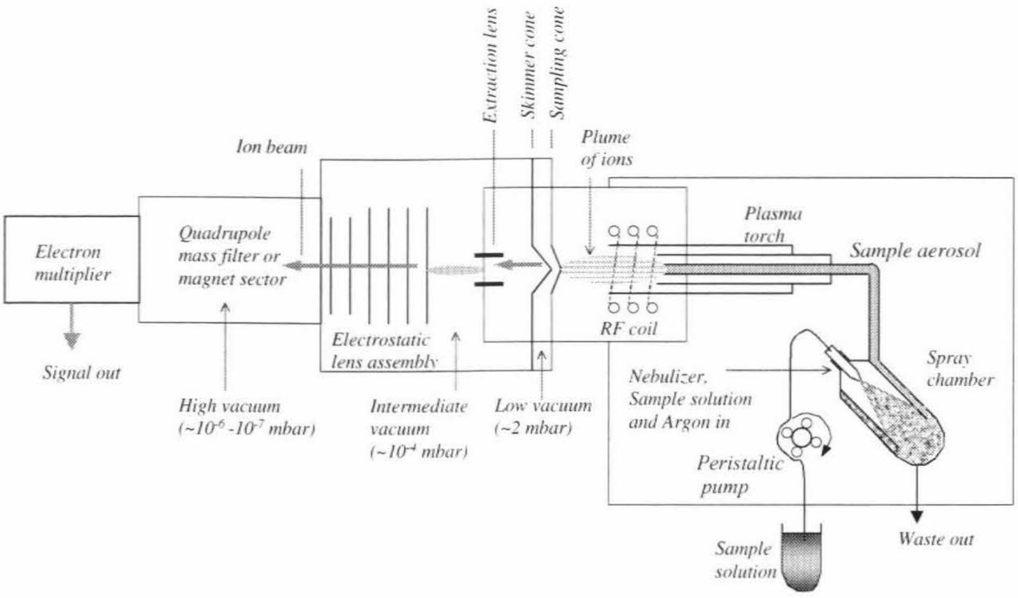

Figure 2.2.1 Schematic of an inductively coupled plasma-mass spectrometer.

Quadrupole ICPMS

The rapid scan rates of ICPMS with quadrupole mass analyzer allows near-simultaneous determination of most elements in the periodic table at levels down to 10 pg/ml.

A diagram of a typical quadrupole mass filter is shown in Figure 2.2.2. In a quadrupole analyzer, mass separation is achieved solely by electric fields. The analyzer has a hyperbolic cross section and consists of four metal rods parallel and equidistant from the axis. Opposite pairs are connected together, and to each pair a potential $U+U_1\cos(2\pi\upsilon t)$ with opposite polarities, is applied (see Fig. 2.2.2a). The direct current voltage (DC) is positive for one pair and negative to another. The radio frequency (RF) voltages on each pair have the same amplitude but are opposite in sign (i.e., they are 180^o out of phase). By varying these voltages, the rods act as a mass filter, allowing only ions of a specific-to-charge ratio to pass through the center of a quadrupole at any given combination of applied voltages (Fig. 2.2.2b). All other masses are unstable and collide with the rods. These voltages are ramped very rapidly so the quadrupole can scan the whole mass range (2-260 m/z) in 100 milliseconds.

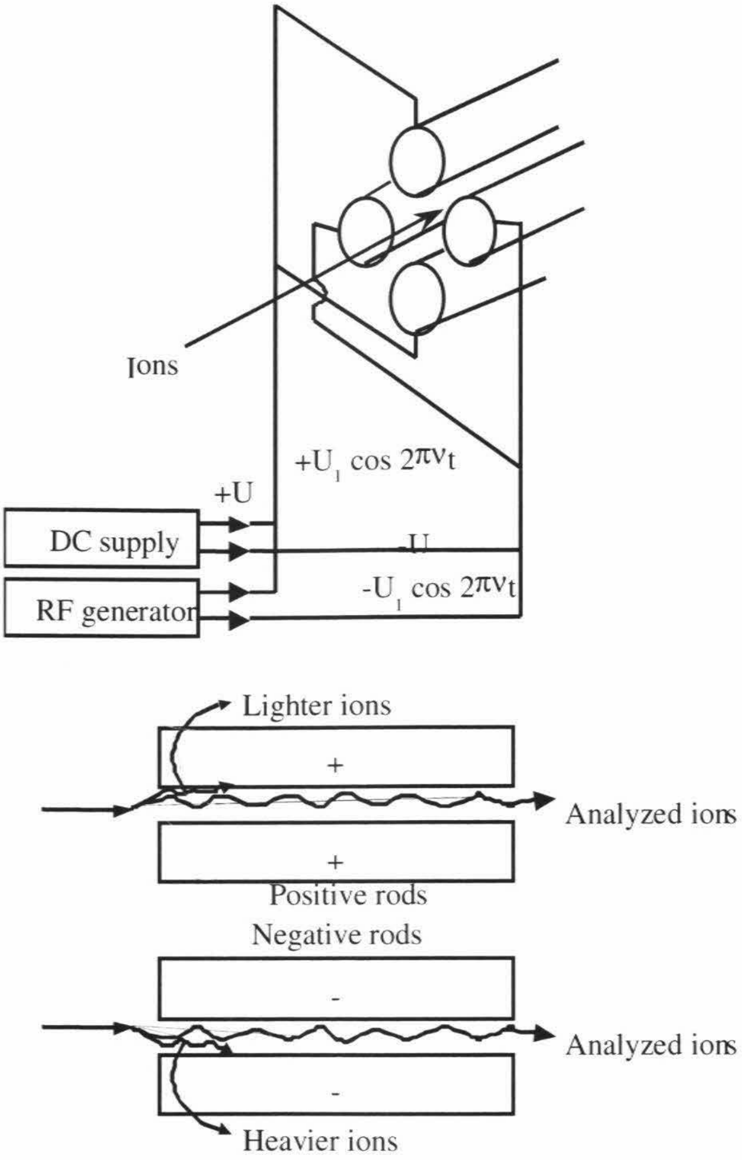

Figure 2.2.2 a) Schematic of a quadrupole mass filter. U is a fixed direct current (DC) potential (up to 70 volts) and U_1 is the peak amplitude for a radiofrequency (RF) potential (maximum of about 400 volts) of frequency υ (typically 2 MHz); b) Illustration of the ion paths in each of the two rod planes. In the positive rod plane quadrupole acts like a high-pass mass filter, in the positive plane – like a low-pass mass filter. Since high-pass and low-pass filtering are superimposed, the two form a system that transmits ions only at the m/z of interest to the detector. Modified from Jarvis (1997).

Quadrupoles are limited effectively to unit mass resolution so they can't resolve polyatomic or isobaric inteferences. However, of all of the elements detectable by ICP-MS, only indium does not have an isotope that is free from overlap by another element.

After passing through the quadrupole, ion currents of a specific m/z ratio are measured by an electron multiplier detector. Depending on the concentration of the analytes being measured, the detector operates in two modes: the pulse count mode for concentrations ranging from detection limit to ~1ppm in solution, and the analog mode for concentrations between 1 and 100 ppm.

Single collector magnetic sector ICPMS

Since the introduction of the first commercial system for ICP-MS employing a quadrupole filter as mass analyzer, the problem of spectral interferences (molecular and doubly charged ions) has always been a significant impediment, because the unit mass resolution of quadrupoles is not sufficient to separate the ions from interfering species.

The most straightforward approach to overcome limitations from spectral interferences is the application of higher mass resolution by focusing both energy and angle of the ion beam in the magnetic sector field mass-spectrometers.

2.3 Instrumentation used in this work

HP 4500 ChemStation Quadrupole mass spectrometer

The HP 4500 is one of the most stable, accurate, and sensitive of the current commercial single-quadrupole ICP-MS instruments. It can detect as little as 1ppt (by mass) of an element in solution and as much as 1ppm of most metals without significant deadtime counting losses and can do this in one minute. For routine quantification 1-1000 ppb is the usual working range.

The HP 4500 features the Babington-type nebulizer, in which the analyte solution runs down a narrow V-shaped groove. The aerosol is produced when solution passes over a small hole in the bottom of the grove, through which argon gas flows at high pressure. A Peltier cooler cools the spray chamber, enabling the temperature inside the chamber to be precisely controlled, which gives the HP 4500 a very stable ion signal.

HP4500 Tuning for U and Th analyses

To achieve high signal sensitivity, the ion beam extracted from the plasma must be focused before entering the quadrupole mass analyzer. The quadrupole and detector are mounted off-axis to the ion beam entering the system from the interface, preventing photons and neutral species from reaching the detector thus giving the HP 4500 a very low random background resulting in high detection limits. The ions are focused into the analyzer, where they are separated by their mass-to-charge ratio (m/z).

Although it is not necessary to tune HP 4500 daily for many applications, in this work optimization was performed routinely to achieve optimum sensitivity.

Optimization of instrument performance consists of tuning for: (1) sensitivity, (2) reducing oxide ions, (3) reducing doubly charged ions, and (4) adequate mass resolution. Within the tuning windows of the HP 4500 ChemStation software, one can adjust parameters for the sample introduction rate, torch box, analyzer and detector systems.

Sensitivity is strongly dependent on the sample uptake rate, carrier gas flow, temperature of the spray chamber (2°C for aqueous samples), radio frequency power, and sample "depth" (distance between the edge of the load coil and the tip of sampling cone). Tuning for the highest sensitivity almost inevitably increases the level of oxide/hydroxide or doubly charged ions. To reduce the level of *oxides*, key factors are plasma temperature, lower sample introduction rate, lower carrier gas flow and longer residence time for ions in the plasma (sample depth) produced by increasing distance between end of the torch and the sample cone. The level of *doubly charged* ions is anticorrelated with the amount of oxides, so a compromise must be reached for higher sensitivity within acceptable limits of polyatomic compounds and doubly-charged ions. For the mass 230-240 region, there is no evidence for molecular interferences. Using a mixed Th and Ba solution, the instrument was tuned to have counting rates of oxides/hydroxides and doubly charged ions in the plasma below 1 and 2 percent respectively.

For most applications the HP 4500 is optimized using a tuning solution with a few elements covering the whole range of masses, assuring good sensitivity at all masses simultaneously. However, for this study the HP4500 was optimized using a 1 ppb uranium standard solution to obtain maximum count rates, usually on the order of 1600 cps for both U and Th. There is a tradeoff between sensitivity, mass resolution, and shape of the peak. The width of every peak is adjusted to give good *resolution* for adjacent masses. For sufficient resolution, the peak width at 10% of a peak height for all masses should be 0.65-0.8 AMU and a peak center should be within 0.1 of the selected mass. Depending on the mass analyzed and tuning parameters, the top of the peak can be made flat to within a few percent for four voltage steps. In this work, for quantitation of U and Th, counts are taken for 3 voltage points on the peak top to provide a single mass peak intensity reading. Exploiting the rapid scan capabilities of the quadrupole to minimize the effects of drift, each mass peak is counted for 0.3 sec (0.1 sec. per voltage point). A data block of 5 such measurements is averaged, and the counting rates and ratios of average counting rates (232/230 and 238/235) tabulated. For such blocks, drift in the intensity is not important. For our work 40 such data blocks have been taken for a given sample, which consumes about 3 cc of solution or about 15% of the sample, leaving the remainder for analysis of other elements in the same solution. The distribution of ratios from the blocks appears normal, with a standard deviation only slightly above that expected from counting statistics, justifying the calculation of an error of the mean for all the data.

Counting rates for pure HNO_3 for masses 230, 232, 235, 238, as well as for masses 231, 233, 234, 236 and 237 are roughly 4 cps. Background corrections are made from counts at masses 230, 232, 235, and 238 from the 7% HNO_3 carrier solution. Counting rates for heavy (e.g., > REE) elements are about the same as for U and Th, but for light elements (masses <56) re-tuning of the instrument is needed for optimum performance.

Instrument drift is initially about 3% per hour, but after first 1.5-2 hr. of work, drift becomes undetectable. Sample and standards can be switched in about 7 minutes in programmable sequences, enabling good precision for analyses comparing counting rates between sample and standard. Of the 7 minute intersample time, 5 minutes are spent for washing the machine with pure 7% HNO3. This time is shown to be sufficient to bring the counting rates to the background level after analysis of 1 ppb sample solution.

Typical observed standard deviations for ^{232}Th/^{230}Th and ^{238}U/^{235}U are <1.5%. Instrumental mass fractionation correction was made on the basis of measurements of an isotopically normal U solution on three separate days. The correction of 0.5% per amu was applied to both ^{230}Th/^{232}Th and ^{235}U/^{238}U.

ELEMENT Finnigan MAT HR-ICP-MS

A diagram of this single collector ICPMS is shown in the Figure 2.3.1. The mass spectrometer consists of post-extraction focusing lens system, the magnet sector, the electrostatic analyzer and the electron multiplier.

Sample is introduced into the spray chamber through the nebulizer. In this work both standard pneumatic (Meinhardt) and self-aspirating microconcentric nebulizers (CETAC MCN-100; Figure 2-3-2) were used. The Meinhardt is essentially two concentric tubes. Through the inner one the sample solution is introduced with a help of peristaltic pump. Through the outer one Ar gas is supplied. To achieve maximum sensitivity, the flow rate through the Meinhardt should be approximately 1 ml/min. The MCN-100 consists of a PVDF body with a Teflon nebulizer capillary and a sapphire nebulizer insert. The MCN-100 is a self-aspirating nebulizer. Argon gas flow produces the vacuum which drives the sample solution into the nebulizer. The MCN-100 offers benefits of low sample uptake with high fraction of the solution injected into the plasma.

With flow rates of only 30 μl/min, the MCN-100 can provide the detection limits of a pneumatic nebulizer. Using the MCN-100, analyses can be performed on small volume (less than 1ml) samples. The decrease in the amount of sample analyzed combined with high sensitivity of ICPMS translates into small sample consumption, allowing for the analyses of wide range of elements in the same sample aliquot.

The beam of plasma with ionized sample passes through the cones, extraction lens, and a set of focusing and shaping (to a line) lenses before entering the flight tube through the entrance slit. The beam then becomes the source for the analyzing system which, in turn, focuses the beam on the exit slit (see Figure 2.3.1 for diagram).

The *ELEMENT* system has an inverse Nier-Johnson geometry, i.e., the magnet is located in front of the electrostatic analyzer (ESA). The *ELEMENT* has been designed for multi element analysis in low, medium, and high resolution mass modes. The electrostatic analyzer (ESA) focuses the ion beam both in angle and in energy. Mass resolution of the analyzer is accomplished by means of two mechanical slits, one at the entrance (source- or entrance-slit) and one at the exit (detector- or exit-slit) of the ion optical system (see Figure 2.3.1). The smaller entrance slits are used for higher resolution modes. Analyses are possible with the use of different resolution modes for different masses in the same sample. Time delay for the switch of the resolution slits is approximately 0.3 sec, so for muli-resolution analyses it is more convenient to scan all the masses at one resolution, then switch slits, and measure all the other masses. The peak shapes produced by the *ELEMENT* are either triangular (medium or high mass resolution) of flat-topped (low mass resolution). The mass range extends from 2 to 260 amu.

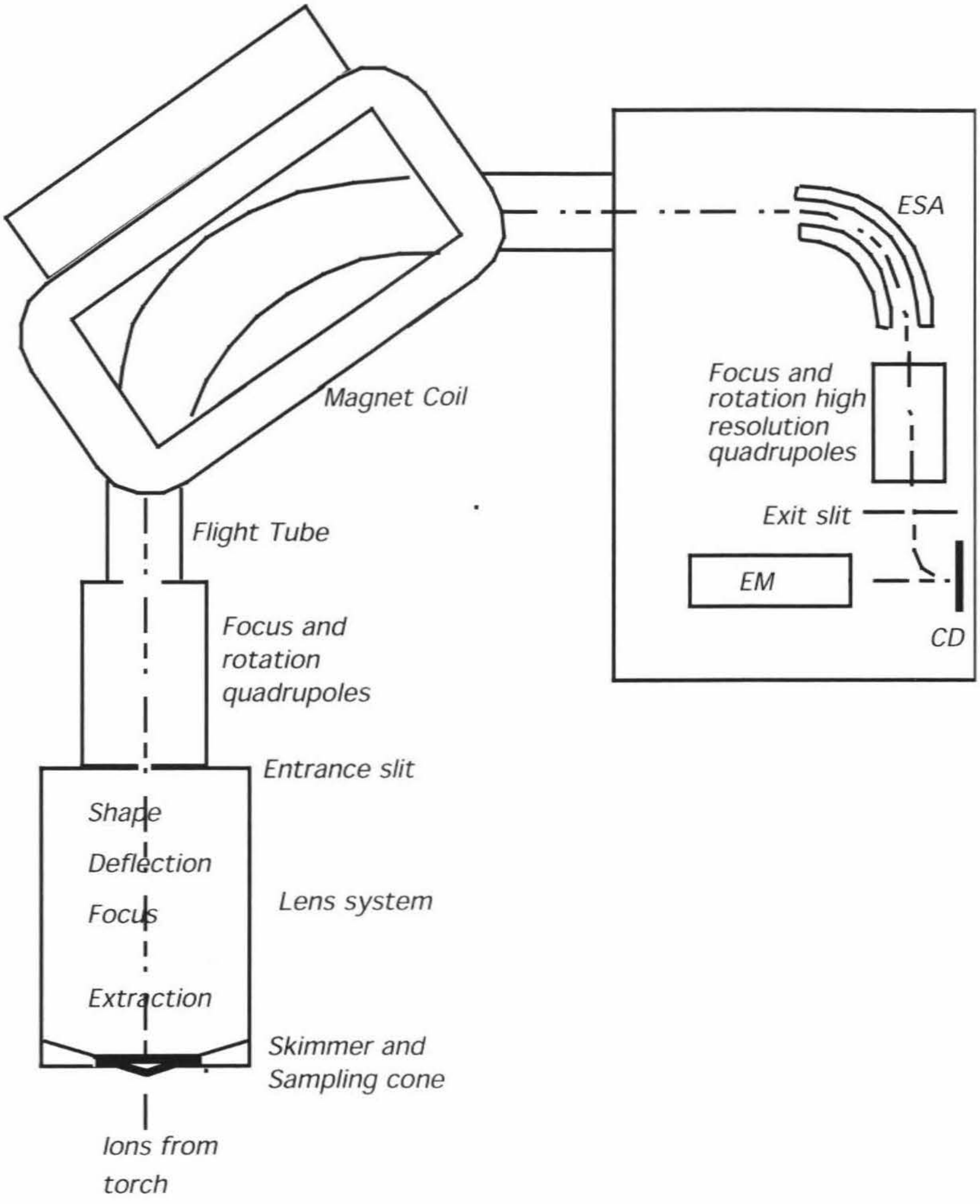

Figure 2.3.1 Schematic diagram of Element ICPMS. ESA- Electrostatic Analyzer; CD - Conversion Dynode; EM - Electron Multiplier. Modified from Element Operating Manual, Revision A.

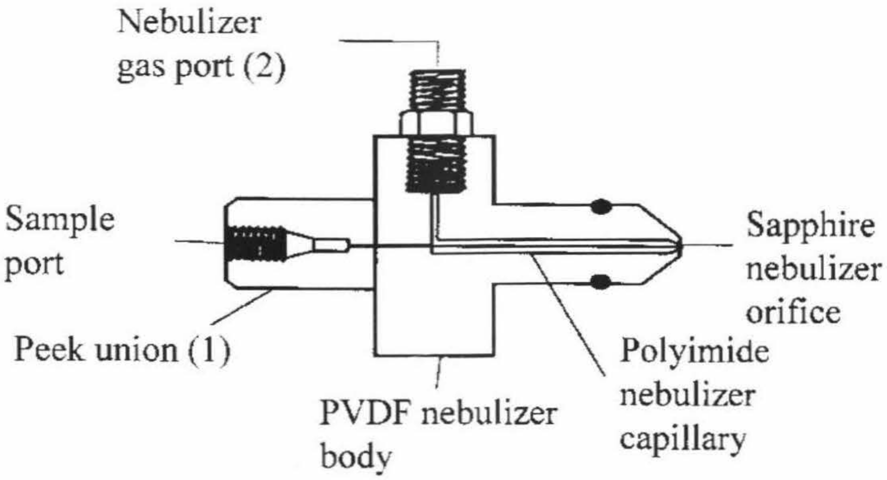

(1) Used to attach the polyimide nebulizer capillary to the sample tubing
(2) Used to connect the nebulizer gas supply from the ICP instrument to the MCN

Figure 2.3.2 CETAC microconcentric nebulizer (MCN-100).

Finnigan *ELEMENT* HR-ICPMS U and Th analysis

The instrument was optimized using a multi-element 1 ppb solution for occasional mass calibration and 1 ppb Indium solution for everyday tuning for sensitivity. Routine tuning includes sample gas flow, lens parameters and plasma power tuning for maximum sensitivity, and plasma parameters for minimum multiple ionisation and minimum molecule-generation. The sensitivity is the highest for high masses (i.e., for U). This is because light masses tend to be deflected from a straight trajectory upon passing through the cones.

U and Th analyses were obtained using low resolution mode of the *ELEMENT*. The resolution R of *ELEMENT* is defined by the peak distance A between ^{56}(ArO) and ^{56}Fe: $R = \frac{2500 * A}{B}$, where B is the width of the ArO peak at 5% height. For low resolution, R=300, which is much higher than the mass resolution of the quadrupole ICPMS. The counting rate for the 1 ppb In solution is ideally 10^6 counts per second (cps) for both nebulizers used in this study. The sensitivity over the whole mass range spans between 10,000 cps for 1 ppb Li and $2*10^6$ for U. Dark noise is usually 0.1 cps.

The only molecular interferences expected for the masses of interest in this study are platinum argides. The most abundant is $^{195}Pt^{40}Ar$, interferring with ^{235}U. After tuning the machine for minimum oxide/hydroxides (on the order of $BaO/Ba^+ \approx 0.003$), there is no evidence of significant input of PtAr in the peak of mass 235.

Masses 230, 232, 235 and 238 are measured using electrostatic scans with the magnet sitting at the lowest mass. At low resolution, peaks have a flat top. Figure 2.3.3 illustrates a U peak at mass 238. An average of 50 scans with 100 point steps was taken over the whole width of the ^{238}U peak. For analyses, 10 point steps were taken over only the central 10% of the peak width for each of the 4 masses. Each point step was scanned for 0.01 second, or 0.1 sec per peak. One scan consist of 4 measured masses; 49 such scans were performed, with a total analysis time of T=4*0.1sec*49+peak shift time < 1 min. Typical standard deviation for measured 232/230 and 238/235 ratios is a few permil. Corrections for instrumental mass fractionation were based on the measurement of the 238/235 ratio in the normal U solution. Typical correction is 0.5% per amu. The background level from the HNO_3 solution is usually < 10 ppq for all masses.

Isotopic ratio analyses of the same samples with the HP quadrupole ICP and *ELEMENT* sector ICP agree within the uncertainty.

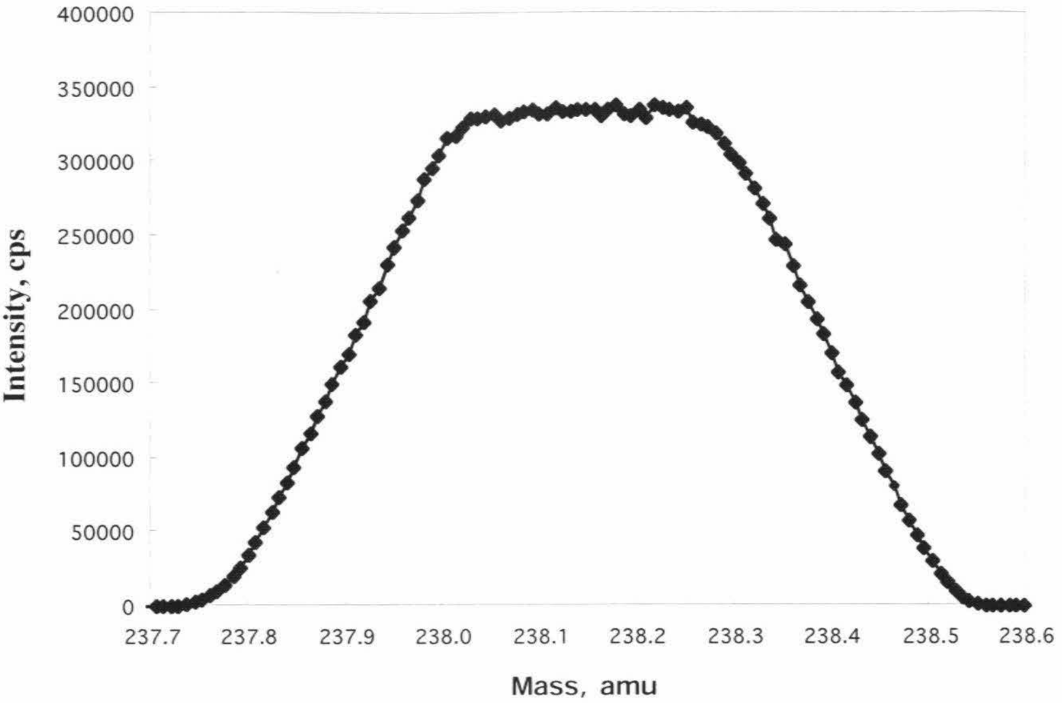

Figure 2.3.3 Low resolution electrostatic scan of the ^{238}U peak, illustrating flatness of the peak top. 50 scans were collected with a 100 point steps in every scan.

Finnigan *ELEMENT* HR-ICPMS P analysis

Phosphorus analyses were done with the Finnigan magnetic sector single collector ICPMS. Medium resolution (4000) was used in order to resolve the ^{31}P peak from $^{15}N^{16}O$ and $^{14}N^{16}O^{1}H$ (Figure 2.3.4). At medium resolution, the shape of P peak is triangular. Counts were taken stepping over a range of 0.01 amu, centered at the P peak, wich covers >100% of the P peak width at the base. 100 point counts per scan were taken, and 100 scans were performed. *ELEMENT*'s software is programmed to find top of the peak for each scan. The 100 scans were averaged and 30% of the peak top was integrated.

It was found necessary to use the method of standard addition for phosphorus analyses to avoid matrix effects. Three aliquots of the sample were analyzed, one with no P added, one with a known added amount of P approximately equal to the sample solution and one twice as much. For quantitative analysis, the sample solution and the two P-spiked sample solutions must produce a linear calibration trend.

Preliminary results showed that the common standard addition method does not produce satisfactory results. Figure 2.3.5 shows that, although the three sample solutions follow a general positive trend, the linear fit is not good. This is probably due to ion beam current instability. To avoid this effect, as well as other processes affecting counting rates, Cs was added as an internal standard to all analyzed solutions. Since the sample solutions contain high concentrations of Mg, ^{25}Mg as well as Cs was used for normalization of P counting rates. One hundred P/Cs and P/Mg ratios were collected for every sample. Results for P concentrations are consistent between Cs and Mg normalized counting rates (Figure 2.3.6). Typical 1 sigma standard deviation was <3%. Reproducibility of analyses performed on different days is on the order of few percent.

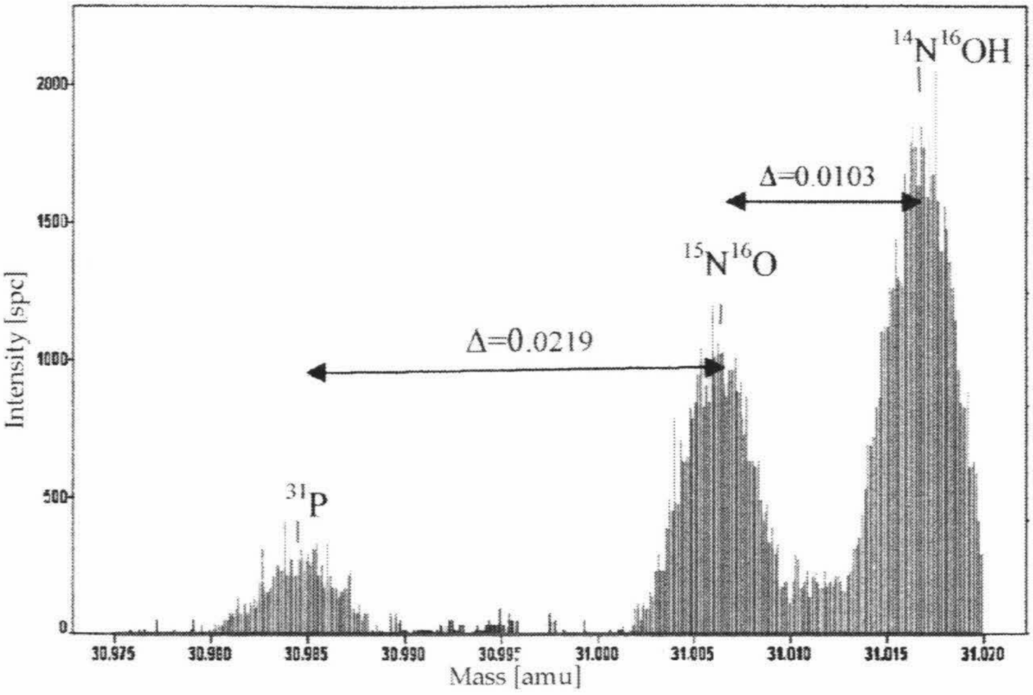

Figure 2.3.4 Medium resolution scan of the mass interval 30.975-31.020 amu, showing resolution of the phosphorus peak and $^{15}N^{16}O$ and $^{14}N^{16}OH$, arising from the HNO_3 carrier solution. Peak corresponds to 7 ppb P concentration.

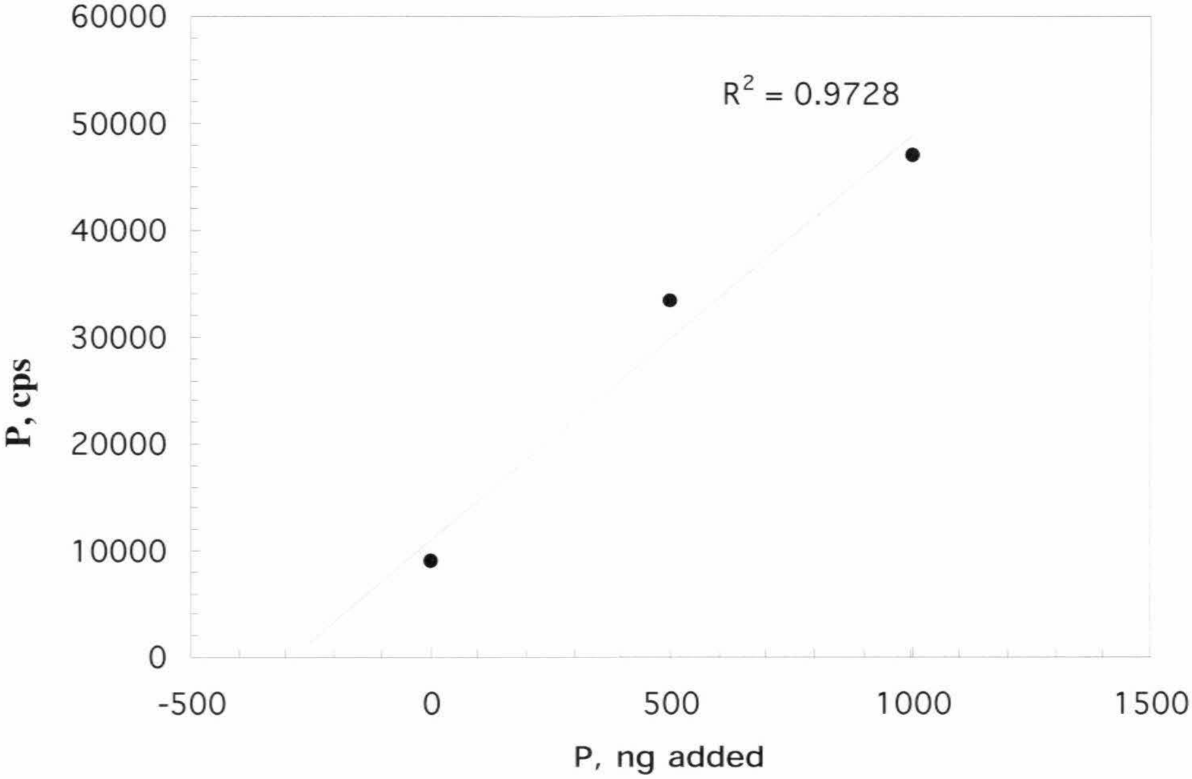

Figure 2.3.5 The Standard Addition method for P without internal standardization. Slope of the line (cps/ppm P) used to calculated P concentration in the unspiked sample solution. Graphically, extrapolation of the cps P vs. ng of P added line to P(cps)=0 gives the concentration of P in the unspiked solution.

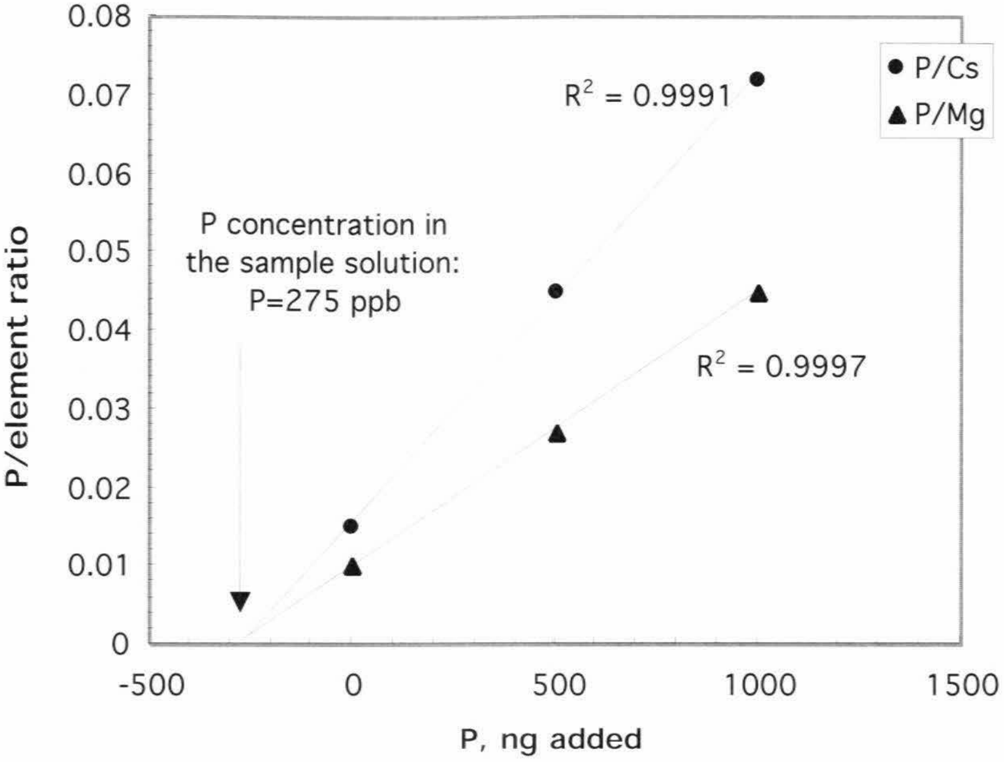

Figure 2.3.6 Demonstration of the Standard Addition technique with normalization of the P counting rates against Cs and ^{25}Mg.

Chapter 3: Ordinary chondrites

3.1 Sample selection and preparation

As discussed in Chapter 1, the bimodal distribution of Th/U in ordinary chondrites is surprising. Based on the previous literature data and issues raised by Figure 1.3, we focused on the anomalous (with respect to Th/U) chondrites, Harleton and Glatton. Rather than assume that all specimens of these have anomalously high Th/U, we established experimental procedures to be able to perform high accuracy isotopic dilution Th and U analyses. With this approach, we could guarantee that the samples we were characterizing did in fact have anomalous Th/U. This conservative approach turned out to be very important and led to solution of the problem.

Analyzed samples are listed in the Table 3.1.1. Two fragments of Glatton and 5 individual multigram fragments of Harleton (I, II, U, 4,5,6) were subdivided into approximately gram-sized samples. Only 2 samples (H6-3 and H6-5) are substantially smaller, about 30 mg. These two samples are round, presumably fragments of relict chondrules. Both are gray and visually homogeneous, H6-3 being darker than H6-5. The last column in Table 3.1 reflects which samples came from the same rock fragment. USNM 2576 and USNM 6625 are separate stones in the Harleton fall. All samples were prepared as described in the Chapter 2. For reference, samples of Leedey (L6) and Allende (CV3) meteorites were analyzed.

Petrography of Harleton chondrite

The Harleton meteorite fell four miles east of Harleton, Harrison County, Texas, on 30 May 1961 (Clarke at al., 1974-75 and references therein). A single stone, weighing 8.36 kg was recovered within ten minutes of the time of the fall. Macroscopically, the interior of the meteorite appeared remarkably homogenous and compact, with a few, poorly defined, chondrules.

Except for a slightly higher FeS content, there is no significant difference in the chemical composition of the Harleton meteorite with an average L(4-6) chondrite composition (Table 3.1.2).

Thin sections under the electron microscope (SEM) show granular agregates of olivine, orthopyroxene and opaque minerals (troilite, metal and chromite). Uniformity of the reflectance of the olivine and orthopyroxene grains in SEM BSE image mode implies homogeneously distributed Fe and Mg contents (characteristic of the equilibrated chondrites). Relict chondrules are rare and poorly defined. Phosphate grains are both chlorapatite and merrillite. Apatite grains as big as 200 μm were obseved (Figure 3.1.1).

Modal analyses of one 10x4 mm section of Harleton are reported in the Table 3.1.3. These are compared with normative composition, calculated from the chemical analyses from Table 3.1.2. From the chemical and mineralogical composition in Tables 3.1.2 and 3.1.3, it is evident that Harleton is typical equilibrated L6 chondrite.

The sizes of the phosphate grains seem to be the only characteristic feature of this meteorite. It should be noted that total amount of phosphates (as well as total phosphorus in the rock) is within the range of L-chondrites (see Tables 3.1.2, 3.1.3).

Table 3.1.1 Sources of meteorite samples.

	#, year received and source
Leedey (L6)	#489.15 Center for Meteorite Studies, Arizona State University
Allende (CV3)	USNM3529 split 9, position 2, 1998, National Museum of Natural History, Smithsonian Institution (NMNH)
Glatton (L6)	
Glatton I	BM, 1991,M3 British Museum, UK
Glatton II	BM, 1991,M3 British Museum, UK
Glatton W	G.J. Wasserburg
Harleton (L6)	
Harleton I	USNM2576, 1992, NMNH
Harleton II	USNM2576, 1992, NMNH
Harleton U	D. Unruh
H4-2	USNM2576, 1998, NMNH
H4-4	USNM2576, 1998, NMNH
H4-6	USNM2576, 1998, NMNH
H5-2b	USNM6625, 1998, NMNH
H6-1	USNM2576, 1998, NMNH
H6-3[*]	USNM2576, 1998, NMNH
H6-4	USNM2576, 1998, NMNH
H6-5[*]	USNM2576, 1998, NMNH
H6-6	USNM2576, 1998, NMNH

[*] Small (~30mg) relict chondrules.

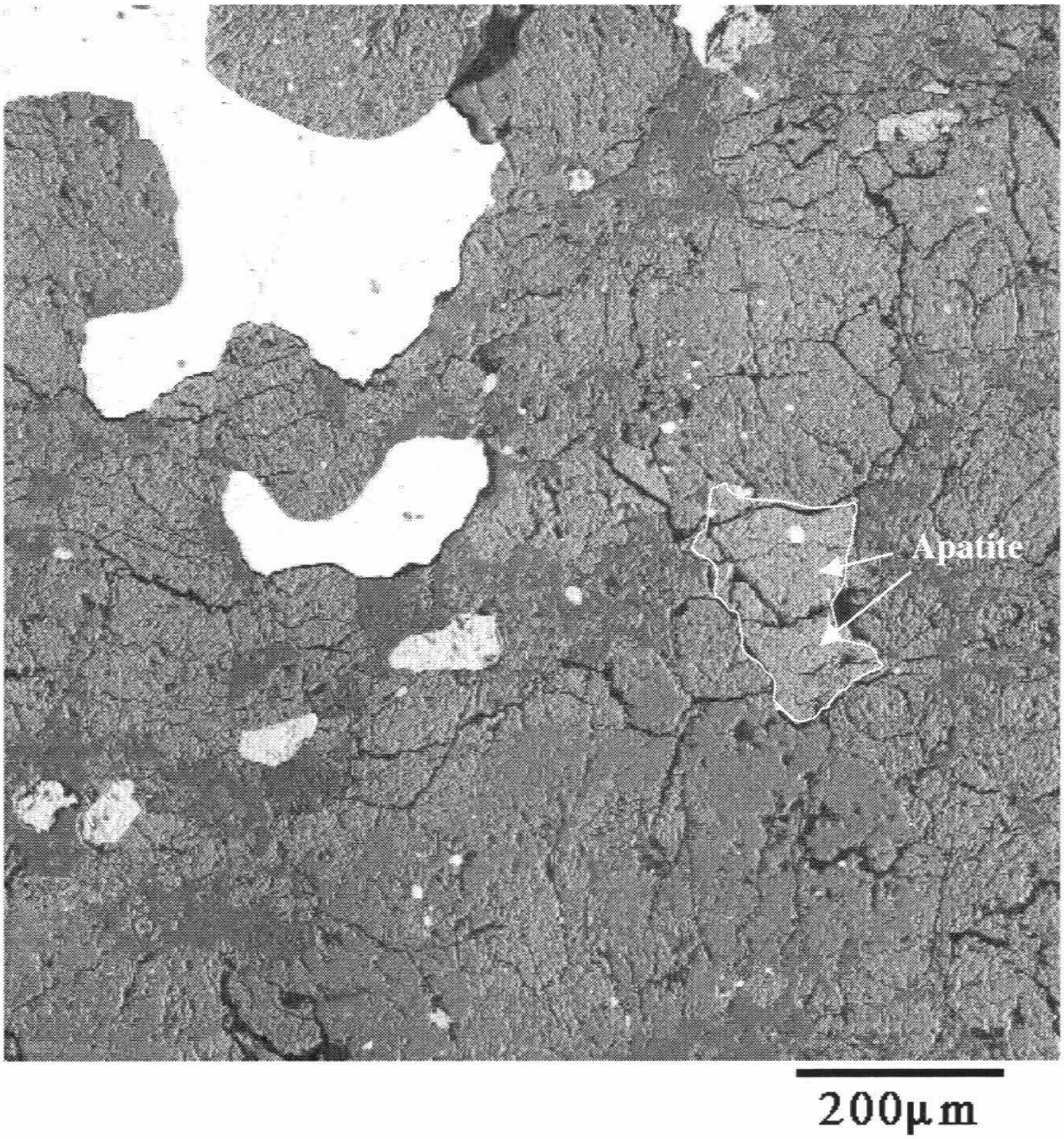

Figure 3.1.1 Backscattered secondary electron image of the Harleton meteorite thin section, outlining big, 100X200 μm apatite grain.

Table 3.1.2 Chemical composition of Harleton chondrite compared to average L chondrites.

Constituent[1]	Harleton, L6[2]	L(4-6) chondrites[3]
SiO2	39.85	39.69
MgO	24.77	24.72
Al2O3	2.14	2.30
Cr2O3	0.52	0.53
MnO	0.33	0.34
TiO2	0.10	0.12
CaO	1.81	1.82
Na2O	0.92	0.94
K2O	0.1	0.11
P2O5	0.23	0.23
FeO	14.3	14.31
FeS	6.58	5.78
Ni	1.14	1.24
Co	0.06	0.07
Fe-metal	7.28	7.37
Fe-total	22.6	22.17

[1] Composition in weight percent.
[2] Clarke et al. 1974-75.
[3] Jarosewich and Dodd 1985.

Table 3.1.3 Normative composition (volume percent) of Harleton compared to average L chondrites.

Constituent	Harleton[1]	Harleton[2]	L(4-6)[3]
Olivine	41.3	43.7	43.6
Orthopyroxene	31.6	27.4	27.5
Clinopyroxene	4.3	5.3	6.0
Feldspar	11.1	13.4	13.0
Apatite[4]	0.4	0.6	0.6
Chromite	0.6	0.6	0.7
Troilite	4.2	5.0	4.4
Nickel-Iron	6.4	4.0	4.2

[1] R. Radtke (personal communication), made by electron microprobe on section from USNM2576.

[2] Clarke et al. 1974-75; norm based on chemical analysis in Table 3.1.2.

[3] Jarosewich and Dodd 1985; norm.

[4] "Apatite" represents total amount of phosphates.

3.2 U, Th, P analytical data

Th and U results, given in Table 3.2.1, are based on the quadrupole ICP analyses. They are corrected for mass fractionation. Mass fractionation correction was made on the basis of three measurements of an isotopically normal U solution. The correction of 0.5% per amu was applied to both ^{230}Th/^{232}Th and ^{235}U/^{238}U.

Procedural blanks (contamination from acids used for digestion plus sample handling during dissolution) were measured using the same mixtures of concentrated acids as for samples. These were evaporated and re-dissolved in 7% nitric acid for analyses. The procedural blanks are at $\approx 10^{-13}$ g for U and Th (negligible, see analytical techniques in Chapter 2).

Table 3.2.1 gives Th, U, Th/U, and P for the analyzed samples. We also tabulate data for previous Th and U analyses of Harleton and Glatton.

Samples of Harleton and Glatton were expected to be anomalous, so a sample of Leedey (L6) was analyzed as representative of a "normal" L chondrite. Our Leedey sample was an aliquot of an older homogenized chondrite silicate sample prepared by crushing a multigram sample. Larger metal fragments were removed during the crushing; consequently, our U and Th concentrations are somewhat higher than typical values. However, as given in the table, our Th/U for this meteorite is in good agreement with previous literature data.

Table 3.2.1 shows that all of our Glatton samples have typical U and Th concentrations for L chondrites. The Glatton P concentrations show a total range of about a factor of 1.5 and the average is somewhat higher than the average L chondrite literature value. None of our Glatton samples show the anomalously high Th/U found by Chen *et al.*, 1993.

By analyzing a large number (12) of Harleton samples, we obtained a wide range of Th/U, including low as well as normal values of Th/U, in addition to only high values reported by Unruh, 1982. *The bimodal distribution in the previous literature Th/U values (Figure 1.3) for ordinary chondrites is only apparent.* Specimens of Harleton show a range in Th/U from 2.5 to 6, larger than the total range observed in previous isotopic dilution analyses. The variations are mostly due to variations in U content. U varies by a factor of 5; Th by a factor of 2. We will focus on the Harleton data in the subsequent discussion.

Figure 3.2.1 shows that the Th/U variations in Harleton display a linear correlation when plotted against 1/U. Taken at face value, the linear trend implies that the Th/U variations are the result of different amounts of mixing of high U, low Th/U and low U, high Th/U end members. There is no obvious grouping among the samples from the same large fragments (H4, H6, HI,II). In fact, the largest Th/U differences among gm-sized samples is between H6-4 and H6-6. Sample H6-5 (smaller sample, presumably relict chondrule, see Table 3.2.1) showed the highest Th/U ratio.

Figure 3.2.2 shows that, in hindsight, all high precision data for ordinary (types 4-6) chondrites also conform reasonably well to the Harleton trend. An exception is the sample of Glatton (Chen *et al.*, 1993), which is characterized by a high Th and Th/U (Table 3.2.1) and lies distinctly off the Harleton trend. No high precision data are available for type 3 unequilibrated ordinary chondrites. No differences are observed among H, L and LL chondrites.

For equilibrated ordinary chondrites, there are three components which affect Th/U and 1/U. Two phosphates (merrillite and chlorapatite) are well characterized as phases in which actinides are concentrated. Based on Crozaz (1974, 1979), the Th/U for merrillite is high (9-11), but much lower in apatite (1-3) (Table 3.2.2).

So, 2 actinide-rich end members with sufficiently different Th/U are known to be present. The third component is the proportion of admixed inert (i.e. actinide-free) phases to the phosphates. The mixing line between the two phosphates is shown in the left-hand side of Figure 4.2.3. Random mixtures of the two phosphates and inert material might be expected to show a lot of scatter on a Th/U vs. 1/U plot (addition of the inert material will dilute U content, but will not change Th/U ratio), but a good correlation is observed, especially clear in the Harleton data.

Thus, a different mechanism is required to explain Figures 3.2.1 and 3.2.2 than just random mixing of phosphate end members and inert material.

Table 3.2.1 U, Th, P analytical data.

Sample ID	Weight (g)	^{238}U, ppb*	^{232}Th, ppb*	Th/U†	P (ppm)
A&G‡		8.1	29.4	3.63	1180
Allende	0.992	12.54	43.28	3.43	1235
LeedeyA	0.999	17.48	60.6	3.44	1040
Glatton$	1	12.5	74	5.87	na
Glatton I	0.979	9.34	36.1	3.83	920
Glatton II	0.891	11.7	43.8	3.70	1260
Glatton W	0.853	12.2	46.3	3.77	1410
Harleton-1#	0.096	6.17	37.5	6.03	na
Harleton-2#	0.075	5.47	32.7	5.93	na
Harleton-3#	0.073	5.07	32.8	6.42	na
Harleton I	0.937	12.38	39.6	3.17	1910
Harleton II	0.957	12.78	43.1	3.35	1460
Harleton U	0.836	11.27	39.8	3.50	1790
H4-2	0.756	10.14	35.8	3.51	936
H4-4	1.154	12.47	36.7	2.93	1140
H4-6	0.992	11.49	39.3	3.39	1110
H5-2b	0.466	8.26	36.5	4.39	916
H6-1	1.118	12.94	43.6	3.34	985
H6-3	0.029	14.1	41.4	2.91	2240
H6-4	1.088	7.03	31.0	4.38	1550
H6-5	0.028	8.03	48.8	6.04	424
H6-6	0.688	25.05	63.5	2.52	630

* ID-ICPMS analyses, corrected for MS isotope fractionation.
† Th/U is a weight ratio, accuracy <1.5% (1σ).
‡ CI chindrites, Anders and Grevesse, 1989.
$ Chen *et al.*, 1993 (and personal communications).
# Unruh, 1982.

Table 3.2.2 St. Severin phosphates (data from Crozaz, 1979).

Phase (# of grains)	U, ppm	Th, ppm	Th/U (wt.)
Chlorapatite (1)	7.5±0.8	11.2±3.8	1.5
Merrillite (7)	0.275±0.025	3.21±0.25	11.67

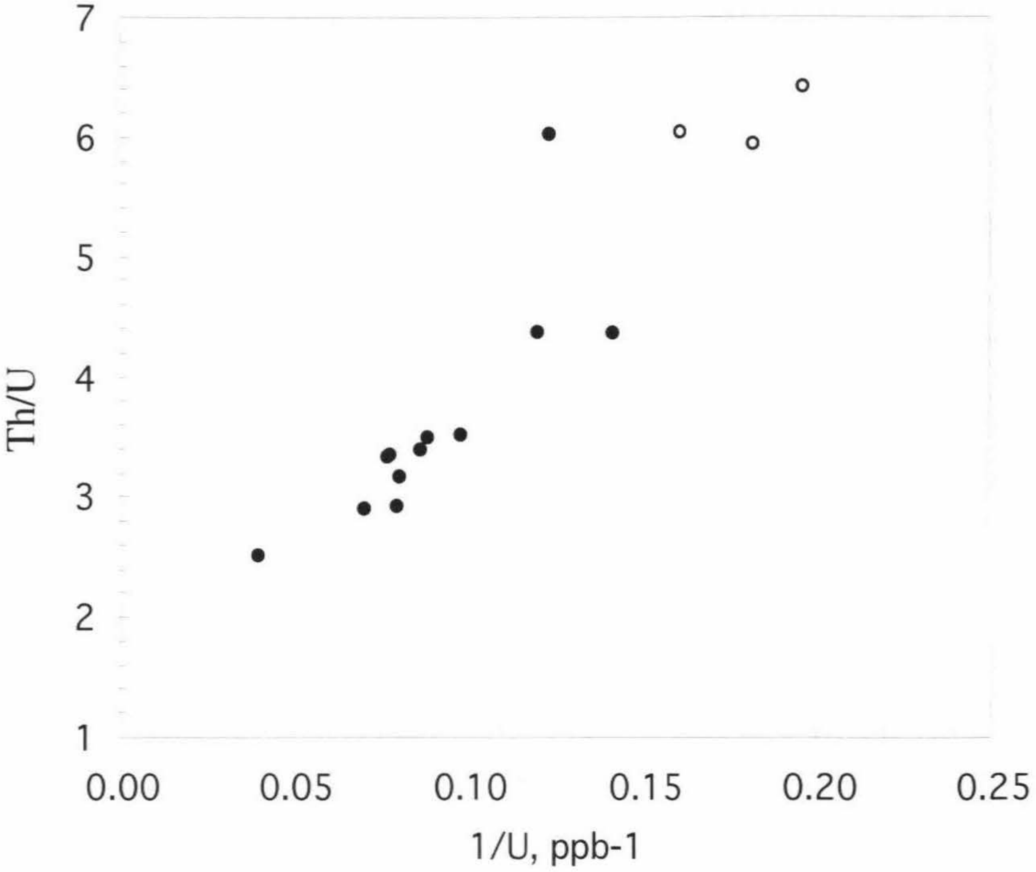

Figure 3.2.1 Th and U isotope dilution data for Harleton. Filled circles - this work, open circles from Unruh, 1982. The linear trend on the plot Th/U vs. 1/U implies a two component mixing between high U, low Th/U, and low U and high Th/U components.

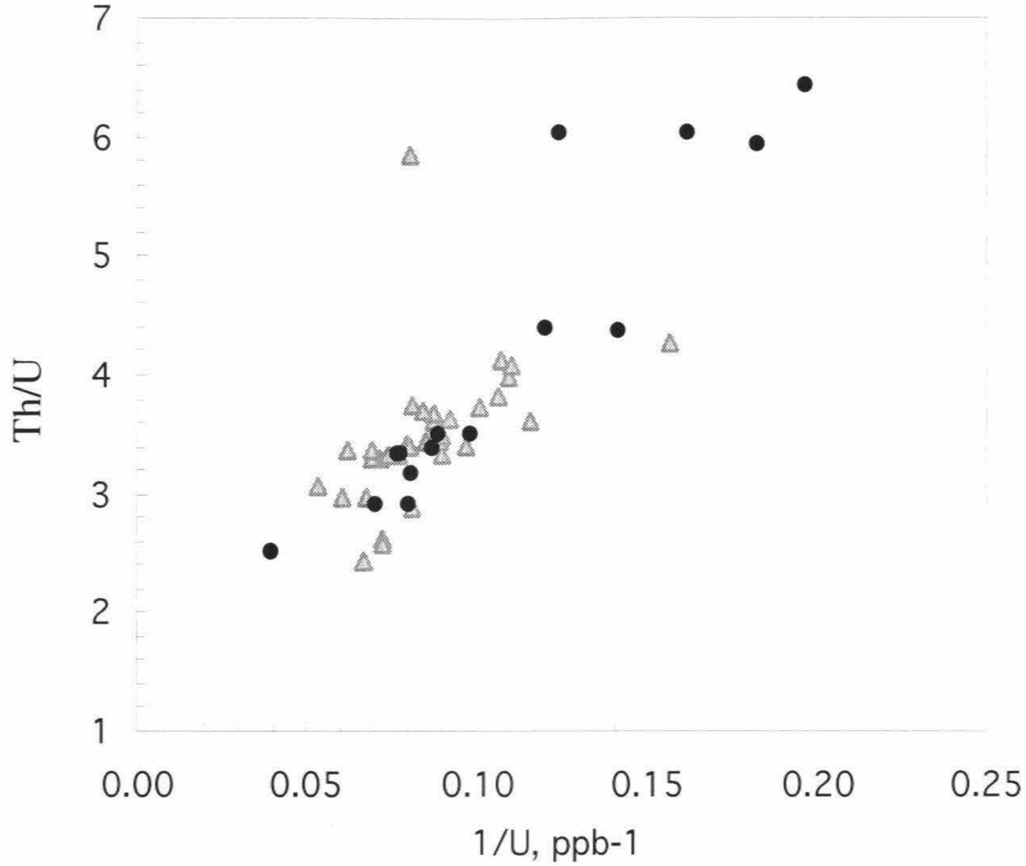

Figure 3.2.2 Combined Harleton data (circles) and literature data (triangles) on ordinary chondrites (from Tatsumoto et al., 1973, Unruh, 1982, Hagee et al., 1990, Chen et al., 1993, Shinotsuka et al., 1995 and this study) data. Ordinary chondrites are mostly types L4-6 plus 5 data points of St. Severin (LL6) and 3 points of of H5. This plot shows that ordinary chondrite data follow the same linear trend as Harleton.

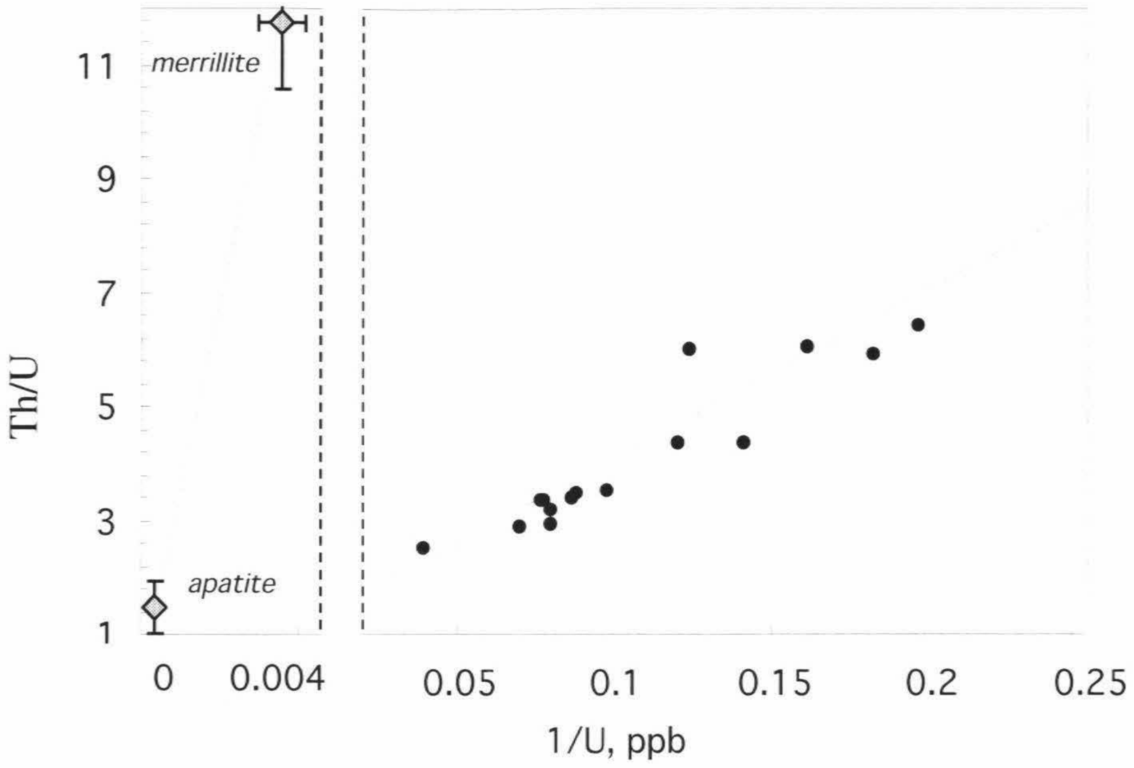

Figure 3.2.3. Model I. Phosphates data from (Crozaz, 1979). Line on the left-hand side represents mixing between 2 phosphates. Dilution of points on this line by random factor will produce scatter in the right-hand side of the plot (note change in scale). Filled circles are Harleton data. Linear trend through these data is calculated in the Model I apatite-merrillite mixing, using dilution factor of 100.

3.3 Phosphate control on the actinide abundances

Model I

A very simple model can quantitatively fit the trend observed in Figure 3.2.1. The left-hand side of Figure 3.2.3 shows the location of the merrillite and apatite points from St. Severin, LL6 (Crozaz, 1979). Relative to Figures 3.2.1 and 3.2.2, an expanded 1/U scale is used here to illustrate the much higher U concentration in apatite compared to merrillite. In Model I we use the St. Severin phosphate Th and U concentrations from Crozaz (1979). Numerical values are summarized in Table 3.2.2.

The dashed curve on the right-hand side of Figure 3.2.3 is calculated by simply taking the St. Severin phosphate data and diluting the U concentrations of both phosphates by a factor of 100, simulating the effect of mixing 1 part phosphates with 99 parts of inert material. The slope of this curve fits the data for equilibrated ordinary chondrites. *The very fact that the slope of the data trend in Figure 3.2.3 matches the phosphate mixing slope says that phosphate variations are indeed the reason for the whole rock Th/U correlation.*

In this model, analyses that are known to involve *three* components (two phosphates and inert material) described by a *two* component mixing line because the phosphate mixture is *uniformly* diluted by inert material. The variations along the line reflect the different proportions of phosphates, with apatite (the high U end member) being especially important. The observed data points correspond to a range of apatite/merrillite from 0.03 (highest Th/U) to 0.3 (lowest Th/U).

Petrographic observations on polished sections of Harleton revealed the special nature of this meteorite. It appears to have a larger proportion of apatite relative to merrillite with large (up to 200 micron, as shown in Figure 3.1.1) apatite grains. In the context of Model I, the proportions of apatite are not unprecedented; however, the unique aspect appears to be the large grain size. With more-or-less normal amounts of U-rich apatite concentrated in large grains, fluctuations in the number of these grains drives large variations in Th/U in gram-sized Harleton samples. In particular, samples which by chance have few or no large apatite grains, but typical amounts of merrillite, will show high Th/U ratios, explaining the Unruh, 1982 data which were the motivation for this study. It is quite ironic that control by apatite (a phase with low Th/U) was first revealed by samples that showed high Th/U ratios. Furthermore, given this non-intuitive feature in the data, it is the ability of mixing models to *quantitatively* describe the Th/U vs. 1/U trend that strongly argues that we have the correct interpretation.

The success of Model I must be respected; however, it is oversimplified and not correct in detail, as we now proceed to discuss. Before launching into complications, it is important to note the conclusion, which we believe to be generally valid, that the chlorapatite control of the U and Th/U distributions very likely reflects heterogeneities in the Cl distribution in the original parent bodies. These Cl heterogeneities then are the ultimate control on the U and Th/U distributions.

Model I makes testable predictions. The required constant dilution factor of 100 implies a total phosphate abundance of 1%, or equivalently, a whole rock P content of around 2000 ppm, but these are a factor of 2 higher than typically observed in ordinary chondrites. Thus, Model I predicts: (1) similar U and Th contents in Harleton and St.

Severin phosphates; (2) a uniform P content in the Harleton samples (variations of up to about ± 20% would be permitted by the scatter in Figure 3.2.1); (3) P concentrations for Harleton that are roughly twice that typically found in ordinary chondrites.

Preliminary ion probe data for Harleton phosphates

Our preliminary ion probe data for Harleton phosphates show that in Harleton, as well as in St. Severin, phosphates display the same characteristic high Th/U (merrillite) and low Th/U (apatite) values.

Ion probe analyses were performed with UCLA IMS-1270. Data for ThO and UO were collected relative to ^{40}Ca. Standard error for ThO/UO is between 1.5 and 3.7%. Standard error is based on 20 cycles that were taken in the measurement. Durango apatite was used as a standard (Ian Hutcheon, Lawrence Livermore National Laboratory). Concentrations of U and Th in Harleton phosphates, St. Severine apatite from this work as well as Crozaz, 1979 are presented in Table 4.2.3. Analyses of the Durango apatite standard are also listed.

Although these results show that actinides in Harleton phosphates follow the same rules as phosphates from St. Severin, actinide concentrations are lower, especially for apatite. However, our data alone are not sufficient to make definitive conclusions, since only the two largest phosphate grains were analyzed.

Table 3.3.1 Th and U ion probe data of phosphates.

Phase (# of grains)	U, ppm	Th, ppm	Th/U (wt.)
St. Severin			
Chlorapatite (1)[1]	7.5±0.8	11.2±3.8	1.5
Merrillite (7)[1]	0.275±0.025	3.21±0.25	11.7
Merrillite (1)[2]	0.325	3.25	10
Harleton			
Chlorapatite (1)[2]	3.6	4.8	1.3
Merrillite (1)[2]	0.2	1.9	9.5
Durango apatite[3]	16.3±1.1	313±9	19.2

[1] Crozaz, 1979.

[2] This work, see text for uncertanties.

[3] I. Hutcheon, personal communication.

Phosphorus analyses.

Major advantages of our ICPMS techniques are that only a small fraction of the sample is consumed in the Th/U determination and that it has excellent sensitivity for the determination of other elements. Thus we were able to test the predictions of Model I by measuring P on exactly the same samples for which U and Th are measured.

Figure 3.3.1 summarizes the results of P analyses:

(1) In spite of the prediction of Model I, P concentrations are not constant in Harleton. A total range over a factor of 5 is observed. The most deviant P concentrations are observed on our smallest (30 mg) samples; however, even when these are omitted, a range over a factor of 3 is observed. (2) The observed P contents are not uniformly high compared to the average 1000 ppm for L chondrites (Moore, 1971). Based on large (10-20 g) samples, the P from the chemical analysis of Clarke et al., 1974-75 (Table 3.1.2) is 1004 ppm. Our average Harleton P concentration is 1240 ppm. Only 2-3 samples have near the 2000 ppm predicted by Model I. (3) There is no clear correlation of Th/U with P. Similarly, there is no correlation of P with U or Th separately (see Figures 3.3.2 and 3.3.3).

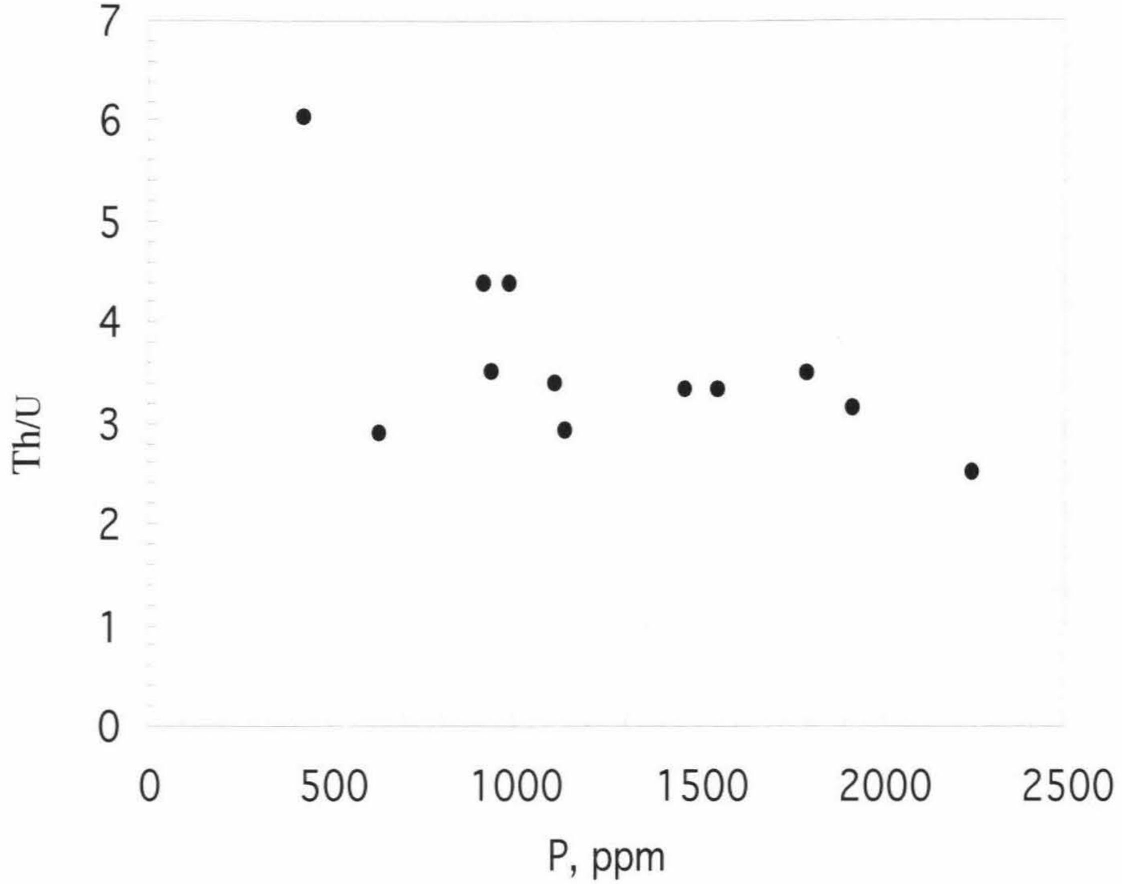

Figure 3.3.1 Th/U vs. P for Harleton. P concentrations show much bigger scatter than predicted by Model I.

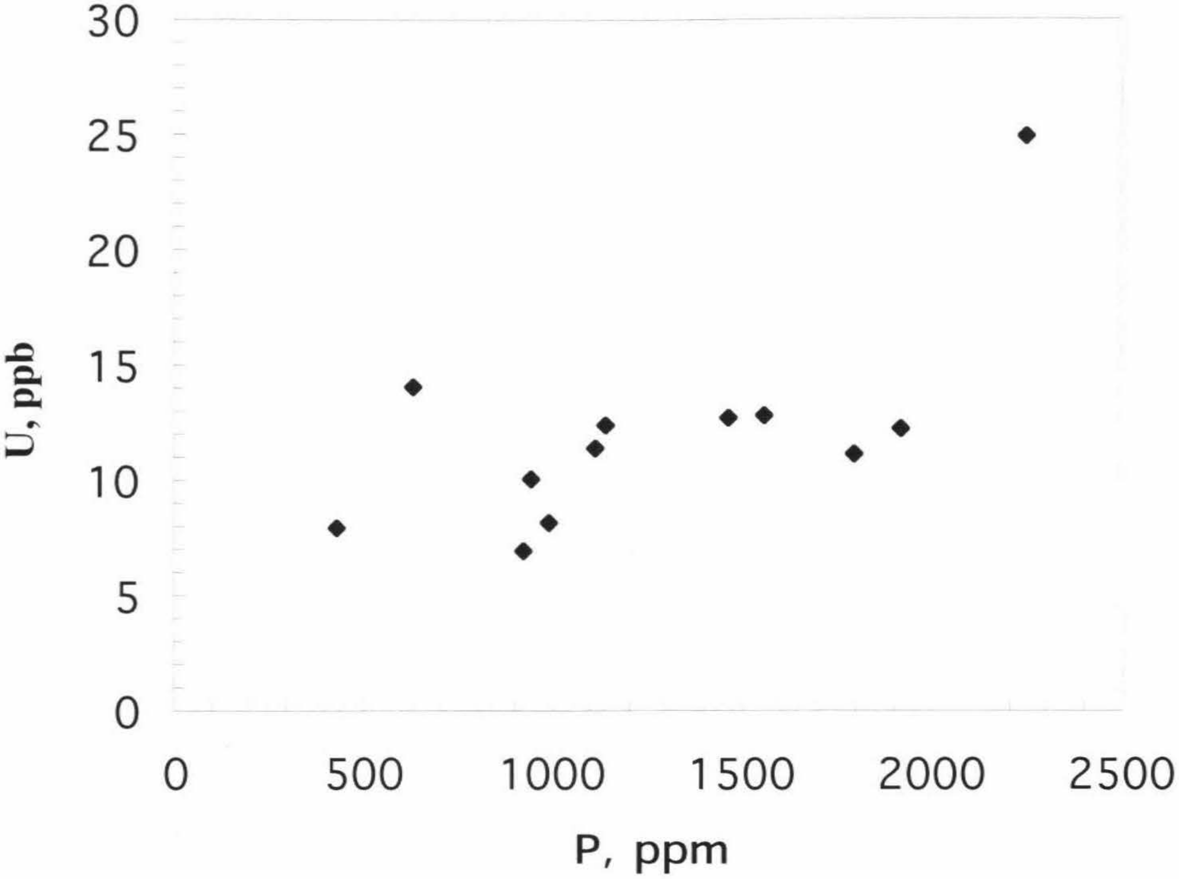

Figure 3.3.2 Plot of measured U concentrations vs. P content in the same sample aliquates.

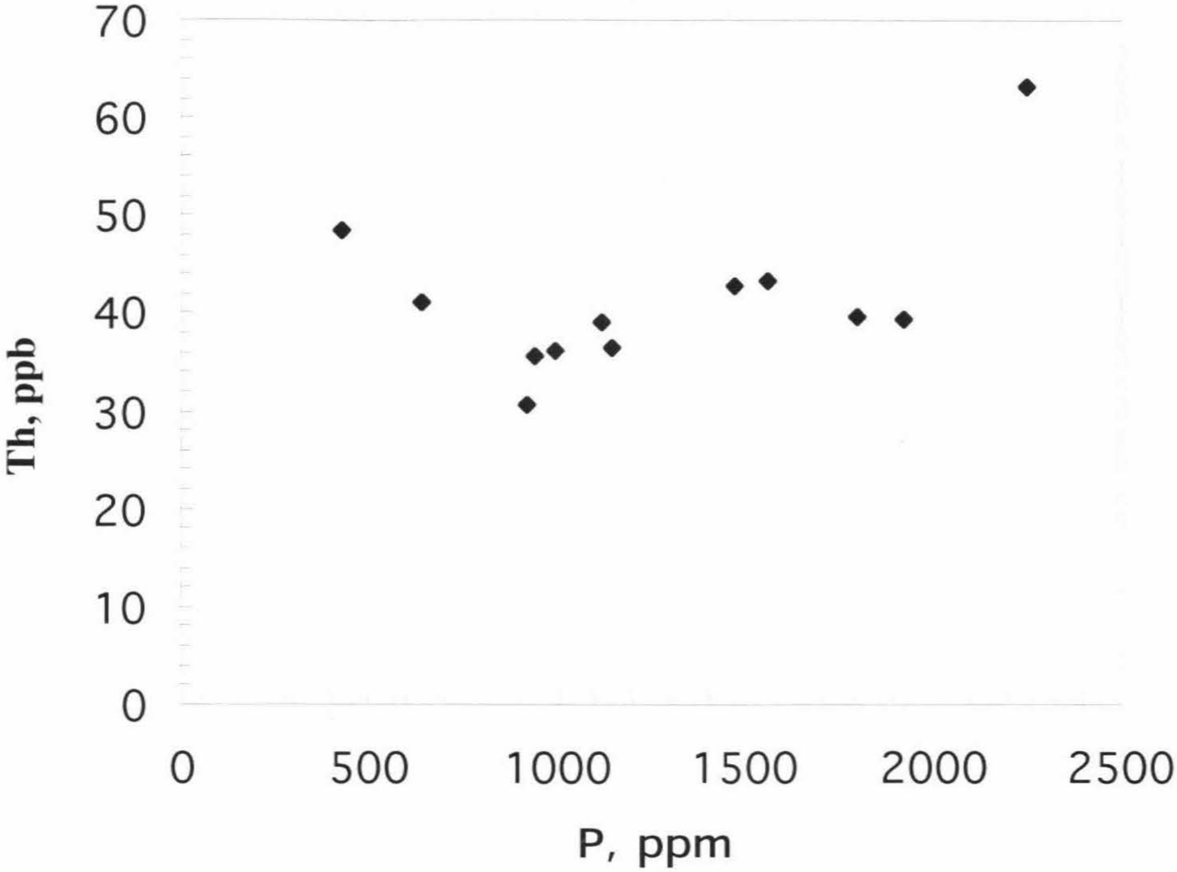

Figure 3.3.3 Plot of measured Th concentrations vs. P content in the same sample aliquots.

This is a failure of the Model I. However, this is probably not a failure of the concept of apatite control, but instead, it indicates the need for a more complex model.

The most interesting feature of the Harleton data is the variability of P concentrations. By itself, the failure of the Harleton samples to show the 2000 ppm predicted by Model I could have been explained simply by abandoning the St. Severin phosphate U concentrations and assuming instead that the Harleton phosphate U concentrations are roughly twice as large. In the mixing model there is a tradeoff between dilution factor and phosphate U concentrations. Our ion probe data show that U concentrations in apatite are roughly the same as for other ordinary chondrite apatites (1-3.5 ppm, Crozaz et al., 1989). The St. Severin apatite U concentration is already the highest. Thus, there is no observational support for increasing U in apatite to compensate for this failure of Model I. However, all actinide measurements are biased towards the biggest grains. This will be considered later.

The lack of uniform P content as well as lack of correlation between P and Th/U (Figure 3.3.1) among the Harleton samples should have produced scatter in the Th/U vs. 1/U plots (Figure 3.2.1 and 3.2.2), but regularity is observed instead. There is a special process, associated with the petrogenesis of ordinary chondrite, which produced the observed correlation.

Model II

Here we retain the successful core of model I that Th/U variations are a reflection of varying proportions of apatite and merrillite. However, we drop the explicit assumption of the St. Severin phosphate Th and U concentrations, and allow [U] and [Th] to vary within phosphates and among the different Harleton samples. For model II, we assume instead that we should take "equilibrated" literally, and assume that in each sample the *relative* amounts of U (and Th separately) between the two phosphates at least approach an equilibrium partitioning ratio defined as $D_U \equiv [U]_{ap} / [U]_{merr}$ (and similarly for Th). We assume that the values for D_U (27) and D_{Th}(3.5) can be inferred by the Crozaz (1979) data for St. Severin. Thus, for model II we have:

$$(Th/U) = (Th/U)_{phos} = (Th/U)_{ap} \; [\, (f_{ap} + f_m/D_{Th}) / (f_{ap} + f_m/D_U) \,] \qquad (1)$$

where the subscripts phos, ap, and m refer to total phosphate, apatite and merrillite, f_i is the fraction of phosphate which is phase i (i.e., $f_{ap} + f_m = 1$).

Simlarly, the whole rock [U] concentration is:

$$[U] = [U]_{phos}/F = ([U]_{ap}/F) \, [(f_{ap} + f_m/D_U) \,] \qquad (2)$$

where F is the dilution factor (gm rock / gm phosphate), but also

$$F = [P]_{phos} / [P] \qquad (3)$$

where [P] is the whole rock P concentration and $[P]_{phos}$ is the concentration of P in phosphates.

Accepting the D as known and constant, there are still four unknowns in the model: f_{ap}, $[U]_{ap}$, $[Th]_{ap}$, and F. Strictly speaking $[P]_{phos}$ in equation (3) depends on f since the P contents of merrillite and apatite differ slightly. Our detailed calculations allow for this, but the effect is totally negligible and $[P]_{phos}$ can be regarded as a constant. Thus, F is completely determined by the measured P concentration. However, even with this simplification, the model remains underdetermined. Although the model doesn't make explicit predictions, there are no required specific correlations between P and Th/U, [U], or [Th] as observed.

If we make an additional assumption, we can use the measured concentrations of U, Th, and P to solve for the unspecified model parameters. A reasonable assumption is that the Th/U in apatite is the same in all samples and the value lies in the range of 1 to 2.5. With this additional assumption we can calculate the actual concentrations of U and Th in the phosphate phases. The additional assumptions in Model II build in the mixing trend from Figure 3.2.1; however, the fit parameters of Model II provide insight into the origin of the mixing trend.

Figure 3.3.4 shows a well-defined correlation between the measured total rock U concentration and the amount of apatite *calculated* from Model II. It demonstrates that the apatite control over U concentration inferred from Model I is maintained in Model II. The failure to have uniform dilution factors does not affect this major conclusion. Figure 3.3.4 is shown for an assumed apatite Th/U = 2, but the observed trend is independent of what is assumed for apatite Th/U (see Fgure 3.3.5). What does change is the calculated range of values for f_{ap}. For lower values of apatite Th/U, lower apatite abundances are calculated.

Figure 3.3.6 shows that there is a general inverse correlation between the U concentration in apatite *calculated* from Model II and the *measured* P concentration. Although an apatite (Th/U) must be assumed to calculate the model $[U]_{ap}$, the trend in Figure 3.3.6 is totally insensitive to the value of apatite (Th/U) chosen; only the $[U]_{ap}$ scale is affected, analogous to Figure 3.3.5. In other words, the assumed Th/U ratio of apatite determines the intercept of the trend in Figure 3.3.6, but does not influence the slope. The data point in Figure 3.3.6, which deviates the most from the trend, is the smallest (relict chondrule) sample H6-3 (see Table 3.2.1).This sample has an anomalously high P content. If a relict chondrule, the high P concentration is surprising. In general we have no explanation as to the anomalous location of this sample on Figure 3.3.6. H6-3 has the lowest Th/U, but plots close to the trend on Figure 3.2.1.

In Figure 3.3.6 the U concentration in apatite is in no way fixed when a P concentration is specified. The correlation in Figure 3.3.6 is not built into the assumptions of Model II. It instead represents a property of ordinary chondrite metamorphism. Figure 3.3.6 helps understand why the lack of uniform P contents and the lack of a correlation between P and Th/U (Figure 3.3.1) did not produce scatter on the Th/U vs. 1/U plots (Figures 3.2.1 and 3.2.2) instead of the observed regularity.

The correlation shown in Figure 3.3.6 is probably best viewed as the response of the U and Th concentrations to P inhomogeneities. With an increase in P, the U concentration in apatite decreases, i.e., a dilution effect. Figure 3.3.6 illustrates a secondary control on the U concentrations, with apatite (and chlorine) abundances (Figure 3.3.4) being the primary control.

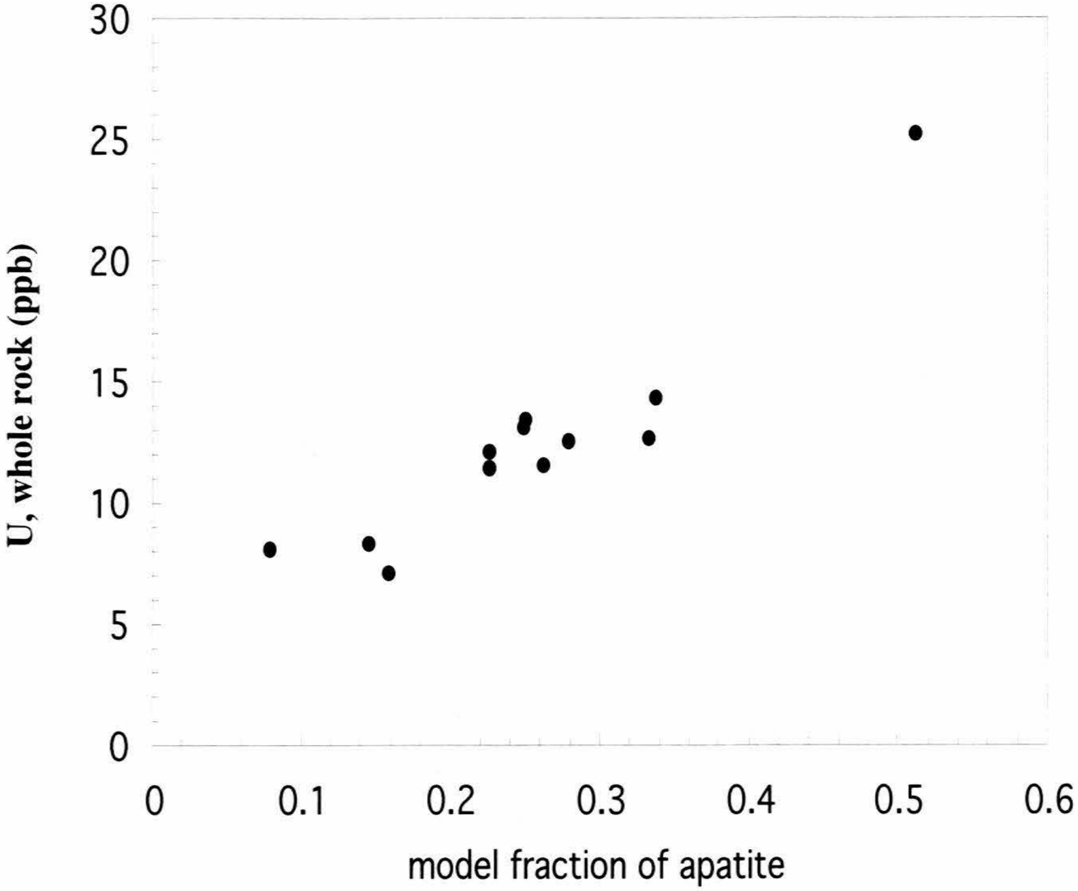

Figure 3.3.4 Plot of measured whole rock U vs. fraction of apatite calculated from Model II. Th/U ratio in apatite is assumed equal to 2.

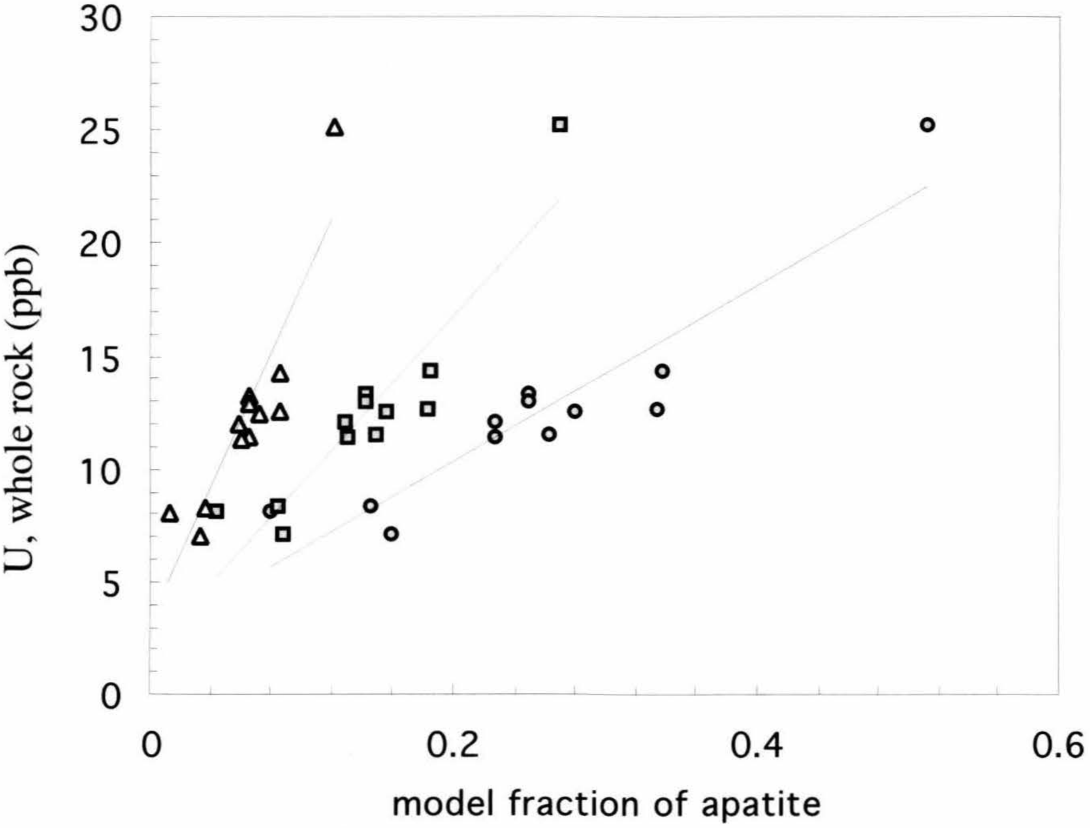

Figure 3.3.5 Same plot as Figure 3.3.4, but showing calculated fraction of apatite for different $[Th/U]_{apatite}$. Circles, squares and triangles correspond to $[Th/U]_{apatite}$ equal 2, 1.5 and 1 respectively.

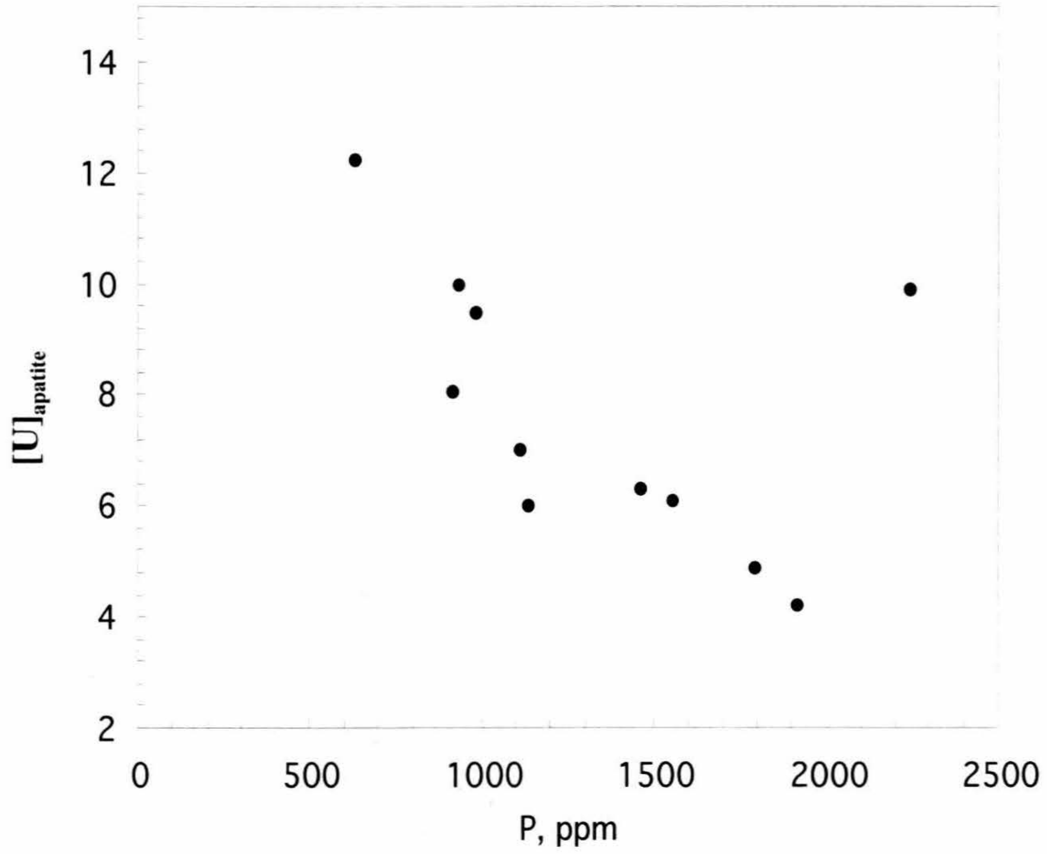

Figure 3.3.6 Model II. Plot of calculated concentrations of U in apatite vs. measured phosphorus concentrations. $(Th/U)_{ap} = 2$ gives most reasonable values for U_{ap}. The two most deviant points (one in with high P, high $[U]_{ap}$ and one off plot) are small relict chondrules (see Table 3.2.1 and Figure 3.3.1).

3.4 Implications for ordinary chondrite petrogenesis

Our data show that the large range of Th/U seen among ordinary chondrites can be found in one meteorite and that the bimodal distribution (see Introduction) of this ratio among meteorites is only apparent.

The nature of the uranium carrier phases in ordinary chondrites is a long standing problem. In a detailed study of the uranium distribution of the St. Severin (LL6) chondrite with the use of fission track radiography, Jones and Burnett (1979) were able to locate reliably apatite grains down to about 1 micron in size. From these data only about 5% of the phosphates were apatite. Apatites greater than 1 micron accounted for 15% of the total meteorite U, and all phosphates accounted for only 24%. Greater than 60% of the U resided in unknown interstitial submicron phases. Jones and Burnett noted that submicron apatite was a plausible candidate for the missing U. This was supported by a lack of a Cl material balance if only the larger apatite grains were considered. Hagee et al. (1990) measured Th/U ratios of 2.60 and 3.63 for samples of the dark and light phase of St Severin. Equation (1) and the St. Severin data give apatite abundances of 25 and 13% for the dark and light phases, significantly larger than the observed 5% for the large apatite grains by Jones and Burnett. The samples of St. Severin used by Jones and Burnett and by Hagee et al. (1990) were not identical; nevertheless, the above calculation gives strong support to the interpretation that submicron apatite grains control the U distribution in St. Severin. The St. Severin analyses of Hagee et al. (1990) are included on Figure 3.2.2 and are consistent with the Harleton trend, also supporting apatite control for St. Severin.

Possibly contradictory evidence comes from leaching studies on non-magnetic fractions of equilibrated ordinary chondrites (including St. Severin) by Ebihara and Honda (1984). For St. Severin, 94% of P was extracted by EDTA and 6M HCl leaches; whereas only 57% of the U was leached, arguing that 43% of the U is not associated with phosphates (M. Ebihara, personal communication). However, the missing 6% of P could represent apatite grains separated with the magnetic fraction, or small grains sealed on the boundaries of binary grains and therefore difficult to leach. If all of the U is associated with phosphates, these small apatite grains might have much higher U concentrations than easily leachable larger phosphates, accounting for 43% of the total U. This could also reconcile the higher model apatite U concentrations (average for whole meteorite) in Figure 3.3.6, with the lower $U_{apatite}$ concentrations measured in large grains (Table 3.3.1). In unequilibrated ordinary chondrites, most of U located in chondrule glass, whereas most of P is in metal. In regions with low P and high U (i.e., chondrule glass) isolated from equilibration with big phosphates associated with metal, small U-rich phosphate grains will not grow during metamorphism, explaining the inferred correlation of the grain size and U concentrations. Finally, it is worth noting that, if the Th/U vs. 1/U systematics for equilibrated ordinary chondrites were dictated by four components (two phosphates, inert material and the 43% non-phosphate carrier), then it would be surprising to observe the correlations shown in Figures 3.2.1 and 3.2.2.

Direct observations on unequilibrated ordinary chondrites (e.g., Yabuki and El Goresy 1986) and inferences from petrographic associations of metal and phosphates in equilibrated ordinary chondrites (e.g., Jones *et al.*, 1980; Murrell and Burnett, 1983), especially an excess of coarse phosphate grains at the margins of metal in the metal-rich

Portales Valley chondrite (Ruzicka et al. 2000), indicate that, prior to metamorphism, P was associated with metal. Association with sulfide cannot be ruled out and P-rich sulfides are reported in CM chondrites (e.g., Bunch et al. 1979, Nazarov et al. 1997). However, the phosphate-sulfide preferential associations are probably best interpreted as FeS formation from a P-rich metal followed by (or simultaneous with) nucleation of a phosphate during metamorphism. The alloying of P in Fe-Ni metal is a predicted consequence of calculations of gas solid equilibrium under solar nebular conditions (e.g., Grossman and Olsen, 1974).

Parent body conditions appear to have been sufficiently oxidizing that phosphates formed early, even in the most primitive chondrites (Yabuki and El Goresy 1986). Phosphate nucleation probably occurred primarily on metal grain boundaries, preserving the preferential association with large metal grains observed in equilibrated chondrites. Large (100 micron) phosphate grains are rare in unequilibrated ordinary chondrites but common in equilibrated ordinary chondrites. Thus, continued growth on some phosphate nuclei at the expense of others over the duration of re-crystallization has produced relatively large phosphate grains which in turn produced a gm-scale heterogeneity in the P concentrations. We have documented that this is quite large in Harleton, but Harleton is likely anomalous in this respect. For an order of magnitude larger sample size, the data of Von Michaelis *et al.* (1969) indicate that equilibrated ordinary chondrite P contents are remarkably homogeneous.

Both apatite and merrillite are observed in unequilibrated chondrites (Murrell and Burnett, 1983; Yabuki and El Goresy, 1986), but petrographic observations to date cannot distinguish which phase formed first.

Similarly, the host phases in which Cl entered into ordinary chondrites are poorly constrained. Besides apatite, other Cl-rich phases in ordinary chondrites are rarely observed, such as lawrencite ($FeCl_2$) and halite (NaCl). Lawrencite was described in only one, unusually high-Cl, L6 chondrite Gomez (Sipiera et al., 1980). Halite has been found in ordinary chondrites of intermediate petrographic grade (Zolensky, 1999), and if it is indeed a hydrothermal mineral, it may have formed very early. If halite was a major source of Cl in ordinary chondrite parent bodies, its apparently gradual destruction during metamorphism may have produced a transfer of the Cl to apatite. The survival of halite in intermediate grade chondrites might indicate that the first formed phosphates were merrillite, followed, possibly relatively quickly, by apatite. However, limited by the chondritic P/Cl abundance ratio, conversion to apatite was only partial. This scenario is supported by the rarity of the observed apatite grains in the low petrographic grade ordinary chondrites (Yabuki and El Goresy, 1986).

Regardless of details, several authors have noted the great variability (up to a factor of 20) of chondritic Cl concentrations (e.g., Reed, 1971) or of the apatite/merrillite ratio (e.g., Pellas and Storzer, 1975). It is plausible to regard this heterogeneity as representing the 'freezing-in" of a heterogeneous Cl parent body distribution on a more uniform distribution of early nucleated merrillite grains. The coarsening of phosphates during metamorphism has not produced a more homogeneous distribution of apatite. This is probably because the apatite/merrillite heterogeneity is only a property of the larger, more easily observed phosphates and that most apatites are really very fine-grained as discussed above. Based on our study it is unlikely that Unruh's (1982) high Th/U measurements (see Table 3.2.1) accidentally happened to sample three different parts of one rock, all with "anomaleously" low Cl content. Unruh's samples are fairly small, ~100 mg, so it is likely that Cl variations have to be on a much larger scale, with Unruh samples all coming from a low-Cl region.

In unequilibrated chondrites, U and Th are concentrated in chondrule mesostasis (Murrell and Burnett, 1983) like other refractory lithophile elements. Phosphates in unequilibrated chondrites have much lower U and Th concentrations compared to those of phosphates in equilibrated chondrites (Crozaz *et al.*, 1989; Murrell and Burnett, 1983). Thus, the migration of U and Th (and other lithophile elements) into phosphates occurs gradually over the epoch of chondritic metamorphic recrystallization. It is plausible to assume that the strong partitioning of U into apatite forces a heterogeneous U distribution, matching the frozen-in initial chlorine distribution.

3.5 An improved solar system Th/U

As noted in the Introduction, cosmochronology models require precise knowledge of the average solar system Th/U. Moreover, a significant scatter in Th/U in CI chondrite analyses (Rocholl and Jochum, 1993) makes this traditional source of solar system abundances unreliable. Relative abundances of other refractory lithophile elements are indistinguishable between CI and ordinary chondrites (Larimer and Wasson, 1988). Consequently, ordinary chondrites are expected to provide a valid average solar system Th/U, although additional tests of the equality of refractory lithophile abundances between ordinary and CI chondrites would be important.

Available high precision Th/U for ordinary chondrites prior to this study showed significant variations well outside of analytical errors. It was tempting to average these data in the hope of obtaining an improved solar system Th/U. However, in the absence of any understanding of the causes of the variations, one could not rule out that the average solar system Th/U was the minimum or the maximum of the range, as opposed to the average.

Our study shows that the observed Th/U variations in equilibrated ordinary chondrites are produced by the redistribution of U and Th among the co-existing phosphate phases, coupled with fluctuations in the sampling of apatite grains in gram-sized ordinary chondrite specimens. *With sampling established as the cause of the observed variations, a sample-mass-weighted average of high precision ordinary chondrite Th/U should give an improved average solar system Th/U.* This conclusion is supported by the data of Von Michaelis *et al.* (1969), which show that ordinary chondrite P abundances converge to precise values when large samples are analyzed.

Thus,

$$(\mathrm{Th/U})_{\mathrm{weighted}}=\Sigma\{(\mathrm{Th/U})_i*g_I\}/\Sigma g_I\ ,$$

and

$$\sigma^2_{\mathrm{mean}}=\Sigma\{g_i*[(\mathrm{Th/U})_i-(\mathrm{Th/U})_{\mathrm{weighted}}]^2\}/N\Sigma g_i$$

where g_i is the mass of i sample and N is a number of the samples in the set with $g_i>0.5$ gr.

The calculated weighted Th/U of Harleton and weighted Th/U for other ordinary chondrites are listed in Table 3.5.1. In this table we present weighted averages for OC data as well as arithmetic Th/U averages for comparison. Calculated σ_{mean} is given in the brackets.

Calculation of weighted averages separately for Harleton and other ordinary chondrites is a test of our approach since the total mass of analyzed samples of Harleton (9.3 grams) and other meteorites (13 grams) is comparable. The OC weighed average is highly sensitive to one 1-gram sample of Glatton (Chen *et al.* 1993 and private communication). This sample is anomalous in two respects: first, this sample falls $>4\sigma$ from the weighted average, and second, the high Th/U in this sample is due to enriched Th. Other (this work and Unruh, 1982) high Th/U whole rock data are mostly due to U depletion. Thus, the Chen *et al.* (1993) Glatton sample can be considered truly anomalous. In Table 3.5.1 we present data for Harleton (line 1); other than Harleton OC literature data (line 2), and OC data omitting the anomalous Glatton analysis (lines 3 and 4). The striking result is that weighted averages of Th/U for Harleton and other OC (without Glatton sample) strongly converge to a value of 3.53.

If, as it was discussed at the end of the previous section, strong partitioning of U into apatite forces a heterogeneous U distribution, matching the frozen-in initial chlorine distribution, then the whole rock analyses of unequilibrated chondrites should converge more readily to the average chondtritic value because of a more homogeneously (on a 1 gram scale) distribution of the chondrule mesostasis. Indeed the average of 5 available analyses of L4 chondrites (Bjurbole and Tennasilm, included in the Figure 3.2.2) is 3.55±0.10.

It is necessary to note that almost all of the literature ID data of OC are for L-type chondrites. However, the relative abundances of refractory lithophile elements are the same in all ordinary chondritic groups and CI, thus the L chondrite bias in the Th/U data should not make a difference for solar system abundance calculations.

The identification of U as a refractory lithophile element can be questioned. High Th/U ratios in Allende CAIs (e.g., Chen and Tilton, 1975; Boynton, 1978) are usually interpreted as reflecting a lower condensation temperature for U. However, the general issue may be much more complex as suggested by a systematic study of CAIs in Mighei (CM2) by MacPherson and Davis (1994), who found Th/U ratios ranging from 1 to greater than 18. Depletions of moderately volatile elements with condensation temperatures significantly below that of U (e.g., Cr, Mn, Li, Na) in ordinary chondrites are not large (≤20%; Palme et al., 1988), but the possibility of the ordinary chondrite Th/U being slightly higher (~ 10%?) than the average solar system value cannot be ruled out.

Table 3.5.1 Calculated average Th/U for ordinary chondrites.

	Weighted average[1]	Arithmetic average
Harleton	3.53 (0.20)	4.12 (0.42)
OChondrites[2], w/o Harleton	3.71 (0.24)	3.55 (0.19)
OC, w/o Harleton and Glatton[3]	3.53 (0.14)	3.46 (0.13)
Ordinary Chondrites[4]	3.53 (0.10)	3.67 (0.20)
A&G[5]		3.63 (0.37)

[1] See equation (4) and explanation in the text for weighted average and $1\sigma_{mean}$ (in brackets).
[2] Literature (Tatsumoto et al. 1973; Unruh, 1982; Hagee et al. 1990; Chen et al. 1993; Shinotsuka et al. 1995) and this study data for H, L and LL 4-6, omitting Harleton. Multiple measurements of the same meteorite are treated as separate samples. Total 31 samples, of which one is H5, 5 are LL6 and the rest are L4-6.
[3] Same as above, with 1 Glatton sample (Chen *et al.* 1993) omitted (see text for explanation).
[4] Combined literature (Glatton omitted) and Harleton analyses from Unruh (1982) and this study.
[5] Anders and Grevesse 1989 value for Solar System abundances, based on CI chondrites.

Chapter 4: Carbonaceous chondrites

4.1 Th/U variations in carbonaceous chondrites

As discussed in the introduction, carbonaceous chondrites show a surprisingly big scatter in Th/U ratios, mostly because of U variations (see Figure 1.1). Restricting our discussion only to high-precision isotope dilution (ID) literature data, Figure 4.1.1 plots Th/U versus 1/U for CI (Orgueil, Ivuna), CM2 (Mighei, Murrey, Murchison, Nogoya and Yamato 74-662), CV3 (Allende) and CO3 (Lance, Ornans). The simplest interpretation of the positive linear trends in Th/U vs. 1/U is two-component mixing between high Th/U, low U and low Th/U, high U endmembers, strikingly analogous to what observed in ordinary chondrites (Figure 3.2.2). Samples within every group appear to yield linear trends, although the trend is less defined for CM chondrites. Trends in the Figure 4.1.1 seem to converge at the same value, possibly a common high-U endmember. Rocholl and Jochum (1989) consider apatite to be a possible endmember, because apatites are reported as trace phases in carbonaceous chondrites and because apatites in ordinary chondrites are enriched in Th and U, and tend to have Th/U ratios around unity.

Objectives of the carbonaceous chondrite study are (1) to test whether phosphates are the cause of the heterogeneous distributions of Th/U shown in Figure 4.1.1, and (2) to determine other possible processes for redistribution of actinides within parent body (such as aqueous alteration).

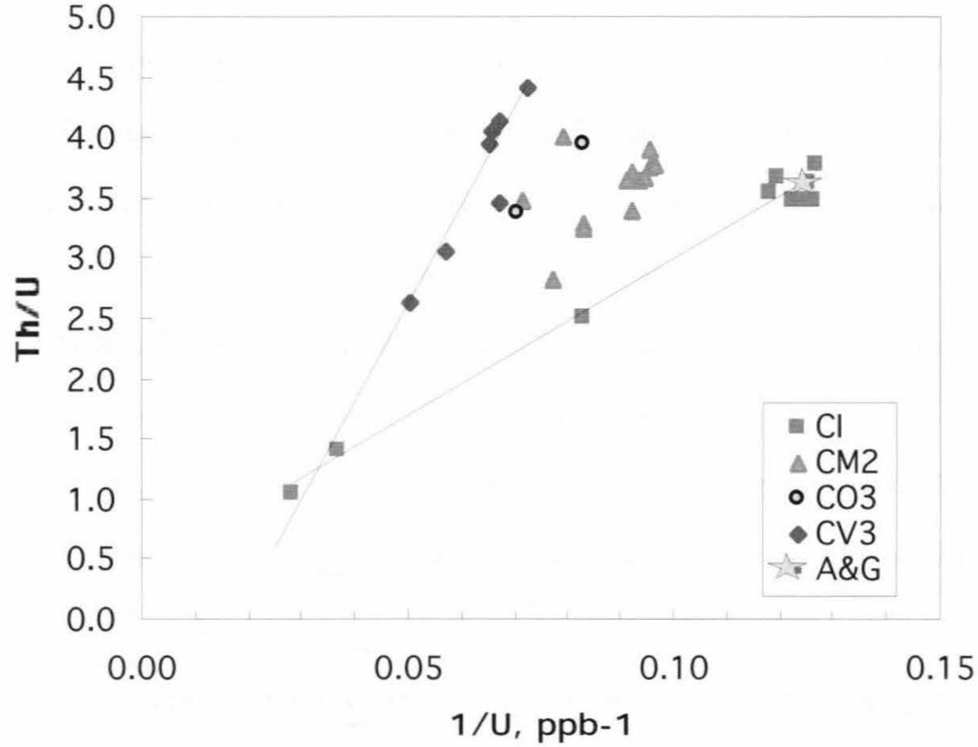

Figure 4.1.1 Th/U vs. 1/U plot of the whole rock ID Th/U analyses for Carbonaceous Chondrites (data from Tatsumoto et al., 1976, Rocholl and Jochum, 1993 and J. Chen, personal communication). Different types of carbonaceous chondrites display linear trends with different slopes. Large variations in Th/U are apparent for CI and CV3 chondrites. Star is Anders and Grevesse (1989) value.

4.2 CI chondrites

The bulk compositions of CI chondrites are a very close match to the composition of solar photosphere (Anders and Ebihara, 1982), excluding a few volatile elements and Th/U (Chapters 1 and 3), hence, the elemental abundances in bulk CI chondrites are used as a reference composition for other types of solar system materials. In general, the other groups of carbonaceous chondrites are enriched in refractory lithophile elements relative to CI, both in absolute concentrations and in Si-normalized ratios, presumably because of the presence of refractory Ca-Al-rich inclusions (CAI).

Petrographically, CI chondrites are constituted almost entirely of fine-grained, opaque matrix material, with virtually no chondrules (<<1%, see Brearley and Jones (1998) for review).

A remarkable characteristic of CI chondrites is the fact that despite being the "most primitive" composition among solar system materials, CI chondrites are the most severely hydrothermally altered. Their matrices consist mostly of very fine-grained phyllosilicate minerals (60-50%) with imbedded magnetite crystals and a variety of accessory sulfides, carbonates and sulfates. Minor phases include Ca-phosphates (e.g., Endress and Bischoff, 1996).

CI leaching experiments

The only attempt to distinguish between different actinide carriers in CI-type chondrites was made by Chen et al. (1993). In this work a number of stepwise leaching experiments were performed for the Orgueil sample. The Chen et al. (1993) results are included in the Table 4.2.1. These showed that there is a large degree of Th/U fractionation in different leaches. The dilute acids (acetic and 0.1 M HCl) removed about 35% of total U, but only few percent of Th.

The presence of these easily leachable sites with relatively high U concentration and low Th/U ratio could be the cause of the variations in Th/U, mostly due to U variations, in whole rock CI chondrites as shown in Figure 4.1.1 and Table 4.2.1. It is evident that a large fraction of U in Orgueil resides in sites which may have been produced by aqueous alteration. Such phases are most likely carbonates or sulfates. Other plausible U-enriched phases would be phosphates, which may or may not be a product of the hydrothermal alteration.

In order to test whether high Th-U phosphates are the cause of the heterogeneous distribution of U and Th in Orgueil, we analyzed phosphorus concentrations in exactly the same leaches in which Th and U were previously determined by Chen et al. (1993). For TIMS analyses, Chen et al. (1993) extracted U and Th via anion exchange column, collecting and combining all elutes other than the U, Th fraction. There is no evidence of P being in the same elute as actinides (Kraus and Nelson, 1958).

Phosphorus was analyzed as described in Chapter 2. The total phosphorus content for the Chen et al. (1993) sample (sum of all elutes) came to 1035 ppm. In CI chondrites, average phosphorus concentration is 1180 ppm (Anders and Greveesse, 1989). This confirms that there was very little or no P lost in Chen et al. (1993) chemistry.

Table 4.2.1 shows that very little P is associated with easily leachable phases, enriched in U. Most of the P (87%) came out in the same stage (6N HCl) that is enriched in both U and Th, but with a high, not low, Th/U. This experiment shows that Th/U variations in CI chondrites are likely dictated by the presence of 2 major actinide carriers:

(1) easily leachable phases, rich in U and very little Th, most likely carbonates and sulfates, and (2) 6NHCl- leachable phase enriched in both actinides, with relatively high Th/U (~6), possibly phosphates, although the correlated release of actinides and P could also be coincidental. So, for CI chondrites, variations in whole rock Th/U ratios can be explained solely by the redistribution of actinides (mostly U) by the aqueous fluid into secondary mineral phases. The linear trend seen in Figure 4.4.1 is produced by mixture of low- and high- Th/U phases.

The observation of uranium redistribution during hydrothermal alteration is not surprising, because upon oxidation to higher valence states, this element becomes more mobile, staying in the aqueous fluids and depositing as alteration phases with fractionated actinides.

Table 4.2.1 U, Th and P analyses of Orgueil (CI).

	U,%[1]	Th %[1]	U, ppb[2]	Th, ppb[2]	Th/U	P, %	P, ppm[2]
Leaching exp.							
HAc	21	1	1.57	0.23	0.15	1.4	14.6
0.1M HCl	14	5	1.07	1.46	1.36	1.1	11.2
6M HCl	55	81	4.16	23.43	5.63	87.2	903
7M HNO3	7	10	0.57	2.95	5.16	9.6	99
Residue	3	3	0.21	0.77	3.57	0.8	7.9
Total	100	100	7.59	28.8	3.80	100	1035
Whole rock							
Orgueil[3]			8.2	28.6	3.45		
Orgueil-1[4]			12.1	30.4	2.51		
Orgueil-2[4]			8.0	29.2	3.65		
Orgueil-3[4]			8.5	30.3	3.56		
Orgueil-536[5]			8.4	31.0	3.69		
Orgueil-T [5]			7.9	27.8	3.51		
Orgueil-T [5]			7.9	30.0	3.80		
Org-318/1-1[5]			27.4	39.1	1.43		
Org-318/1-2[5]			36.0	38.0	1.06		

[1] From Chen et al. 1993

[2] Concentrations in leaches (ppb) are in ng of element in the leach per total mass of the initial sample.

[3] Tatsumoto et al. 1976

[4] J. Chen, personal communications

[5] Rocholl and Jochum, 1993

4.3 CM2 chondrites

CM2 chondrites are more petrologically and chemically heterogeneous than CI. While the CI consist almost entirely of fine-grained material, the matrix in CM occupies only 70% by volume (Brearley and Jones, 1998). Other constituents include chondrules (20%), refractory inclusions (5%), isolated olivine grains and sulfides. Metal is rare in CM2 chondrites (0.1% by volume), with Fe present as Fe-oxides and sulfides. Matrix material consists mostly of hydrous phases, which are believed to be products of hydrothermal alteration of a fine-grained anhydrous precursor (see Brearley and Jones, 1998 for review). Chondrules and CAIs also have been altered to a different degree by hydrous fluids in different CM chondrites (e.g., Clayton and Mayeda, 1989). Analogous to CIs, aqueous alteration of CM chondrites could produce redistribution of U by hydrothermal fluids and fractionate Th and U if conditions are sufficiently oxidizing. Carbonates and sulfates occur as major phases in CM matrices, as well as secondary alteration phases in CAIs (Brearley and Jones, 1998, MacPherson and Davis, 1990). Cl-free apatite was found in the matrix of the Cochabamba CM chondrite (Muller et al., 1979).

In addition to aqueous alteration, the heterogeneous distribution and mineralogical and chemical diversity of refractory inclusions in CM2 chondrites can affect the whole rock Th/U ratio. Refractory inclusions appear to be the first materials formed in the solar nebula, but have very complex evolutionary histories. Thermodynamic calculations of the condensation temperatures of U and Th in the solar nebula show that Th is slightly more refractory than U. Differences between 50% condensation temperatures (K) of Th and U at different pressures and C/O ratios are from 10 to 100°K U (Kornacki and Fegley, 1986, Lodders and Fegley, 1993). So refractory inclusions in carbonaceous chondrites might not reflect the solar Th/U ratio.

A thorough ion probe study of bulk major and trace element compositions of the refractory inclusions from Mighei (CM2) chondrite was done by MacPherson and Davis (1994). Figure 4.3.1 shows whole rock ID analyses for CM2 chondrites as well as in-situ analyses of the refractory inclusions from Mighei. Refractory inclusions exhibit a wide range of Th/U (from 1 to 20). Surprisingly, in spite of the big error bars on the ion probe data points, refractories also seem to follow a positive trend in Th/U vs. 1/U coordinates.

The objectives of CM-chondrite study are similar to CI-chondrites: (1) To test whether phosphates are the cause of the heterogeneous distribution of Th/U, and (2) to determine other possible processes for redistribution of actinides within parent body (such as aqueous alteration).

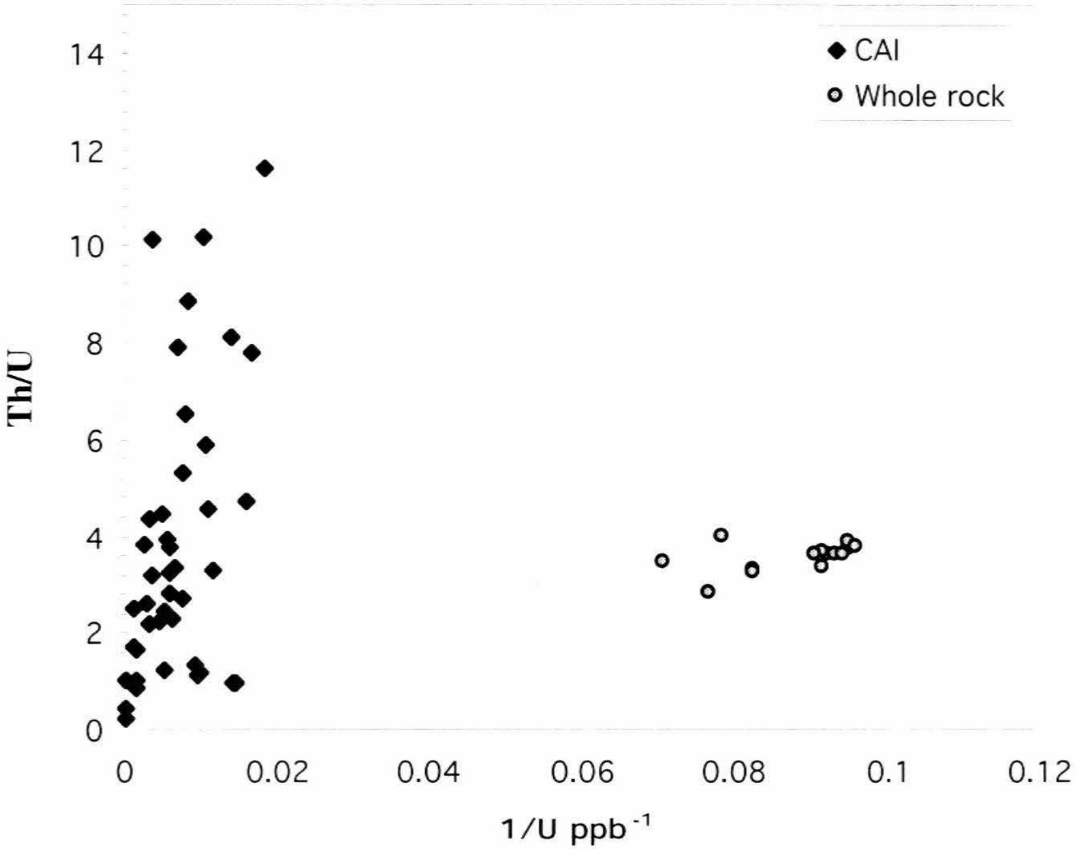

Figure 4.3.1 Th/U vs. 1/U plot for CM2 chondrites. Whole rock analyses same as in Figure 4.1.1, CAI – ion probe data from MacPherson and Davis (1994).

CM leaching experiments

The Murchison CM2 meteorite was chosen for this study. We have performed leaching experiments in order to distinguish between different actinide carriers. To gain a qualitative understanding of high and low U components, we have tried to distinguish U and Th associated with carbonates, sulfates, phosphates, matrix material (phylosilicates) and with chondrule plus CAI material.

Leaching experiments are challenging to interpret because of the tendency of dissolved elements to precipitate from the solution and readsorb on the residues. For Th this tendency is especially well known. Without isotope dilution, measured Th concentrations might be significantly lower than the real concentration in the leached phase. So one should be careful in choosing the reagents and conditions of the experiment (such as temperature and duration).

Three pieces of the same fragment of Murchison (Me2683) were surface cleaned with a diamond dental drill and rinsed in spectroscopic grade methanol. Sample Mu1 was spiked and dissolved following the technique described in Chapter 2.4. Sample Mu2 was: 1) subjected to ultrasonic digestion for 15 minutes in 3 ml 1.6M HNO_3; 2) sample was centrifuged, leachate separated and spiked; 3) 3 mlH_2O was added, centrifuged, and the leach combined with the one separated in the step 2. Step 3 was performed one more time. The combined solution is Mu2-leach in the Table 4.3.1. The residue (sample Mu2-residue) after leaching was spiked and dissolved following Chapter 2.4. The results of the Mu2 leach were not definite, so a more elaborate experiment was designed to distinguish between different easily soluble phases.

Sample separation for Mu3 is illustrated in the schematic diagram Figure 4.3.2. Mu3 was carefully (not to break chondrules and CAIs) crushed in a stainless steel pestle, and separated into two fractions – fine (MuF) and coarse (MuC). Separation was performed using 270 mesh (53 μm) Nylon screen under methanol. The goal was to have the MuF fraction be a relatively pure matrix material. Consequently, the MuC fraction does have matrix lumps, in addition to expected constituents of the coarse fraction. The fine (<53 μm) fraction was divided into two splits MuF1 and MuF2. MuF1 was spiked and dissolved.

The coarse (>53 μm) fraction was divided into two splits: MuCsp1 and MuCsp2. Split MuCsp1 was put aside for the future study. Split MuCsp2 was powdered and split in two: MuCsp2a and MuCsp2b. Sample MuCsp2b was spiked and dissolved.

Samples MuF2 and MuCsp2a underwent stepwise leaching. Parallel to the samples, blank solutions were carried through the same steps. In the Figure 4.3.2, three leaching steps are indicated:

1. HAc. Carbonates and sulfates dissolve readily in acetic acid (HAc). The duration of the HAc leaching step was short to minimize time for Th precipitation. For preparation of the samples MuF2-1 and MuCsp2a-1, one ml 10% HAc was added to the samples, allowed to sit for 5 minutes at room temperature, periodically hand shaken, and then digested ultrasonically for 5 minutes. For the separation of the leach from the residue, samples were centrifuged using 2 ml Nalgene acid-cleaned centrifuge vials with a 0.2 mm Nylon filter insert (Figure 4.3.3). All following residue-leach separations were performed using these centrifuge vials. Solution was removed from the lower part of the vial, and Th-U spike was added. An additional 0.4 ml of HAc was added right on top of

the filter and centrifuged. This solution was combined with the spiked portion. Two additional 0.4 and 0.6 ml H_2O rinses were made and the rinse solution combined with previous solutions.

2. NH_4-EDTA. Ebihara and Honda (1984) have demonstrated that ammoniacal EDTA (preparation of the reagent described in the Section 2.4) efficiently attacks phosphates. Additional experiments on the dissolution of powdered (~200 μm) apatite grains in EDTA were performed to show that the dissolution works and to determine a sufficient duration for the phosphate dissolution. We performed test experiments to determine whether Th stays in EDTA solution without adsorbtion on the solid residue. ^{230}Th spike was added to scrap powdered material from Murchison and leached with NH_4-EDTA for 7 hours at room temperature. After centrifugation, the sample powder was rinsed with fresh EDTA 3 times. The leach and rinse solutions were combined for analysis. The procedure above was repeated 2 more times.

Finally, the solid residue was dissolved and analyzed along with the leaching solutions for the presence of ^{230}Th. The results of this experiment showed that Th complexes, formed upon reaction with NH_4-EDTA, keep Th in solution. Approximately 96% of ^{230}Th from the spiked amount came out with the first EDTA leach, and an additional 4% was in the following EDTA rinse. The following leaching steps as well as the dissolved residue did not carry detectable amounts of ^{230}Th.

For preparation of the samples MuF2-2 and MuCsp2a-2, 0.6 ml of ammoniacal EDTA solution was added to the residue in the centrifuge vial. These were left for reaction for 7 hours at room temperature. The leach was centrifuged, separated, and spiked. Additional rinses were made with one additional ml of NH_4-EDTA and one ml of H_2O. The rinse solutions were combined and added to the original leach.

3. NH_4-EDTA (re-extract). Preparation of the samples MuF2-3 and MuCsp2a-3 was as in step 2.

4. Dissolution of the residues MuF2-4 and MuCsp2a-4. Inserts from the centrifuge vials, carrying residual samples on top the filter, were removed and placed up-side down into screw-cap Teflon beakers with 1.5 ml 0.5N HCl. Ultrasonic digestion for 15 minutes was performed to separate sample from the filter. The filter was removed and cleaned an additional two times in the ultrasonic bath in HCl. The HCl solutions and sample residues were combined, spiked, and the excess HCl evaporated. Mixture of concentrated HF, HNO_3 and $HClO_4$ were added for dissolution as described in Chapter 2.4.

Results

Analytical results for U, Th and P from Murchison are listed in Table 4.3.1. For Th and U the analytical blank was of the order of 10^{-14} g, which is significantly lower than most of the samples analyzed. A blank space for U, Th or P in Table 4.3.1 means concentrations below blank levels.

The Th/U ratio of the whole rock shows large variations between 2.85 and 4.5. It is evident, that unlike CI and OC whole rock analyses, Th/U variations in CM2 chondrites are mostly due to Th variations.

The whole rock sample Mu1 has the highest U, Th and Th/U. This suggests that this sample might contain excess of CAI material.

Leaching of the whole rock sample Mu2 shows that about half of the U, Th and most of the P are in 1.6 M HNO_3-leachable phases. These include carbonates, sulfates, sulfides, and phosphates. However, some of the chondrule mesostasis and silicate material may have been leached as well, making the results of this experiment somewhat ambiguous. Th/U ratio in the 1.6 M HNO_3 is somewhat lower than the whole rock ratio, suggesting the presence of more soluble U-rich phases.

Unlike Mu1, total U and Th concentrations in Mu2 are not elevated, probably indicating no excess of CAI material in the sample.

The amounts of U and Th leached in Mu2 compare well with those from the 6M HCl leach (sample Murchison#6 in Table 4.3.1) used by Chen et al., 1993. 60% of U extracted with 1.6 $MHNO_3$ (63% - with HCl), 53% of Th (40% - with HCl). The 6M HCl will attack the same phases as nitric acid. But Th stays better in nitric solution than in HCl.

The second leaching step of Chen et al. (1993) was $7MHNO_3$ which extracted a significant part of the U (22% of total) and approximately half (47%) of the Th. The 7M HNO_3 is concentrated enough to start dissolving more resistant silicate phases, so detailed interpretation of the 7M HNO_3 –leach data is not possible.

The U, Th analyses of the fine (matrix) separate (MuF1) and total for matrix sample MuF2 are consistent. The P contents differ by 50%. The Th/U ratio for both is low, 2.57 and 1.42 respectively. A major result is that the matrix U, Th and P contents are significantly lower than the whole rock concentrations. Whereas there are big reservoirs for U and Th in CM chondrites (chondrules and CAIs), most of the phosphorus might have been expected to be in the matrix because phosphates were observed in CM matrix (Brearley and Jones, 1998).

Results of the stepwise leaching of the matrix material are also shown in Table 4.3.1. The HAc leach, targeted to the carbonates and sulfates, removed a significant portion of U (42%) and virtually no Th (0.7%) or P, suggesting a mobile U-rich component. But on a total sample basis, this component accounts only for 10% of total U content.

Chen et al. (1993) found no U associated with 0.1 N HCl, which should have dissolved carbonates. Of course, we cannot rule out a possible particular contamination of small, low in U samples prior to chemistry. For example, to produce the amount of U "contamination" extracted in our HAc-leach (0.24ng), the sample needed to pick up 25 μg of dust with 10 ppm U concentration or ten million of 1 μm size dust particles. This seems large. It may be that our sample and and that of Che et al. (1993) are different.

The first EDTA leaching step, which preferentially dissolves phosphates, extracted ~3% of Th, 0.8% of U, and 3.6 % of phosphorus. The EDTA re-extract showed that no leachable phosphate is left in the sample. Most of the Th and P, and half of U, were left in the residue. This result provides strong evidence for the interpretation from MuF1 analyses: *P is not concentrated in phosphates*. One of the explanations is that P is actually associated with sulfides, which did not break during the separation of the fine and coarse fractions. Figure 4.3.3 shows such a Ni-Fe sulfide grain, rich in P. Cr and P-rich sulfide phases are recognized in CM chondrites (Bunch et al., 1979, Nazarov et al., 1997). Recent TEM studies suggest that these phases most likely are mixture of two phases, one of which is likely to be a phosphide (Devouard and Buseck, 1997).

The total P differs by 50% in MuF1 and MuF2, indicating that P is concentrated in relatively large, possibly sulfide, particles, thus difficult to sample representatively.

Assuming our matrix separation was successful, one can predict the concentrations of U and Th in the coarse fraction. In CM2 chondrites, matrix material constitutes 70% by volume (Brearley and Jones, 1998). Thus, from the samples MuF1 and MuF2 it follows that matrix can account only for 5% of total U and Th and for 30-50% of P. Then, the estimated Th, U and P concentrations of the non-matrix material (including chondrules and CAIs) are 105 ppb, 25 ppb and 2300 ppm respectively.

Surprisingly, the analytical data for both the coarse fractions of Murchison (sample MuCsp2b and the total of sample MuCsp2a) revealed factors of 3-5 higher actinide concentrations than was expected! Phosphorus concentrations are within the expected range.

These actinide concentrations are way too high to be explained by particulate sample contamination. Very low concentrations in fine fractions show that the overall sample was clean. The only plausible explanation is presence of an anomalously big CAI fraction in the sampled rock fragment. High U and Th concentrations in both coarse fractions MuCsp2a and MuCsp2b suggest possibly just one big CAI, which broke on further crushing after sieving. To produce the observed Th and U concentrations ~10 mm^3 CAI is required to have on the order of 1 ppm U and few ppm Th. MacPherson and Davis (1994) analyzed many CAIs from Mighei (CM2) with U and Th concentrations this high.

The split of the coarse fraction (sample MuCsp1) was investigated in order to find pieces of broken CAI. The 11 biggest chunks (~0.5 mm diameter) were mounted into the epoxy and polished. X-ray mapping for Ca and Al did not reveal CAI material among those fragments. However, in a doubly polished thin section, made from an adjacent piece to the initial rock sample, a big ~7mm diameter CAI was observed. Backscattered secondary electron image as well as X-ray maps of CAI inclusion from our Murchison sample are presented in Figure 4.3.4. No phosphates were observed within the inclusion based on a P X-ray map. The petrography of this CAI inclusion was not studied in detail, since only the presence of such big CAI inclusions is important for this study.

In the stepwise leaching of the coarse fraction of Murchison, the HAc step extracted phases carrying 4 ppb of U and unusually high (30 ppb) concentrations of Th. No phosphorus was associated with this step. So it is likely that these HAc-leachable phases are either in-situ alteration products of high Th/U CAI phases (according to MacPherson and Davis, 1993, carbonate-barring CAIs have wide range of Th/U ratios), or residual alteration products after removal of more mobile U by aqueous fluids.

An amount of phosphorus (5% of total in the coarse fraction) comparable to the matrix fraction was extracted by EDTA with very little actinide content (0.14% of U and 0.8% of Th), supporting the conclusion from the matrix leaching of the overall low phosphate content in Murchison.

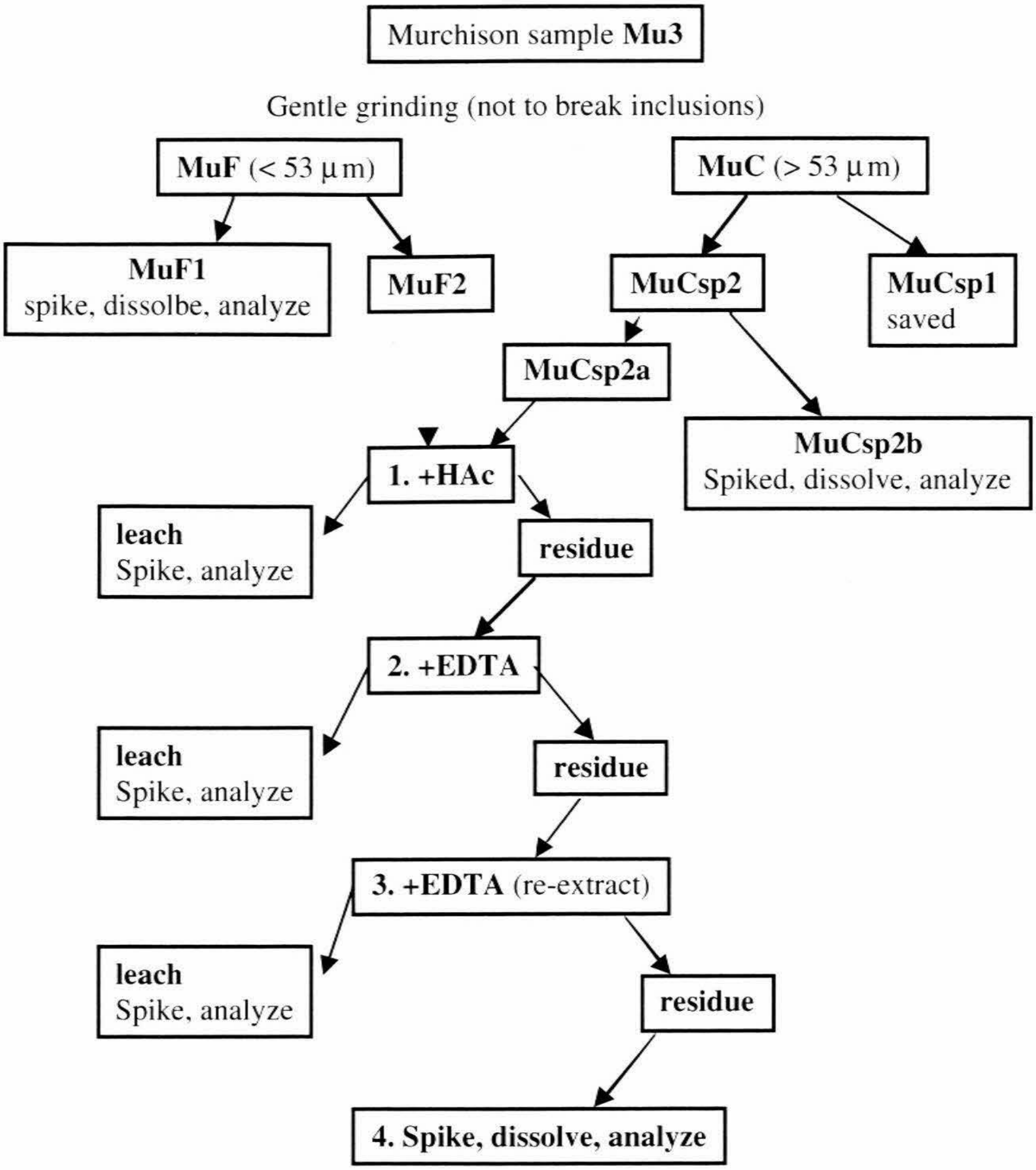

Figure 4.3.2 Schematic diagram of the sample preparation and leaching steps for the Murchison sample Mu3. Both samples MuF2 and MuCsp2a have undergone leaching steps 1 through 4.

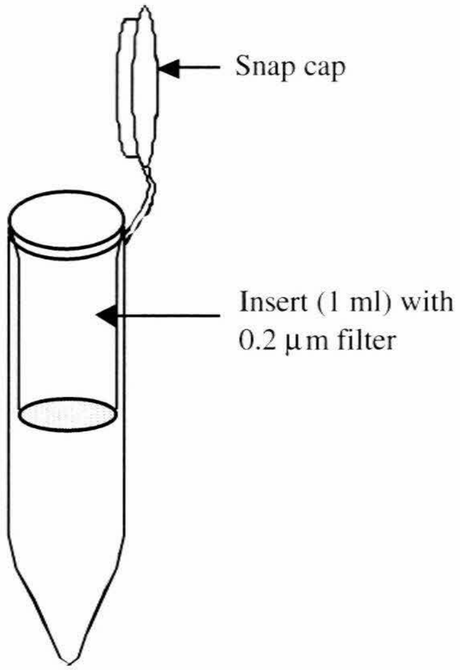

Figure 4.3.3 Illustration of the 2 ml centrifuge vial used for separation of the leaching solution from the residue.

Table 4.3.1 Murchison meteorite. Whole rock and leaching experiments analytical results.

Sample	Weight, g	Leachate	U, %	Th, %	U, ppb[4]	Th, ppb[4]	Th/U	P, %	P, ppm
Whole rock									
Mu1	0.2523				14.37	65.03	4.52	100	2212
Murchison#1[1]	0.2				12.7	51.1	4.02		
Murchison#2[1]	0.1				10.9	37.1	3.40		
Murchison#3[1]	0.2				10.5	41.1	3.91		
Murchison#4[1]	2.9				12.1	39.5	3.26		
Murchison[2]	0.181				13	37	2.85		
Murch(SIMS)[3]	0.215				10.7	39.3	3.67		
Murch(TIMS)[3]					10.6	39	3.68		
Leaching exp-ts									
Mu2-leach		1.6MHNO$_3$	60.05	53.05	7.27	20.65	2.84	81.9	1925
Mu2-residue		residue	39.95	46.95	4.83	18.28	3.78	18.1	425
total	0.574		100	100	12.10	38.93	3.22	100	2350
MuF1	0.0325	none	100	100	2.714	6.985	2.57	100	548
MuF2-1		HAc	41.6	0.67	1.512	0.035	0.023	-	-
MuF2-2		EDTA	0.8	2.82	0.029	0.146	4.95	3.60	13
MuF2-3		EDTA	-	0.95	-	0.049	-	0.02	0.06
MuF2-4		residue	57.6	95.6	2.097	4.952	2.36	96.38	348
total	0.158		100	100	3.639	5.182	1.42	100	361

Table 4.3.1 Cont.

Sample	**Weight, g**	**Leachate**	**U, %**	**Th, %**	**U, ppb[4]**	**Th, ppb[4]**	**Th/U**	**P, %**	**P, ppm**
MuCsp2a-1		HAc	6.07	10.88	4.14	29.2	7.05	-	-
MuCsp2a-2		EDTA	0.14	0.79	0.09	2.13	21.9	5.17	168
MuCsp2a-3		EDTA	-	0.63	-	1.70	-	0.004	0.14
MuCsp2a-4		residue	93.79	87.70	63.97	235.6	3.68	94.83	3082
total	0.2228		100	100	68.20	268.6	3.94	100	3250
MuCsp2b	0.1884	none	100	100	133.4	417.7	3.13	100	2730
Murchison#5[1]		water	0.05	0.008	0.005	0.003	0.68		
		0.1M HCl	0.04	0.001	0.005	0.0005	0.1		
		residue	99.9	100	10.33	39.46	3.79		
total	3.1		100	100	10.34	39.46	3.80		
Murchison#6[1]		6MHCl	63	40	6.78	15.68	2.29		
		7M HNO3	21.5	47	2.31	18.70	8.04		
		residue	15.6	13.4	1.69	5.31	3.12		
total			100	100	10.78	39.69	3.66		

[1] Chen et al., 1993. TIMS analyses.

[2] Rocholl and Jochum, 1993. ID-SIMS analyses. Precision for Th/U is 3%.

[3] Rocholl and Jochum, 1993. ID-SIMS and TIMS analyses of the same aliquot. Precision for Th/U is 3% and 0.3% respectively.

[4] Concentrations in leaches (ppb) are in ng of element in the leach per total mass of the initial sample.

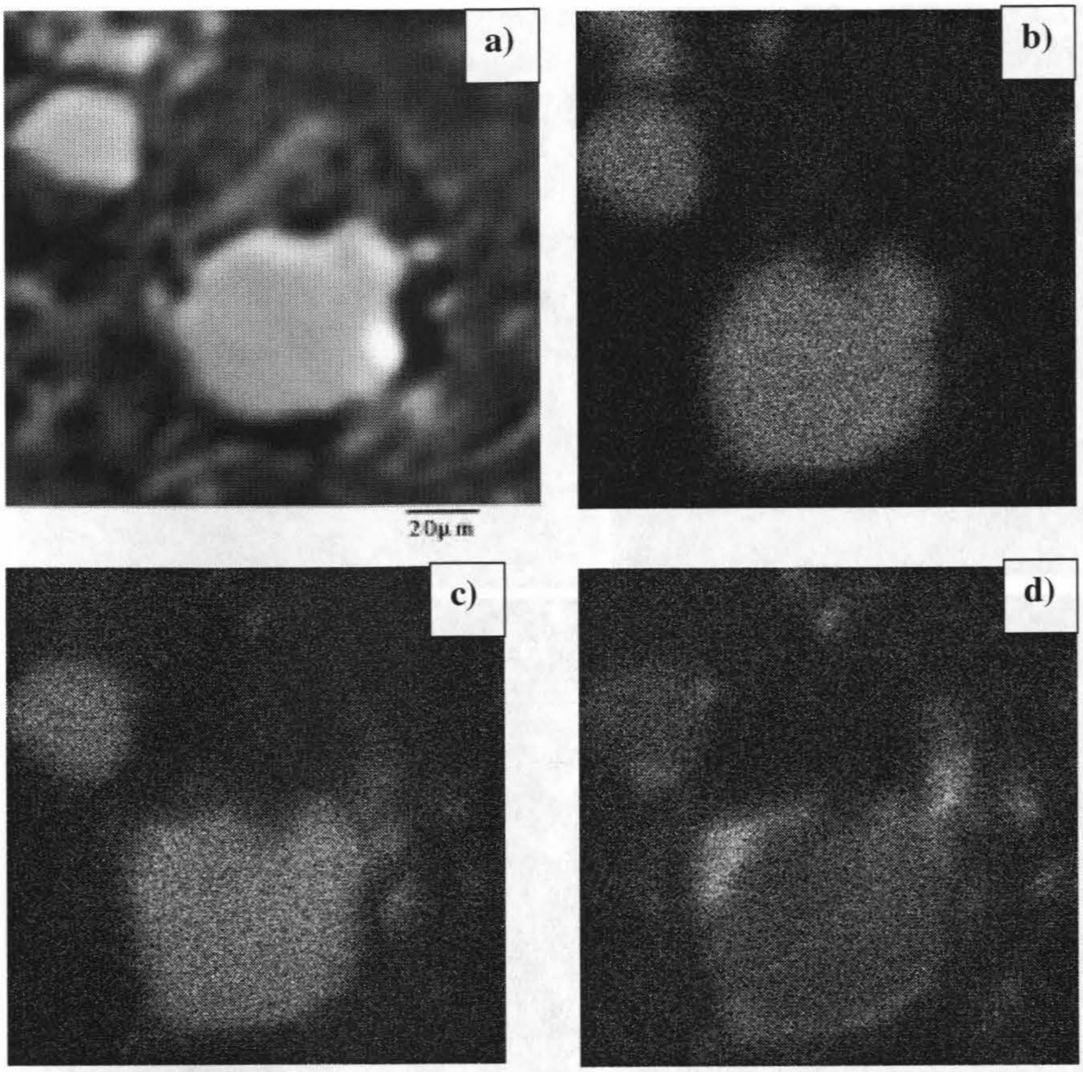

Figure 4.3.4 Ni-Fe-silfide grain from Murchison a) BSE SEM image; X-ray map for b) Ni, c) P, and d) Ca of the same sulfide grain. Ca-enrichment on the edge of the grain is likely oxidation, probably beginning of the Ca-phosphate formation.

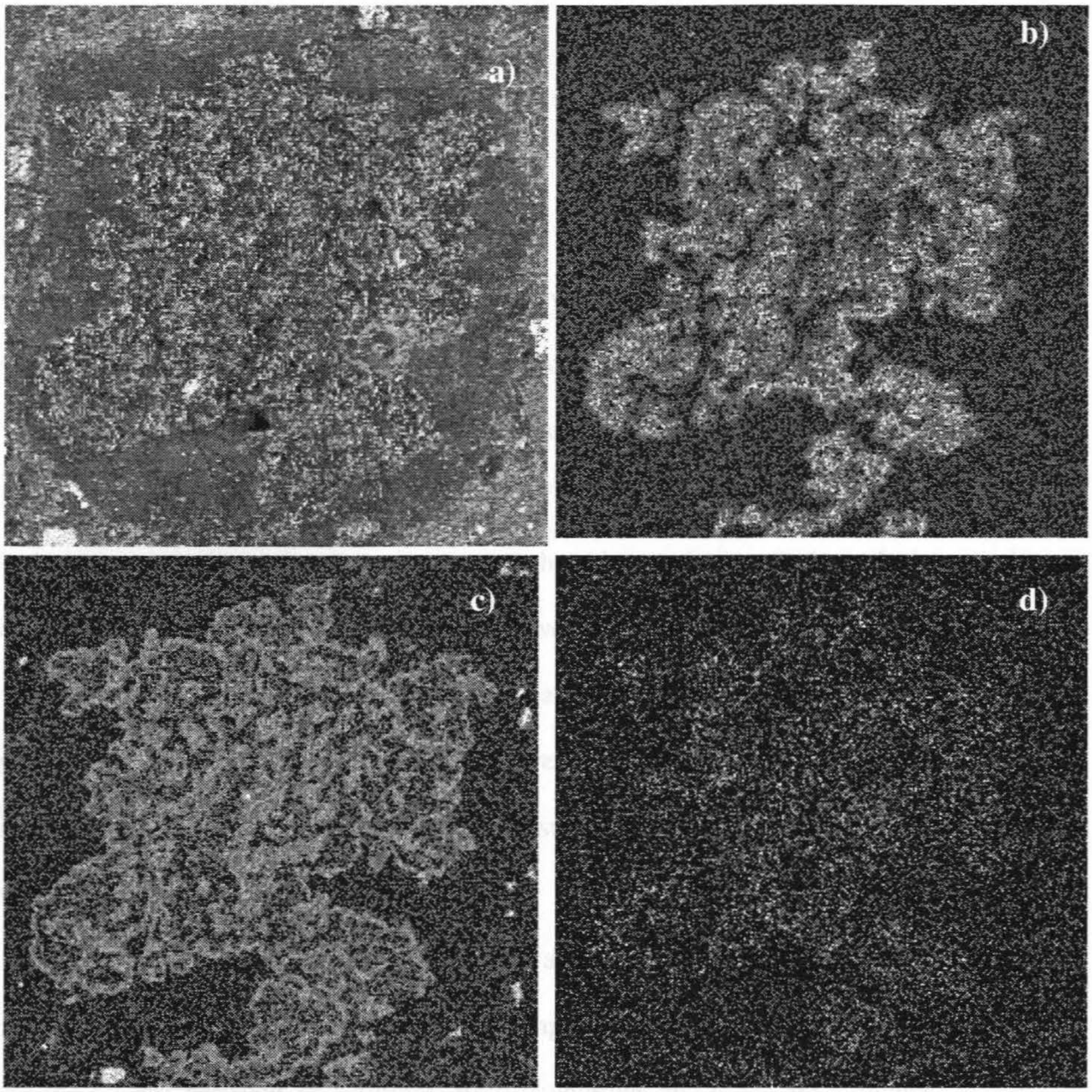

Figure 4.3.5 CAI inclusion from Murchison meteorite. a) SEM BSE image of the inclusion b), c), and d) – X-ray maps for Al, Ca and Ti correspondingly. Width of all images is 7 mm.

4.4 Interpretations

From our size separation and leaching data it is evident that the distribution of Th/U in CM2 chondrites cannot be described by mixture of only 2 high- and low-U components. Figure 4.4.1 combines literature and whole rock data from this study, including the matrix and coarse fractions. If two-component mixing exists, we would expect data from the matrix separates and the coarse fraction to fall on the same linear trend. They clearly do not. Presumably, whole rock compositions can be reconstructed by mixing matrix with an appropriate amount of coarse fraction to produce data points laying on a pseudo-mixing line. However, when the complete whole rock data set is considered, there is very little correlation observed.

Unlike the CMs, the Th/U data in ordinary and CI chondrites can be described by pseudo-mixing of only two components. There is a mixing of two phosphates with an inert material in ordinary chondrites, and redistribution of uranium into carbonates and sulfates in CI chondrites.

Figure 4.4.1 shows that, in fact, there are more than 2 components involved in producing variations in Th/U. Two of the components are chondrules and CAIs, which are the biggest reservoir of actinides. Both chondrules and CAIs are combined in our coarse fraction, although in fact, they represent two different reservoirs.

As shown in Figure 4.3.1, CAI materials have a wide range of Th/U. Because of this variability, CAIs cannot be considered as one single component. A linear trend in Th/U vs. 1/U coordinates for CAIs seems to hold. This may be a coincidence, but there are reasonable interpretations of that trend. The ion probe study of Murchison perovskites (Ireland et al., 1990) shows that this highly actinide enriched phase has Th/U well below unity. Such perovskite-bering CAIs can represent a low-Th/U endmember. Our data shows presence of high-Th/U, HAc-leachable phases (sampleMuCsp2a-1, Table 4.3.1), likely carbonate. This carbonate material could be produced either by the in-situ aqueous alteration of the high-Th/U material (complementary to perovskite?) or be a residue after removal of more mobile U by aqueous fluids. Carbonate is a common secondary mineral phase in CM CAIs (Brearley and Jones, 1998). Variations in the amount of high-Th/U carbonates in CAI materials will produce the mixing trend seen in Figure 4.3.1. If the high Th/U ratio in carbonates is a result of preferential leaching of more mobile uranium, then the hydrated matrix material should show a relatively high U content, which it does not. This work shows that the Th/U ratio in matrix is indeed relatively low (~2), and the Th/U ratio of the HAc-leachable matrix phases are below unity. But the matrix material accounts for only a very small fraction of the total rock uranium (~10%).

Chondrules in ordinary, CV3 and CO3 chondrites show small (1-2x CI composition) enrichments in refractory lithophile elements (Grossman et al., 1988). Specifically, the data of Murrell and Burnett (1983) and Chen and Tilton (1975) for ordinary and CV3 chondrites respectively, show that U and Th are similarly enriched in chondrules with respect to CI. By analogy, it is very likely that CM chondrules are also significant reservoirs of Th and U.

Contrary of the suggestion of Rocholl and Jochum (1993), our data shows that phosphates play only a minor role as actinide carrier phases in both CI and CM chondrites.

The fine-grained matrix can be regarded as another component. However, there is fractionation of Th/U within matrix material. The Hac-leachable phase has very low

Th/U, compared to the bulk matrix analyses. The matrix contains much lower concentrations of actinides compared to CI materials. Matrices in carbonaceous chondrites are often regarded as primitive, but our matrix data in Table 4.3.1 and Figure 4.4.1 clearly shows that the matrix is strongly actinide and phosphorus depleted.

The Th/U linear correlation in Figure 4.1.1 for whole rock CV3 chondrites is as good as that for CI chondrites. The amount of CAI material in CVs is twice as much as in CMs (Brearley and Jones, 1998). So, the CAI input into the Th/U whole rock variations has to be significant. To produce the CV-trend in Figure 4.1.1, CAI materials have to be mixed with a low-U component (matrix?).

The amount of Th and U data for CAIs of CV3 chondrites is not overwhelming. Whole rock CV3 and isotope dilution TIMS analyses of CAIs from Allende (CV3) meteorite are plotted in Figure 4.4.2. The only available analyses of the CAI and chondrules are ID TIMS from Tatsumoto et al. (1976) and Chen and Tilton (1975). CAI Th/U ratios range between 2.5 and 11, whereas chondrule data from Chen and Tilton (1975) are scattered in the area between CAI and whole rock analyses. From the data plotted in Figure 4.4.2 it is not obvious that mixtures of all the components should produce a linear correlation. A possible problem with the Chen and Tilton (1975) data is that these authors used HCl leaching of their samples as a cleaning procedure. Potentially, such leaching could remove microscopic carbonates and phosphates before analysis, producing disturbed actinide data. The HCl-leached CAIs and chondrules are filled symbols in Figure 4.4.2. Omitting those leached samples, mixture of the chondrule Th and U analyses average out closer to the whole rock data.

Figure 4.4.3 demonstrates one possible way to produce linear whole rock correlation in CV chondrites. As shown in Figure 4.4.3, mixture of a primitive (nebular) CI-like material ("A&G") and 5% of CAI component with variable Th/U will produce a whole rock trend seen in Figure 4.1.1. Uranium data for chondrules and, possibly, matrix are higher than primitive CI composition, which argues that these components were "contaminated" with CAIs. Unlike CM chondrites, phosphates are more commonly observed in CV chondrites. Our leaching experiments show that in CMs very little phosphorus is in phosphate phases, but Ebihara and Honda (1987) have found that ~60% of P in Allende (CV3) is associated with phosphates, so their role in the CV Th/U distribution can not be ruled out.

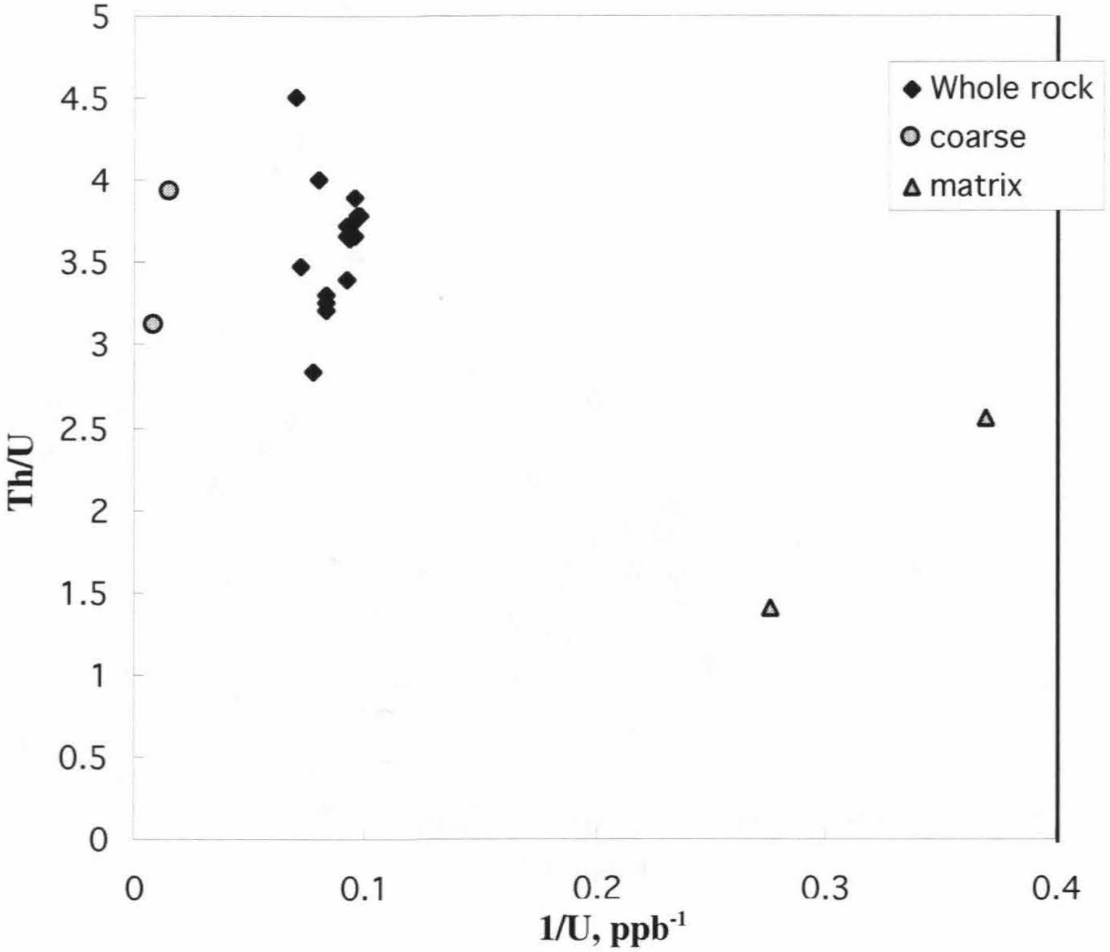

Figure 4.4.1 Combined literature and this study data for CM2 chondrites meteorite from Table 4.3.1. Matrix and coarse fractions as well as leaching experiments data are "total" analyses.

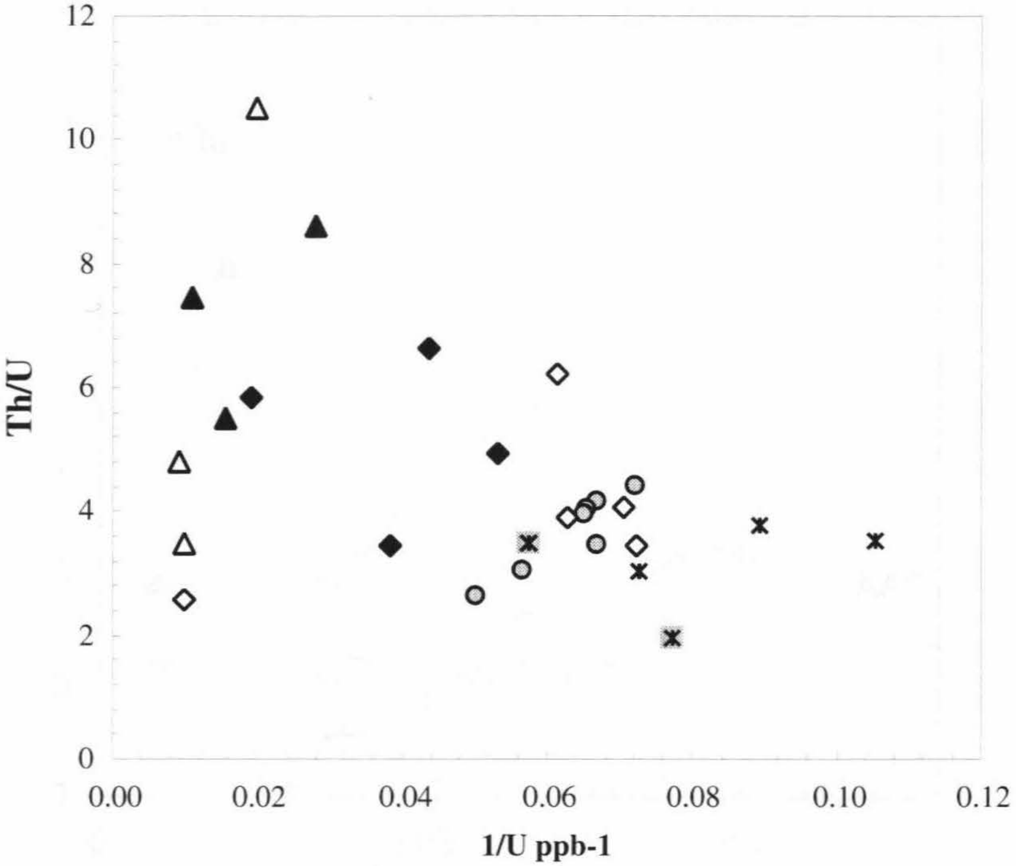

Figure 4.4.2 Whole rock (circles), CAI (triangles), chondrules (diamonds) and matrix (crosses) analyses in Allende (CV3) meteorite. Whole rock analyses same as in 4.1.1. Data from Tatsumoto et al. (1976) and Chen and Tilton, (1975). Filled labels are samples leached with HCl (see text for details).

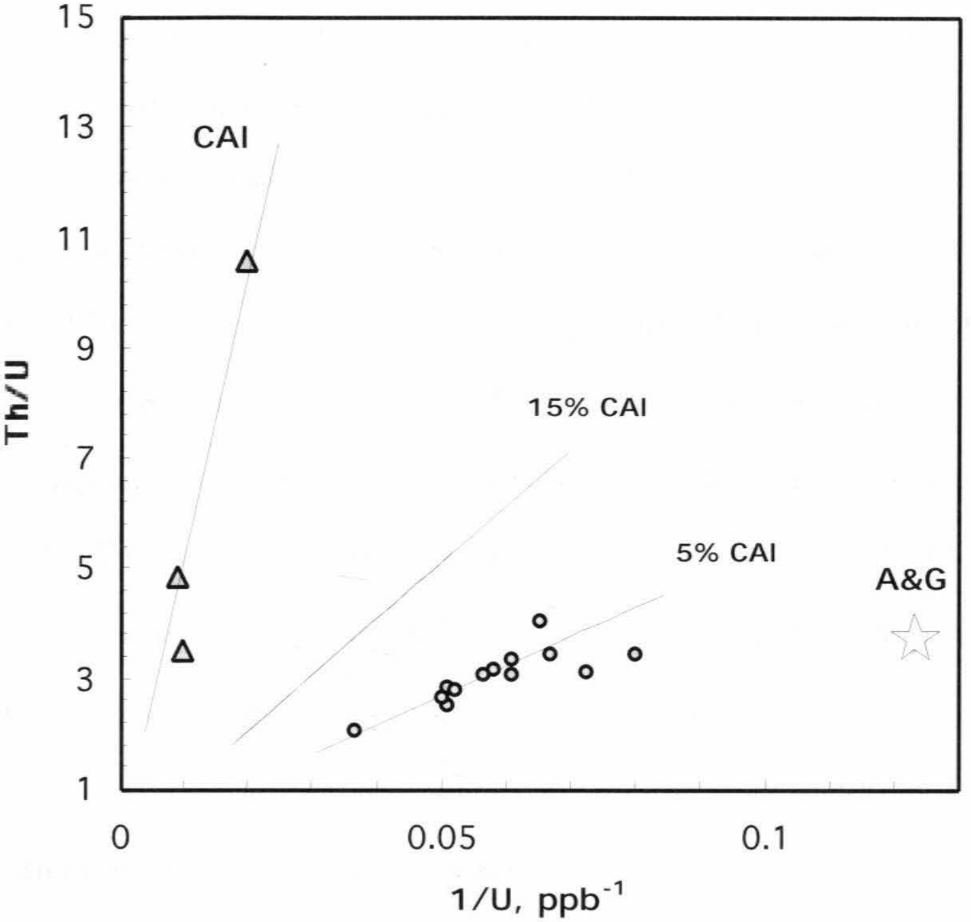

Figure 4.4.3 Illustration of the mixing of the primitive nebular material (A&G, Anders and Grevesse, 1989) with CAIs of variable Th/U (Tatsumoto et al. 1976) to produce whole rock CV3 variations. Whole rock data as in Figure 4.1.1. The line through the whole rock CV3 data is a calculated trend with 5% of CAI mixed with A&G component. For comparison, trend for 15% CAI admixture is also shown.

Chapter 5: Implications to cosmochronology

As it was briefly discussed in the Introduction, U and Th solar system abundances are especially valuable for determining the age of r-process nucleosynthesis.

Cosmochronological time is usually divided into three periods: 1) T, a period of active nucleosynthesis, during which the production of a nuclear species (P_i) occurs parallel to the free decay; 2) Δ, a free-decay period before the formation of the solar system, during which P_i=0, and 3) 4.6 Gyr of the solar system existence, from T+Δ until today, during which free decay occurs within solar system (e.g., Podosek and Swindle, 1988). Constraints on Δ come from short-lived isotopes, such as ^{244}Pu. We assume that $\Delta \ll \tau_{235}$ (where τ_{235} is the lifetime of ^{235}U, the shortest–living of nuclides considered), so that Δ=0 is a good approximation for for the models considered.

For every nuclear species with a decay constant λ_i, the abundance N_i at time T is defined as a solution of the growth equation:

$$N_i = \int_0^T P_i(t) e^{-\lambda_i (T-t)} dt \tag{1}$$

There are two unknowns in the equation above: production "history," or change in the production rate with time, and T. Instead of dealing with absolute abundances and absolute production rates, it is only possible to consider two ratios of two species, such as ^{235}U/^{238}U and ^{232}Th/^{238}U. Thus in general we have two equations with two unknowns, although P_i(t) can have several parameters.

There are various simple models of nucleosynthetic production histories (see Figure 5.1), such as (1) constant production rates until solar system matter is isolated from further nucleosynthetic input, (2) production exponentially decreasing with time (e.g., Fowler, 1977), and (3) initial rapid increase in production, followed by the smooth decrease (for example, Clayton 1988). These models have received substantial mathematical treatment (Schramm, 1973, Clayton, 1984, Fowler 1977, 1987, Clayton, 1987), and a number of galactic ages (T+4.6 Gyr) were determined, ranging from 8.7 to 12.8 billion years relative to the present.

All the models are limited by how precisely we know the two abundance ratios and two relative production rates of ^{235}U, ^{238}U and ^{232}Th. The solar uranium isotopic composition $^{235}U/^{238}U=1/137.88$ is precisely defined (e.g., Chen and Wasserburg, 1981). In this work we have improved the knowledge of the solar system $Th/U=3.53\pm0.1$ (weight ratio), which translates to $^{232}Th/^{238}U\approx3.64\pm0.1$ atomic ratio.

The relative production rates are known from a combination of the decay schemes and nuclear physics theoretical predictions. As was recognized by B^{2}FH, P_{232}/P_{238} and P_{235}/P_{238} are unique among nucleosynthetic production rates, being accurately determined simply by counting the alpha decay progenitors ending at masses 232 and 238 based on the well known decay properties of nuclei near the line of β-stability between A= 230-260. The uncertainties on relative production ratios come mostly from the consideration of β-delayed neutron emission. Although by astrophysical standards these uncertainties are small, for present purposes they are big. The quoted values for U, Th relative production rates vary by ~25%, and uncertanties on those values are up to 30%.

During the 1980s, it was proposed that, during the long chain of β-decays connecting the r-process path and the line of β-stability, spontaneous fission from nuclear excited states following beta decay ("beta-delayed fission") would significantly change the B^2FH progenitor production rate model. However, in the last 10 years, estimates of the importance of beta-delayed fission have steadily dropped (Meyer et al., 1989; Hall and Hoffman, 1992) to the point where it is acceptable to neglect this effect (D. Hoffman, private communication).

Table 5.1 lists literature production rate ratios of chronometer pairs (modified from Thielemann et al. 1993).

Hipparcos astrometry satellite observations have dramatically improved knowledge of our Galaxy. Interesting results come from the re-evaluating distances, hence ages of globular clusters. The globular clusters of the galactic halo are the oldest datable objects in our galaxy, thus setting a lower limit to the galactic age. Clusters as old as 15 billion years (e.g., globular cluster M92, Carretta et al., 2000) are observed.

Differing from the starting point of other researchers, we will accept the estimates of the minimum galactic age based on the globular clusters. So the age of the galaxy is not a parameter. On the other hand, we will permit maximum production to occur significantly more recent than 15 Gyr, corresponding to the slow infall into the galactic disk.

The uncertainties of the estimates of the relative production rates is the major limiting factor for all models. Consequently, our approach is to calculate the production rate ratios (P_i/P_j), defined by the galactic age, nuclide abundances, and time-dependence of the production rate evolution assumed in the model. Then the calculated production ratios can be compared to the estimates from Table 5.1.

Let us consider 3 relatively simple scenarios, illustrated in Figure 5.1, for the evolution of the galactic production rates.

1). In case of the uniform production (Figure 5.1 a), $P_i(t)$=constant, equation (1) becomes

$$N_i = P_i \tfrac{1}{\lambda_i}(1-e^{-\lambda_i T}) \tag{2}$$

Then, for every pair of nuclides i and j,

$$\frac{N_i}{N_j} = \frac{P_i}{P_j}\frac{\lambda_j}{\lambda_i} * \frac{(1-e^{-\lambda_i T})}{(1-e^{-\lambda_j T})} \tag{3}$$

For the galactic ages (T+4.6 Gyr) 13-15 Gyr, and Th/U_{today}=3.55-3.75, the calculated range of possible solutions of the equation (3) for relative production rates is illustrated in the Figure 5.2. It is evident that calculated production ratios for the given time interval T are systematically off the production estimates (circles in the Figure 5.2 are from Table 5.1). Only for the galactic ages as young as 13 Gyr, the production ratios calculated in this model overlap with the estimated theoretical values of P_{232}/P_{238} and higher than P_{235}/P_{238}. The height of the bar is determined by allowing today's solar system Th/U to vary between 3.55 and 3.75, witch is in the limits of 1σ uncertainty on our Th/U. For 2σ, the overlap will be greater, allowing 14 Gyr calculations to also overlap with the estimates. Most previous nucleocosmochronology models indicated galactic ages significantly lower. Indeed, according to Figure 5.2, lower ages are more compatible with estimates of the production rates, would be consistent with the beginning of the r-process production in the disk long after the formation of the halo globular clusters.

2). In case of exponential galactic synthesis (Figure 5.1.b), it is assumed that the rate of the star formation and the rate of nucleosynthesis are exponential functions of the time (Fowler, 1977). In this case for every nuclide i with λ_i decay constant and initial production P_{i0},

$$\frac{dN_i}{dt} = P_{i0}e^{-t/T} - \lambda_i N_i, \tag{4}$$

where T_r is the decay time constant in the rate of r-process nucleosynthesis.

From the equation (4) it follows that for every pair of nuclides i and j,

$$\frac{N_i}{N_j} = \left(\frac{P_i}{P_j}\right)_0 \frac{\lambda_j - 1/T_r}{\lambda_i - 1/T_r} * \frac{e^{-t/T_r} - e^{-t\lambda_i}}{e^{-t/T_r} - e^{-t\lambda_j}} \tag{5}$$

Figure 5.3 shows the field of possible solutions for ^{232}Th/^{238}U and ^{235}U/^{238}U production ratios from the equation (5), given the Th/U ratio today between 3.55 and 3.75 and age of the Galaxy between 13 and 15 Gyr. There is a full range of T_r from essentially zero to infinity. As follows from this plot, the field of existing solutions barely overlaps with estimated production ratios. It is possible to calculate possible T_r for the time interval and production rates, defined by the overlap of the solutions for equation (5) with the field of production rate estimates. This range corresponds to only 13 Gyr galactic age and T_r >35 Gyrs, which is approaching a uniform production (case of Figure 5.2).

3). Now let us consider a more general case, which includes the two scenarios above as special cases. We assume that initial exponential growth in the galactic production in the beginning of the galactic history is followed by an exponential decrease (Figure 5.1.c). This scenario allows for the delayed supernovae production in the disc relative to the globular cluster age. Thus we assume r-process production rate to be proportional to ($e^{-t/\tau 1}$-$e^{-t/\tau 2}$), where $\tau_1 > \tau_2$, starting with $P_i(0)=0$:

$$\frac{dN_i}{dt} = P_i(e^{-t/\tau_1} - e^{-t/\tau_2}) - \lambda_i N_i \tag{6}$$

Figure 5.1.c shows only a general shape of change in supernovae production. The position and amplitude of the peak in Figure 5.4 depends on values τ_1 and τ_2. The

parameter τ_1 is the decay constant for exponential decrease in the production rates (analog to T_r in the second model). The parameter τ_2 is a time constant defining infall from the halo to the disc.

From the equation (6) for the nuclide pair:

$$\frac{N_i}{N_j} = \frac{P_i}{P_j} * \frac{e^{-t/\tau_i}}{e^{-t/\tau_j}} * \frac{\left[\dfrac{e^{-\frac{t}{1/\tau_i - 1/\tau_1}} - 1}{1/\tau_i - 1/\tau_1} - \dfrac{e^{-\frac{t}{1/\tau_i - 1/\tau_2}} - 1}{1/\tau_i - 1/\tau_2}\right]}{\left[\dfrac{e^{-\frac{t}{1/\tau_j - 1/\tau_1}} - 1}{1/\tau_j - 1/\tau_1} - \dfrac{e^{-\frac{t}{1/\tau_j - 1/\tau_2}} - 1}{1/\tau_j - 1/\tau_2}\right]} \qquad (7)$$

where τ_I and τ_j and are mean lives of the two nuclides.

The parameters τ_1 and τ_2 can be calculated assuming 13-15 Gyr Galactic age and solar Th/U ratio 3.55-3.75. Figure 5.4 shows fields of possible solutions for relative production rates for 13, 14 and 15 Gyr galactic age. Although we cannot distinguish between the three fields, this model has a bigger overlap with estimated relative production rates than the previous ones. A semi-log plot of τ_2 vs. τ_1 in Figure 5.5 shows contours of P_{235}/P_{238} relative production rates calculated for 15 Gyr galactic age. The lower part of the plot (field of $\tau_2 > \tau_1$) is not allowed in the frame of this model. The shaded area, where $1.2<P_{235}/P_{238}<1.52$, is the field where solutions of equation (7) overlap with the field of estimated ratios.

Most solutions correspond to large τ_1, i.e., slow decay of the production rate. For a 15 Gyr galactic age, the fastest possible decay (≈8 Gyr decay time constant) corresponds to a very slow infall rates (≈7.5 Gyr time constant). Faster decays are possible with younger galactic ages. The dependence of minimum decay constants for 13 Gyr on the infall time constant and Th/U ratio is shown in Table 5.2.

To achieve a short infall time constant (τ_2 <0.5 Gyr), the decay constant must be very big (>100 Gyr), approaching uniform production. The dependence of the minimum infall time constants on the assumed ranges of Th/U ratios and the galactic ages is shown in Table 5.3. This table shows, that production starting earlier in the galactic hystory, the minimum infall times become progressively higher.

From the models considered for 15 Gyr galaxy, model 3 is the only one that is consistent with theoretically estimated actinide relative production rates. Thus, taking in account galactic infall, we can limit the range of time constants τ_1 and τ_2 for 15 Gyr galaxy. Time-dependence of the galactic production rates can be described as a case between nearly uniform production for extremely fast infall rates and moderately fast decay time with very slow infall (8 Gyr).

Table 5.1 Production ratios from r-process calculations.

^{232}Th/^{238}U	^{235}U/^{238}U	Reference	Notes
1.65	1.42	Seeger et al., 1965	
$1.74^{+0.3}_{-0.2}$	$1.46^{+0.4}_{-0.3}$	Schramm and Wasserburg, 1970	
1.9	1.89	Seeger and Schramm, 1970	
1.8±0.1	1.42±0.19	Fowler 1977	
1.9	1.5	Symbalisty and Schramm, 1981	
1.5	1.1	Krumlinde et al., 1981	
$1.9^{+0.2}_{-0.4}$	$1.5^{+0.5}_{-0.6}$	Schramm, 1982	
1.4	1.24	Thielemann et al., 1983	
1.71±0.07	1.34±0.19	Fowler, 1987	Same as Fowler, 1977, with ^{250}Cm-SF corrected
1.6	1.16	Cowan et al., 1987	With β-delayed fission
1.53	1.26	Thielemann et al., 1989	Without β-delayed fission
1.73	1.79	Thielemann et al., 1993	Equal abundances assumed

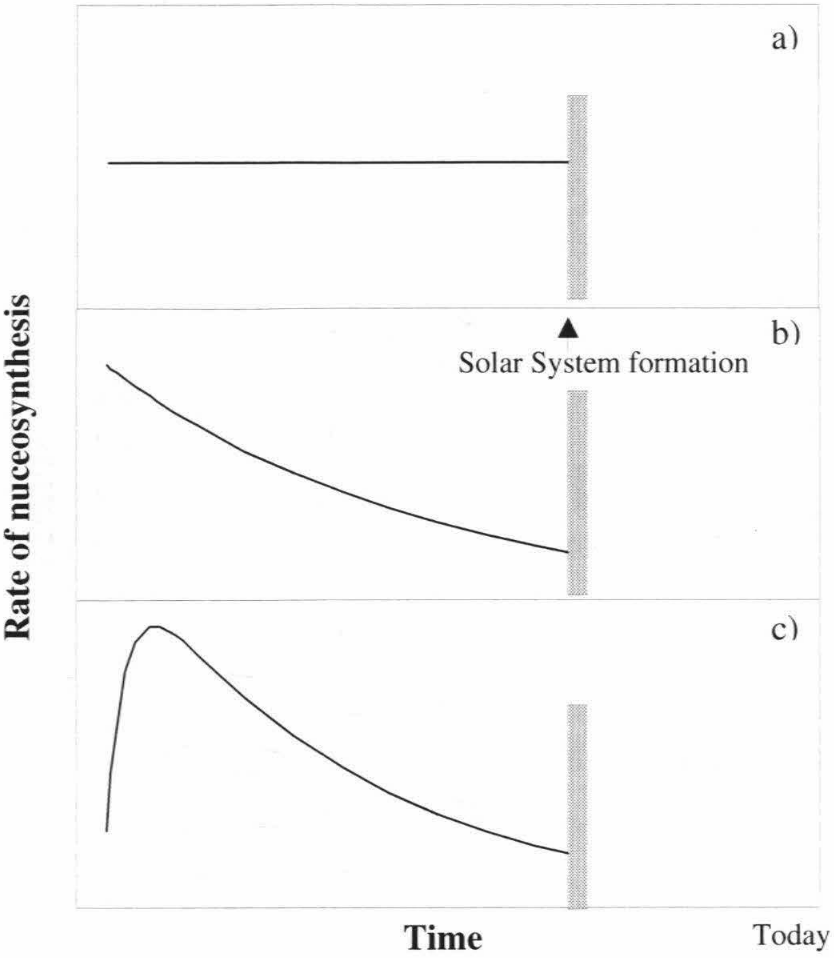

Figure 5.1 Examples of different models of nucleosynthetic production histories. a) constant production until the formation of the Solar System, b) exponential decrease in production, c) rising production in the beginning of the galactic history followed by exponential decrease.

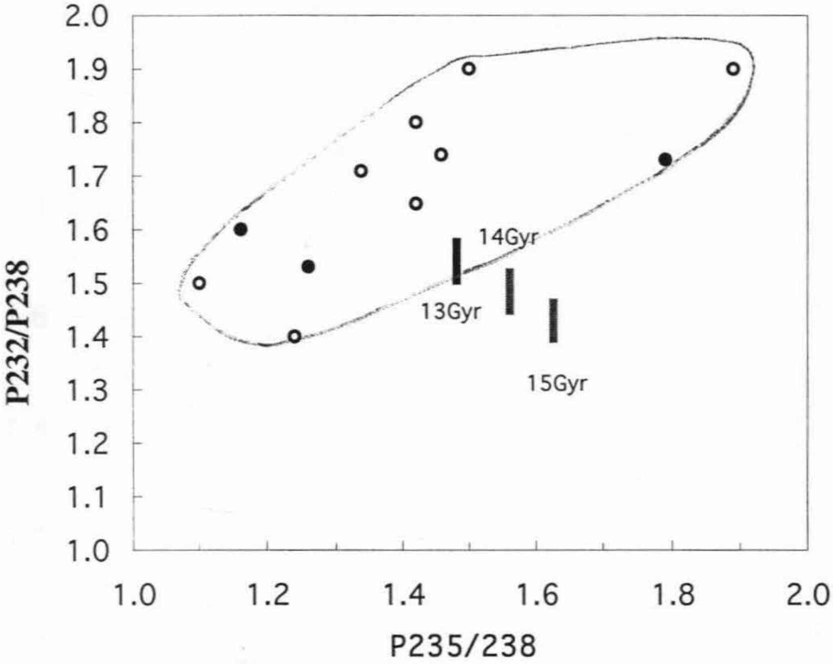

Figure 5.2 Solutions for the relative production rates for uniform production (equation 3) for the galactic ages from 13 to 15 Gyr. The height of the bar is determined by allowing today's solar system Th/U to vary between 3.55 and 3.75. Circles are production values from Table 5.1 for comparison (filled circles are three the most recent values).

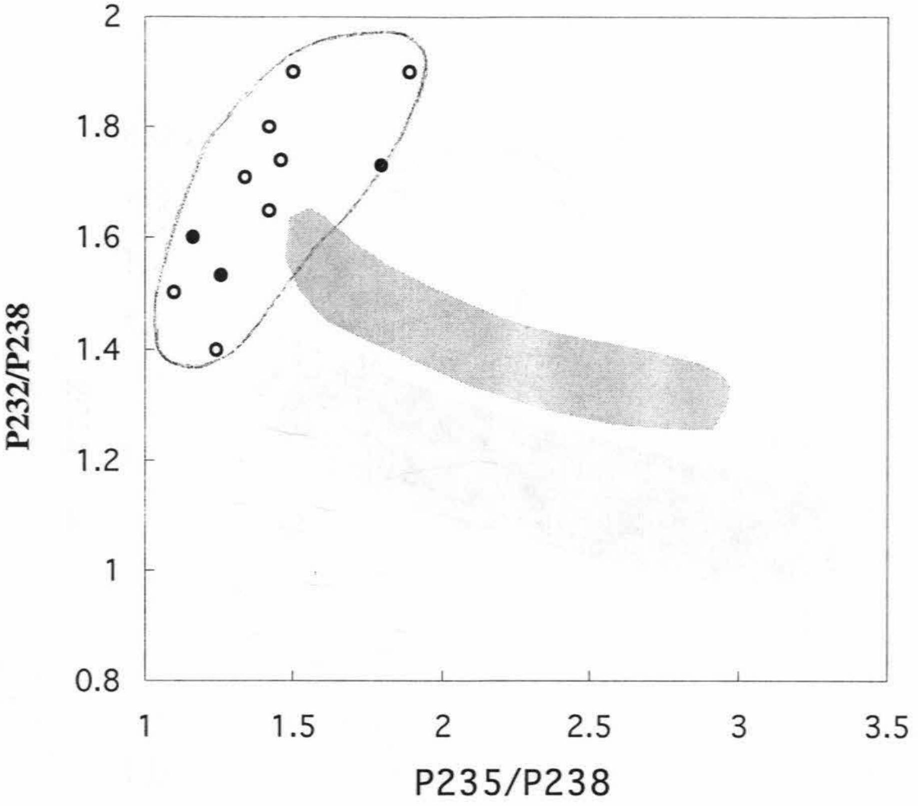

Figure 5.3 Calculated possible solutions for today's Th/U between 3.55 and 3.75 and age of the galaxy between 13 and 15 billion years. Circles are theoretical estimations of r-process production rates as in Figure 5.2. There is no overlap of two fields for an age >13 Gyr.

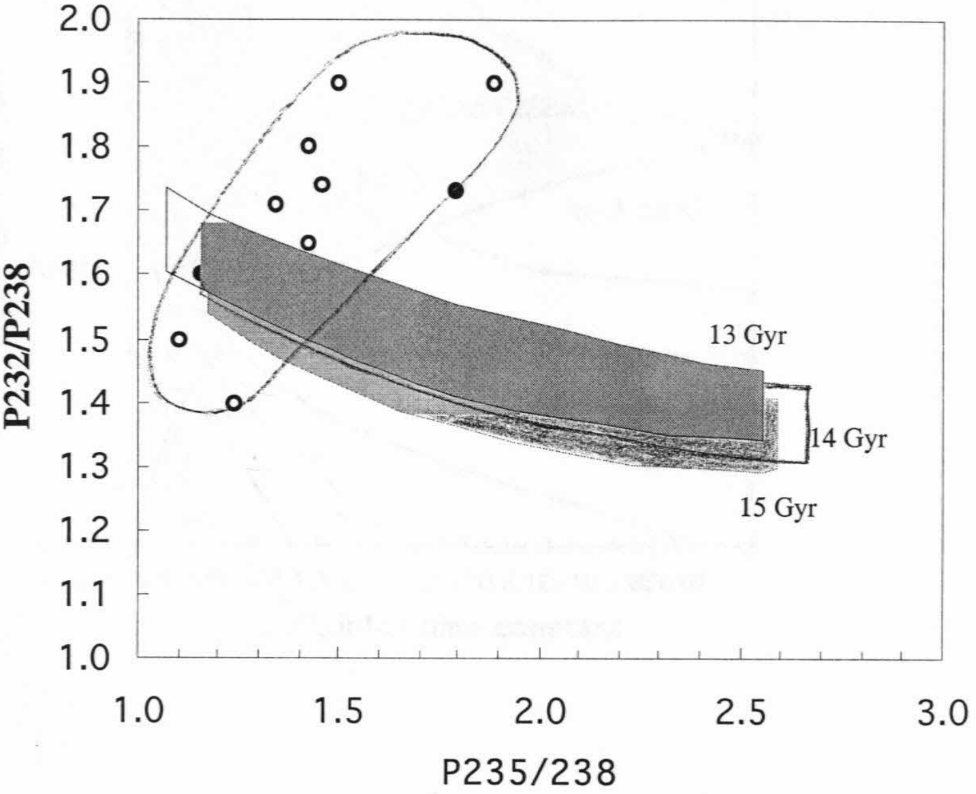

Figure 5.4 Calculated possible solutions for today's Th/U between 3.55 and 3.75 and age of the galaxy of 13, 14 and 15 billion years (equation 7).

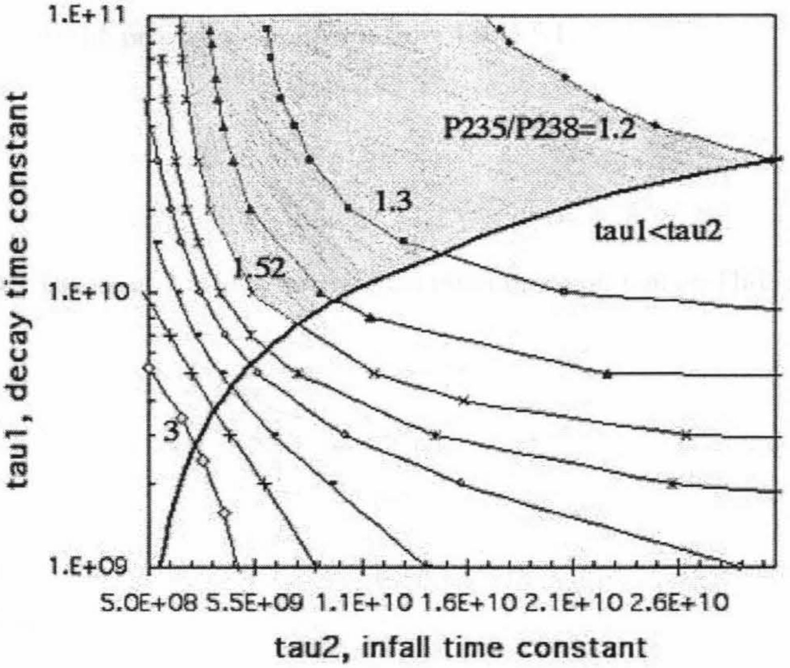

Figure 5.5 Calculated parameters τ_1 and τ_2 from equation (7) for different $^{235}U/^{238}U$ supernovae production rates and 15 Gyr galactic age. Shadowed area is the field of overlapping solution with area of theoretical estimations of the production rates (see Figure 5.4).

Table 5.2 The minimum decay time constant for 13 Gyr galactic age as a function of τ_2 and Th/U.

	Th/U today		
τ_2, Gyr	3.49	3.62	3.75
5	5	5	5
3	6.5	5.3	4.6
1	35	17	13
0.5	80	30	20
0.2	x[1]	x[1]	31

[1] no overlap with production estimates from Table 5.1.

Table 5.3 The dependence of the minimal infall time constant on Th/U and the galactic age.

	Th/U today		
T, Gyr	3.49	3.62	3.75
13	0.7	0.4	0
14	1.4	1	0.4
15	2.6	1.8	1.5
16	4.4	3.5	2.5
17	7	4.5	4.3

Summary

Non-volatile elements in CI chondrites are considered to have average solar system abundances. However, literature data show big variations in Th/U. Ordinary chondrites have refractory element abundances identical to CI chondrites; therefore, we should be able to rely on ordinary chondrites for estimation of a more precise solar Th/U ratio. Whole rock Th, U analyses prior to our work showed a bimodal distribution in ordinary chondrites, with some meteorites showing an anomalously high Th/U of 6. One of those meteorites, Harleton, was the key for the current study.

Isotope dilution thorium and uranium analyses by inductively-coupled plasma mass spectrometry of 12 samples of Harleton (L6) show a much larger scatter than was previously observed in equilibrated ordinary chondrites. The bimodal distribution of the older data was only apparent. Th/U linearly correlates with 1/U in Harleton and in the total equilibrated ordinary chondrite data set as well. Such a correlation suggests a two component mixture and this trend can be quantitatively modeled as reflecting variations in the mixing ratio between two phosphate phases: chlorapatite and merrillite. The major effect is due to apatite variations, which strongly control the whole rock U concentrations. Phosphorous variations will tend to destroy the Th/U vs. 1/U correlation, and measured P concentrations on exactly the same samples as U and Th show a factor of 3 range. It appears that the P variations are compensated by inverse variations in U (a dilution effect) to preserve the Th/U vs. 1/U correlation.

In ordinary chondrites, data on actinide, P, and Cl chemistry are consistent with contemporary views on the origin and evolution of these materials. The parent material of ordinary chondrites resulting from nebular processes had Th and U primarily concentrated in chondrule glass with P present in metal (possibly sulfide) phases, the latter a consequence of condensation or at least high temperature nebular phase equilibrium. The chlorine host phases are unknown, but apparently very heterogeneously distributed. Very early after the accumulation of parent bodies, more oxidizing conditions resulted in phosphate nucleation, preferentially as binary grains with metal or sulfide (Jones and Burnett, 1979). The relatively large chondritic P/Cl ratio compared to apatite stoichiometry and the heterogeneous Cl distribution resulted in a relatively homogeneous distribution of merrillite and a very heterogeneous distribution of apatite. During the later stages of ordinary chondrite metamorphism, following crystallization and recrystallization of chondrule glass, the actinides redistributed themselves into the phosphate phases with gm-scale heterogeneities impressed on bulk actinide (especially U) concentrations. The unequal distribution of Th and U among the two phosphates is probably a consequence of equilibrium partitioning. Thus, except for an inability of apatite grains to coarsen during metamorphism, equilibrated chondrites possibly can be regarded as truly equilibrated from the point of view of actinide chemistry.

Because variations in whole rock Th/U are consequences of phosphate sampling, a weighted average of high accuracy Th/U measurements in equilibrated ordinary chondrites should converge to a significantly improved average solar system Th/U. Based on the combination of our and literature isotope dilution data, we calculate a solar system Th/U value of 3.53 (by weight), with $1\sigma_{mean}=0.10$, which is significantly lower and more precisely defined than previous estimates.

If this number is indeed an average solar system value, it brings up an issue of a significantly higher Th/U ratios of the Earth (~3.9, see Chapter 1.1). Such difference can be attributed to U, behaving more as moderately volatile element, rather than refractory lithophile. Interestingly, in this case, the *true* average solar system Th/U must be even lower than our estimate of the ordinary chondrite ratio. An other possibility is that the Earth reservoir was more contaminated with the high Th/U refractory material than ordinary chondrites.

Analogous to ordinary chondrites, an apparent two-component correlation of Th/U vs. 1/U in carbonaceous chondrites was previously suggested by Rocholl and Jochum (1993). To explore the possibility of apatite producing Th/U variations in CI and CM chondrites, we performed P analyses on the solutions from previous CI leaching experiments from Chen et al. (1993) and our own leaching experiments in CM-type carbonaceous chondrites.

Th/U variations in Orgueil (CI) can be explained by the redistribution of actinides (mostly U) by the aqueous fluid into secondary mineral phases, such as carbonates and sulfates. Our data show that the mobile phase is not a phosphate, contrary to the interpretations of Rocholl and Jochum. The redistribution of alteration products, rich in uranium, but not thorium, can produce a real 2-component mixing line for the whole rock CI analyses. To become mobile, uranium has to be partially oxidized to higher valence states.

Unlike CI and OC whole rock analyses, Th/U variations in CM chondrites are mostly due to Th variations. The Th/U vs. 1/U correlation is an artifact of the older data.

There are at least 4 components in CM chondrites responsible for the Th/U variations we see in the whole rock analyses.

First, fine matrix material in Murchison contains U-rich carbonate/sulfate phases (analogous to Orgueil), but the total amount of matrix U is not significant on a total rock basis. Matrices in carbonaceous chondrites are often regarded as primitive. Our study of the Murchison (CM2) matrix showed that it is P and actinide-depleted. Second, CAI and chondrules are major reservoirs for actinides, which is consistent with contemporary views on the origin and evolution of these materials. Finally, our data show an easily leachable phase of high Th/U, likely carbonates produced by alteration of CAIs as with Cis. Phosphates play only a minor role as actinide carrier phases in CM chondrites.

Establishing a more precise solar system Th/U allowed us to re-visit nucleocosmochonology models, but starting from a point different from other researchers. We accept the estimates of the minimum galactic age based on the halo globular clusters and calculate the required relative supernovae production rates for ^{232}Th/^{238}U and ^{235}U/^{238}U, assuming different models for the time dependence of r-process nucleosynthesis. The required production rates can be compared with independent nuclear physics estimates. We considered three simple models of the galactic supernovae production: (1) constant production over the galactic history untill solar was formed; (2) production exponentially decreasing with time, and (3) initial rapid increase in production (infall), followed by the exponential decrease. The calculated production rates for the first two models are compatible with part of the range of estimated values for the galactic age <13 Gyr. The older galaxy requires time-dependence of the galactic production rates to be a case between nearly uniform production for extremely fast infall rates and moderately fast decay time with very slow infall (8 Gyr).

References

Allegre C.J., Dupre B. and Lewin E. (1986) Thorium/Uranium ratio of the Earth. *Chem Geol.,* 56, 219-227.

Anders E. and Ebihara M. (1982) Solar-system abundances of the elements *Geochim. Cosmochim. Acta*, 46, 11, 2362-2380.

Anders E. and Grevesse N. (1989) Abundances of elements: meteoritic and solar. *Geochim. Cosmochim. Acta,* 53, 197-214.

Asmerom Y. (1999) Th-U fractionation and mantle structure. *Earth Planet. Sci. Lett.* 166, 163-175.

Boynton W.V. (1978) Fractionation in the solar nebula, II. Condensation of Th, U, Pu and Cm. *Earth Planet. Sci. Lett.* 40, 63-70.

Brearley A.J. and Jones, H.J. (1998) Chondritic meteorites, in *Planetary Materials* (ed. J.J.Papike), Reviews in Mineralogy Series, MSA, Washington, DC, 3-01 - 3-398.

Bunch T.E., Chang S., Frick U., Neil J. and Moreland G. (1979) Carbonaceous chondrites - I. Caracterization and significance of carbonaceous chondrite (CM) xenoliths in the Jodzie howardite. *Geochim. Cosmochim. Acta,* 43, 1727-1742.

Burbidge E.M., Burbidge G.R., Fowler W.A. and Hoyle F. (1957) *Rev. Mod. Phys.* 29, 547.

Burnett D.S., Stapanian M.I. and Jones J.H. (1982) Meteorite actinide chemistry and cosmochronology. In *Essays in Nuclear Astrophysics* (eds. C.A. Barnes, D.D. Clayton and D.N. Schramm), pp. 141-158. Cambridge University Press.

Carretta E., Gratton R.G., Clementini G., et al. (2000) Distances, ages, and epoch of formation of globular clusters. *Astrophys J.* 533, 215-235.

Carretta E., Gratton R.G., Clementini G., and Pecci F.F. (2000) Distances, ages, and epoch of formation of globular clusters *Astroph. Jour.,* 533, 215-235.

Chen J.H. and Tilton, G.R. (1975) Isotopic lead investigations on the Allende carbonaceous chondrite. *Geochim. Cosmochim. Acta,* 40, 635-643.

Chen J.H. and Wasserburg G.J. (1981) Isotopic determination of Uranium in picomole and subpicomole quantities. *Analit. Chem.* 53, 2060-2067.

Chen J.H. and Wasserburg G.J. (1985) Peculiar U-Th-Pb systematics in Shergotty: A Martian lead? (abstract). *Proc. Lunar Planet. Sci.*, 16, 7-8.

Chen J.H., Wasserburg G.J. and Papanastassiou D.A. (1993) Th and U abundances in chondritic meteorites (abstract). *Lunar Planet. Sci.,* 24, 277-278.

Clarke, Roy S., Jr. and Henderson, E.P. (1974-75) The Harleton, Texas, Chondrite. *Smithsonian contributions to the Earth Sciences*, 19, 61-70.

Clayton R.N. and Mayeda T(1989) Oxygen isorope classification of carbonaceous chondrites (abstr,) *Lunar Planet. Sci.,* 67, 151-161.

Collerson K.D. and Kamber B.S. (1999) Evolution of the continents and the athmosphere inferred from Th-U-Nb systematics of the depleted mantle. *Science* , 283, 1519-1522.

Crozaz G. (1974) U, Th and extinct 244Pu in the phosphates of the St. Severin meteorite. *Earth Planet. Sci. Lett.,* 23, 164-169.

Crozaz G. (1979) Uranium and thorium microdistributions in stony meteorites. *Geochim. Cosmochim. Acta,* 43, 127-136.

Crozaz G., Pellas P., Bourot-Denise M., de Chazal S.M., Fieni C., Lundberg L.L. and Zinner E. (1989) Plutonium, uranium and rare earths in the phosphates of ordinary chondrites; the quest for a chronometer. *Earth Planet. Sci. Lett.* 93(2), 157-169.

Devouard B. and Busek P.R. (1997) Phosphorus-rich iron, nikel sulfides in CM2 chondrites: condensation or alteration products (abstr) *Met. Planet. Sci.* 32, A34.

Ebihara M. and Honda M. (1984) Distribution of rare earth elements and uranium in various components of ordinary chondrites. *Meteoritics*, 19(2), 69-77.

Ebihara M. and Honda M. (1987) Rare earth elements in Ca-phosphates of Allende carbonaceous chondrite. *Meteoritics*, 22(3), 179-190.

Endress M. and Bischoff A. (1996) Carbonates in CI chondrites: clues to parent body evolution *Geochim. Cosmochim. Acta,* 60, 489-507.

Fowler W.A. (1977) Nuclear cosmochronology. In *The R.A. Welch Found. Conf. on Chem. Research XXI. Cosmochemistry*, pp. 61-133, Houston, Texas.

Fowler W.A. (1987) The age of the observable universe. *Q. Jl R. Astr. Soc.* 28, 87-108.

Grossman L. and Olsen E. (1974) Origin of the high temperature fraction of C-2 chondrites. *Geochim. Cosmochim. Acta,* 38, 1119-1140.

Grossman J.N., Rubin A.E., Nagahara H. and King E.A.(1988) Properties of chondrules. In *Meteorites and the early solar system* (eds. J. F. e. Kerridge and M. S. e. Matthews), 619-659. The University of Arizona Press, Tucson.

Hagee B., Bernatowicz T.J., Podosek F.A., Johnson M.L., Burnett D.S. and Tatsumoto M. (1990) Actinide abundances in ordinary chondrites. *Geochim. Cosmochim. Acta,* 54, 2847-2858.

Ireland T.R., Compston W., Williams I.S. and Wendt I. (1990) U-Th-Pb systematics of individual perocskite grains from the Allende and Murchison carbonaceous chondrites. *Earth Planet. Sci. Lett.* 101, 379-387.

Irion R. (2000) A crushing end for our Galaxy. *Science*, 287, 62-64.

Jarosewich, E. and Dodd, R.T. (1985) Chemical variations among L-chondrites; IV, Analyses, with petrographic notes, of 13 L-group and 3LL-group chondrites. *Meteoritics*, 20, 1, 23-36.

Jarvis, K.E. (1997) Inductively coupled -plasma-mass spectrometry. In *Modern Analytical Geochemistry* (ed. R. Gill), pp.171-187. Longman, Singapore.

Jones J.H. and Burnett D.S. (1979) The distribution of U and Pu in the St. Severin chondrite. *Geochim. et Cosmochim Acta,* 43, 1895-1905.

Jones J.H., Burnett D.S., Criswell P.R. and Merrill R.B. (1980) Laboratory studies of actinide metal-silicate fractionation. Meteorite and regolith studies (abstract). *Lunar Planet. Sci.,*11, pp. 995-1001.

Kallemeyn and Wasson (1981, 1982, 1986) reference in Larimer J.W. and Wason J.T. (1988).

Keppler H. and Wyllie P.J. (1990) Role of fluids in transport of uranium and thorium in magmatic processes. *Nature*, 348, 531-533.

Kornacki A.S. and Fegley B. Jr (1986) The abundance and relative volatility of refractory trace elements in Allende Ca,Al-rich inclusions; implications for chemical and physical processes in the solar nebula. *Earth Planet. Sci. Lett.* vol.79, 217-234.

Korotev R.L. (1998) Concentrations of radioactive elements in lunar materials. *J. Geophl. Res.* 103 (E1), 1691-1701.

Kraus K..A. and Nelson F. (1958) Metal separations by anion exchange. *Am. Soc. for Testing and Materials Spec. Publ.,* 195, 27-57.

Larimer J.W. and Wasson J.T. (1988) Refractory lithophile elements. In *Meteorites and the early solar system* (eds. J. F. e. Kerridge and M. S. e. Matthews), pp. 394-415. The University of Arizona Press, Tucson.

Lodders K. and Fegley B. Jr. (1993) Lantanide and actinide chemistry at high C/O ratios in the solar nebula. *Earth Planet. Sci. Lett.* 117, 125-145.

Mackinnon I.D.R., Kaser S.A. (1990) Trace phases in CI chondrites Alais and Orgueil. *Proceedings of the abstracts of the 53rd meeting of the Meteoritical Society* 25(4), 381-382.

MacPherson G.J. and Davis A.M. (1994) Refractory inclusions in the prototypical CM chondrite, Mighei. *Geochim. et Cosmochim Acta,* 58, 5599-5625.

Manhes G., Allegre C.J., Dupre B. and Hamelin B. (1979) Lead-Lead Systematics, the "Age of The Earth" and the chemical evolution of our planet in a new representation space. *Earth Planet. Sci. Lett.* 44, 91-104.

Moore, C.B. (1971) Phosphorus. In *Handbook of elemental abundances in meteorites*. (B. Mason ed.) Gordon and Breach Science Publishers. p. 555.

Muller W.F., Kurat G. and Kracher A. (1979) Chemical and crystallographic study of cronstedtite in the matrix of the Cochabamba (CM2) carbonaceous chondrite. *Tschermaks Min. Petr. Mitt*. 26, 293-304.

Murrell M.T. and Burnett D.S. (1983) The behavior of actinides, phosphorus, and rare earth elements during chondrite metamorphism. *Geochim. Cosmochim. Acta,* 47, 1999-2014.

Nazarov M.A., Brandstatter F. and Kurat G. (1997) Comparative chemistry of P-rich phases in CM chondrites (abstract) *LPSCXXVIII*, 1003-1004.

Palme H., Larimer J.W. and Lipschutz M.E. (1988) Moderately volatile elements. In *Meteorites and The Early Solar System* (eds Kerridge F. and Matthews M.S.) pp. 436-461. University of Arizona Press, Tucson.

Pellas P. and Storzer D. (1975) Uranium and plutonium in chondritic phosphates. *Meteoritics* 10, 471-473.

Podosek F.A. and Swindle T.D. (1988) Nucleocosmochronology. In *Meteorites and the Early Solar System* (eds. J. F. Kerridge and M. S. Matthew), pp. 1114-1126. University of Arizona Press, Tucson.

Reed G.W. (1971) Chlorine. In *Handbook of elemental abundances in meteorites.* (ed. B. Mason), pp. 143-148. Gordon and Breach Science Publishers.

Rocholl A. and Jochum K.P. (1993) Th, U and other trace elements in carbonaceous chondrites: Implications for the terrestrial and solar-system Th/U ratios. *Earth Planet. Sci. Lett.* 117, 265-278.

Ruzicka A., Killgore M., Boesenberg J. and M. Prinz (2000) Portales Valley: not just another "ordinary" chondrite (abstract). *Meteoritics*, 35 supplement, A139-A140.

Schramm D.N. (1982) The r-process and the nucleochosmochronology. In Essays in Nuclear Astrophysics, eds. Barnes C.A., Clayton, D.D. and Schramm D.N., Cambridge Univ. Press, 325-353.

Schramm D.N. and Wasserburg G.J. (1970) Nucleocosmochronologies and the mean age of the elements. *Astrph. J.* 162, 57-69.

Seeger P.A., Fowler W.A. and Clayton D.D. (1965) reference in Thielmann et al. (1993)

Shinotsuka K. and Ebihara M. (1997) Precise determination of rare earth elements, thorium and uranium in chondritic meteorites by inductively coupled plasma mass spectrometry - a comparative study with radiochemical neuron activation analysis. *Analytica Chimica Acta,* 338, 237-246.

Shinotsuka K., Hidaka H. and Ebihara M. (1995) Detailed abundances of rare earth elements, thorium and uranium in chondritic meteorites: An ICP-MS study. *Meteoritics* 30, 694-699.

Sipiera P.P., Tarter J., Moore C.B., Dodd B.D. and Johnson R.A. (1980) Gomez, Terry County, Texas: a new meteorite find. *Meteoritics*, 15(3), 201-210.

Stacey J.S. and Kramers J.D. (1975) Approximation of terrestrial lead isotope evolution by two-stage model. *Earth Planet. Sci. Lett.* 26, 207-221.

Tatsumoto M. (1966) Genetic Relations of Oceanic Basalts as Indicated by Lead Isotopes. *Science* 153, 1094-1101.

Tatsumoto M., Knight R.J. and Allegre C.J. (1973) Time differences in the formation of meteorites as determined from the ratio of lead-207 to lead-206. *Science*, 180, 1279-1283.

Tatsumoto M., Unruh D.M. and Desborough, G.A. (1976) U-Th-Pb and Rb-Sr systematics of Allende and U-Th-Pb systematics of Orgueil. *Geochim. Cosmochim. Acta*, 40, 617-634.

Thielemann F.-K., Bitouzet J.P., Kratz K.-L., Cowan J.J. and Truran J.W. (1993) Operation of the r-process and cosmochronology. *Phys. Rep.* 227, 269-281.

Unruh D.M. (1982) The U-Th-Pb age of equilibrated L chondrites and a solution to the excess radiogenic Pb problem in chondrites. *Earth Planet. Sci. Lett.* 58, 75-94.

Von Michaelis H., Ahrens L.H. and Willis J.P. (1969) The composition of stony meteorites II. The analytical data and an assessment of their quality. *Earth Planet. Sci. Lett.* 5, 387-394.

Yabuki H. and El Goresy A. (1986) Phosphate-bearing microspherules in chondrules of unequilibrated ordinary chondrites. Yanai, Keizo, Takeda, Hiroshi and Shimoyama, Akira (editors), Proceedings of the Tenth symposium on Antarctic meteorites, *Memoirs of National Institute of Polar Research*. Special Issue, 41, p. 235-242.

Zolensky M.E., Bodnar R.J., Gibson E.K. Jr., Nyquist L.E., Reese Y., Shih, Chi-Yu, Wiesmann H. (1999) Asteroidal water within fluid inclusion-bearing halite in an H5 chondrite, Monahans. *Science,* 285, 1377-137.

Appendix I. Fibrous nanoinclusions in massive rose quartz. Part I: The origin of rose coloration.

This is a manuscript in press, to be published in the *American Mineralogist*, April 2001.

Fibrous nanoinclusions in massive rose quartz.

Part I: The origin of rose coloration.

Julia S. Goreva, Chi Ma and George R. Rossman
Division of Geological and Planetary Sciences,
California Institute of Technology, MS 100-23, Pasadena, CA, 91125

ABSTRACT

Pink nanofibers were extracted from rose quartz from 29 different pegmatitic and massive vein localities throughout the world. Their width varied from 0.1 to 0.5 _m. On the basis of optical absorption spectra of the fibers and the initial rose quartz, we conclude that these nanofibrous inclusions are the cause of coloration of massive rose quartz worldwide. These fibers do not occur in the rare, euhedral variety of pink quartz. Redox and heating experiments showed that the pink color of the fibers is due to Fe-Ti intervalence charge transfer that produces an optical absorption band at 500 nm. Based on the XRD patterns and characteristics of pleochroism, the best match for these inclusions is dumortierite. FTIR and Raman spectra consistently did not exactly match the standard dumortierite patterns, suggesting that this fibrous nano-phase may not be dumortierite itself, but rather a closely related material.

INTRODUCTION

The rose variety of quartz is known and valued from time immemorial as an item of beauty, a source of rock for decorative carvings and as a jewelry stone. Even though it is one of the less common colored varieties of quartz, rose quartz is found at numerous localities around the world.

Massive rose quartz occurs most commonly in granitic pegmatites and sometimes in massive hydrothermal veins. It makes up the whole or part of the core and/or joins together the potassium feldspars of the blocky zones of pegmatites (Cassedanne and Roditi 1991). Associated minerals are schorl, cassiterite, beryl, and phosphate minerals. Coloration of massive rose quartz varies from bright to pale pink, sometimes with lavender or orange overtones. It is always slightly- to highly turbid.

In spite of extensive studies over the last century, the source of the rose coloration in quartz still remains a subject of active debate. A number of possible mechanisms for the color of rose quartz have been proposed (reviewed in Rossman, 1994), but no consensus has developed. The proposed causes of pink color in quartz can be divided into 3 groups: (1) the presence of individual substitutional/interstitial ions in the quartz structure; (2) charge transfer between pairs various transition elements in the quartz structure; (3) the presence of mineral inclusions.

Based on chemical analyses, Holden (1924ab) argued that rose color in quartz is due to Mn^{3+} pigmentation. On the other hand, number of researchers later attributed the color to the presence of Ti^{3+} (Wright et al. 1963; Lehmann 1969; Cohen and Makar 1984). Other workers have suggested that the color of rose quartz is due to intervalence charge transfer (IVCT) between $Fe^{2+} + Ti^{4+} \rightarrow Fe^{3+} + Ti^{3+}$ (Smith et al. 1978) or between substitutional Ti^{4+} and interstitial Ti^{3+} (Cohen and Makar 1985).

Turbidity and scattering of light in massive rose quartz suggests the presence of a second mineral phase. Fine, submicrometer diameter oriented needles were observed and identified as rutile by many workers (e.g. Holden 1924a; Gordon 1945; Wright et al. 1963; Lehmann 1969). Vultee (1955) and Vultee and Lietz (1956) argued that scattering of light by rutile is, in fact, the real cause of the rose color. Later work by Dennen and Puckett (1971) supported this argument and concluded that the color of rose quartz results from

Tyndall scattering by tiny oriented rutile needles. Other pink phases such as tourmaline and manganiferous clays have been identified as inclusions in pegmatitic quartz, but their relationship to common, massive rose quartz has not been explored.

More recent studies presented different inclusions in rose quartz as an alternative to rutile. By HF etching of metaquartzite, Folk (1989) noticed fibrous resistant inclusions in quartz, which he presumed to be aluminosilicates. Applin and Hicks (1987) found that pink microfibers included in massive rose quartz from Montana and South Dakota yielded an X-ray diffraction pattern compatible with that of dumortierite, $Si_3B[Al_{6.75}[]_{0.25}O_{17.25}(OH)_{0.75}]$ (Moore and Araki 1978). Ignatov et al. (1990) observed macroscopic (2-3 mm) as well as submicron size inclusions in a rose quartz specimen from a vein in a biotite-muscovite schist from the Caucasus Mountains. Fine inclusions were oriented perpendicular to the c-axis of the quartz crystal. Clusters of larger prismatic needles were identified as dumortierite. The authors extrapolate their phase identification to the submicron size inclusions and conclude that these two types of inclusions (oriented and clustered) represent two generations of the same mineral, dumortierite. Optical absorption spectra, taken from a ~2 mm cluster, are similar to the optical spectra of the rose quartz itself. This study and the work of Applin and Hicks (1987) motivated us to raise the question of a more global role of dumortierite or other mineral inclusions in rose quartz coloration.

A further complication comes from reports about the lack of photo- and thermo-stability of rose quartz. Cassedanne and Roditi (1991) report, that in some Brazilian deposits, specimens on the surfaces of mine dumps turned milky white over a few years. Fading is often a characteristic of color centers from radiation damage. In other deposits, fragments dumped more than 50 years ago do not show any fading. There are reports that massive rose quartz is unstable under heat. Experiments by Ignatov et al. (1990) showed, that the color of rose quartz is lost at ~500°C. At this temperature, the larger, clustered inclusions in the quartz lost their color but did not change to another phase.

Although normally found in massive aggregates, rose quartz also occurs in a few pegmatites as euhedral crystals. Based on their optical properties and chemical composition, the coloration of these two types of rose quartz appears to be of a different nature. Massive quartz is slightly- to highly turbid, indicating the presence of the second phase, whereas single-crystal rose quartz (sometimes called pink quartz) is nearly devoid of internal scattering when probed by a narrow laser beam. In addition, single-crystal rose quartz is photochemically unstable, and, unlike massive rose quartz, it is extremely rare.

EPR spectra of natural euhedral rose quartz showed that this type of rose quartz contains hole centers induced by ionizing radiation. Maschmeyer and Lehmann (1983) have attributed rose quartz color to these centers. Their model consists of substitutional Al and P atoms bridged by O^- ions. This is further substantiated by Balitsky et al. (1996) who synthesized single-crystal rose quartz that contains these types of centers. The $Al\text{-}O^-\text{-}P$ centers are responsible for the photochemical instability. EPR studies of some synthetic euhedral rose quartz also revealed $[SiO_4/Li]^0$ centers (Bailey and Well, 1991) and $[TiO_4]^-$.

In this work we concentrate only on common massive rose quartz. By extraction of inclusions from pegmatitic and hydrothermal vein rose quartz from different localities, we explored whether there is a general relation between the presence of nanofibers and the origin of color in rose quartz. We tried to understand whether massive rose quartz commonly contains fibrous inclusions, whether nanofibers are the reason for its coloration, and what mineral phases make up those nanofibers.

MATERIALS AND METHODS

Sample preparation

The massive rose quartz samples selected for analysis (Table 1) exhibit small differences in tones and intensity of coloration. They all scattered light when probed with a narrow laser beam by, presumably, a second phase. For comparison, a sample of single-crystal pink quartz (GRR-1790a) with no turbidity, and a sample of dumortierite from

Dehesa, CA (GRR 122), were also analyzed. The quartz and dumortierite were crushed to a grain size of 1-5 mm, cleaned successively in methanol, near-saturated oxalic acid, 2N HCl and water. After cleaning, samples were left over night in an oven at 90°C to dry. The visual intensity of the coloration did not change during sample preparation and heating. The quartz samples were then dissolved in hot (100°C) concentrated (48%) HF. All 29 massive quartz samples produced insoluble fibrous residues (between 50 and 150 ppm of initial sample weight), with a color visually corresponding to the initial coloration of the samples. Residues from dissolution were treated with a 3:1 mixture of concentrated HF and HNO_3 and washed several times (until no visible fluorides were left) in 5% HNO_3 and H_2O followed by centrifugation. Residues were dried on a hot (150°C) plate. Upon drying, all samples (with the exception of GRR1790a) produced residues of visually homogeneous, fine textured, flaky pink-colored mats. Sample GRR-1790a dissolved entirely. The dumortierite sample from Dehesa, CA, did not experience significant weight loss after acid digestion. Ultimately, this acid-treated dumortierite sample was compared to the resistant residues from quartz.

Analytical methods

Imaging and qualitative analysis were performed with Caltech's CAMSCAN Series II scanning electron microscope and associated Link thin-window SiLi detector and EDS analyzer system. Semi-quantitative X-ray fluorescence spectra of all the fiber mats were taken with a Kevex/IXRF 770 EDS system using Ge and Gd secondary targets.

For the XRD analyses, fibers from GRR1815 and dumortierite (Dehesa, CA) were finely ground and loaded on the tip of a glass fiber. Conventional powder diffractometry was not used for two reasons: first, the available sample size was too small, and second, even our finest grinding of the sample produced particles with a very high length to width ratio, minimizing X-ray incidence in the elongated direction of the crystals. X-ray diffraction patterns were obtained with a 57.3 mm diameter Gandolfi camera that introduces 2 axes of rotation to the fibrous sample to ensure a powder diffraction pattern. The films were read with an estimated accuracy of 0.02° in the 2-theta measurements.

Infrared reflectance spectra of all fiber samples and dumortierite were obtained with a Nicolet 60SX FTIR spectrometer. Whole mats of fibers were first placed over a pinhole aperture. Spectra were then obtained with a NicPlan IR microscope at 4 cm^{-1} resolution at near-normal incidence in the reflection mode. In addition, IR transmission spectra from samples GRR1815, GRR1811 and GRR1864 dispersed in KBr pellets were obtained.

A Renishaw 1000 micro-Raman spectrometer with a 2 cm^{-1} resolution was used to obtain Raman spectra of dumortierite and fiber samples. Five samples were examined. Mats of fibers were placed at the microscope focus (20x) and probed with a polarization–scrambled 514.5 nm laser operating at 50 mw.

Optical spectra were obtained using a home-built 1024 element silicon diode-array spectrometer. Spectra of the fiber mats were taken in a reflectance mode by focusing an approximately 2 mm diameter spot of light on the mat and collecting the reflected light at 90° to the incident light. These spectra were compared to massive rose quartz spectra obtained in a diffuse transmission mode. In these experiments light was directed into a rectangular block of rose quartz and light was collected from an adjacent face and directed to the spectrometer. Milky quartz was used as a reference standard in both of these experiments.

RESULTS

Physical characteristics

All massive rose quartz samples produced fibrous residues that, among different samples, varied from only slightly pink to bright pink. Clusters of parallel fibers show strong pleochroism under the optical microscope. They are bright pink parallel to the direction of elongation and near-colorless perpendicular to that direction.

SEM observations and sample chemistry

Fiber samples obtained from dissolution experiments were examined with SEM. Representative back-scattered electron images of the fibers are shown in Figure 1. Figure 1a shows a residual mat from the quartz sample GRR1820 from the Black Hills, South Dakota. The length of the fibers was probably controlled by the grinding of the initial quartz sample. Figure 1b shows a more detailed image of a fiber cluster from the same sample. The width of individual fibers recovered from different samples generally varied between 0.1 to 0.5 μm. The SEM-EDS analyses of the wide (relative to the width of individual crystals) areas of the fiber mats show an aluminosilicate framework with traces Ti and Fe in all samples. The relative intensity of the Al and Si peaks is approximately 2:1. Unfortunately, because of the small size of the individual fibers, quantitative analysis could not be obtained by EDS. No other elements were detected by EDS XRF. In particular, Sb, Ta, Nb and As were absent even though they are found in holtite, a phase related to dumortierite (Hoskins et al. 1989).

An attempt to obtain chemical analyses of fibrous residues with ICP-MS (Elan 5000A) was also made. Residues were dissolved in 10N KOH. The ICP-MS analysis confirmed that boron was present in the fibers at levels of at least 2%, but repeat analyses did not yield reproducible results, presumably as a result of boron loss during the analytical procedure.

Occasional larger tabular crystals were observed in the fiber mats extracted from GRR1819 and GRR1820. A Si-Al matrix and morphology of these crystals suggest an Al_2SiO_5 polymorph, probably sillimanite.

X-ray diffraction

The ten most intense lines for fibers extracted from sample GRR1815 (Madagascar) and dumortierite (Dehesa, CA) are compared (Table 2) with those of the ICDD standard dumortierite (12-0270). The d-spacings from the diffractograms of the powdered fibers and natural dumortierite are close to those of the JCPDS standard dumortierite pattern, although there are differences in intensities.

FTIR spectrometry

The IR spectra of the rose fibers are broadly compatible with the spectrum of dumortierite (Fig. 2). All samples show the borate band at 1450 cm^{-1} that indicates the presence of the BO_3^{3-} ion. Comparison of the absorption spectra of dumortierite and the fibers suggests that these phases have approximately the same borate to silicate ratios. The spectrum of dumortierite from Dehesa, CA, closely matches the synthetic dumortierite spectrum (e.g., sample B12) of Werding and Schreyer (1990), but these spectra consistently differ from those produced by the various fiber samples. Relative band intensity differences in the 1000 and 500-600 cm^{-1} regions are the salient differences.

Raman Spectrometry

Figure 3 shows Raman spectra of a dumortierite crystal (Dehesa, CA), acid-treated dumortierite powder, and three samples of fiber mats from different localities. The two dumortierite spectra are similar, with only minor differences in the relative intensities of two bands in the 500-600 cm^{-1} region. These differences can be attributed to the anisotropy of the single dumortierite crystal, as the spectrum was taken with the incident light perpendicular to the c-axis. The spectra produced by the fibers are virtually identical to each other, but they are significantly different from the spectra generated by dumortierite (Figure 3). Vertical dashed lines in Figure 3 help to illustrate differences in the positions and intensities of the bands.

Optical absorption

Optical absorption spectra of fiber mats from GRR1815, GRR1818, GRR1820 and GRR1874 were compared to the spectra of the corresponding initial rose quartz samples.

The spectra of fiber mats showed an absorption band centered at approximately 500 nm. Moreover, the absorption bands of mats and their rose quartz precursors were nearly identical, indicating that their colors share a common origin (Figure 4). For comparison, an optical spectrum of pink dumortierite (Dehesa, CA) is also presented. In addition to the 500 nm band, it also has a longer wavelength shoulder arising from a second component previously described in Platonov et al (2000).

Irradiation and thermal stability of color

As noted earlier, the heating experiments by Ignatov et al. (1990) showed that their rose quartz and its associated clusters of fibrous inclusions in the quartz loose their color at ~ 500°C. For several minerals, color loss on heating is associated with radiation-induced colors. Since rose quartz occurs in pegmatites, where a number of minerals such as smoky quartz have radiation-induced color, it is plausible that the pink color of rose quartz was developed upon natural irradiation within the pegmatite body. In order to explore this possibility, we subjected quartz sample GRR1815 to three weeks of heating at 750°C in air. The quartz sample lost its rose color, although the overall turbidity of the quartz did not visually increase. The fibrous inclusions extracted from the heated quartz were colorless. The FTIR spectrum of the colorless fibers was virtually identical to the spectrum of the pink fibrous residue from an unheated aliquot of the same rose quartz (Figure 2) and indicates that a phase change did not occur. The colorless fibers then were irradiated in a ^{137}Cs source. After exposure to 10 Mrad of gamma radiation, the fibers did not turn pink, suggesting that a radiation-induced center is not a cause of the color.

After ruling out the irradiation hypothesis, we designed a number of heating experiments to determine if this loss of color was due to the oxidation of transition elements. Experiments were performed on fibers extracted from 13 of the 29 samples studied. All 13 samples of rose fibers lost their color upon heating in air at temperatures between 430° and 750°C. The higher the temperature, the more quickly the fibers lost their color. At 750°C it takes few minutes, whereas at 430°C it takes several days. The colorless fibers were reheated at the same temperatures under highly reducing conditions with a mixture of 95% N_2 and 5% H_2. Eleven out of 13 samples regained their pink color. Samples GRR-1897 and GRR-1904 remained white. Both of these samples contained thicker fibers (~1 _m), so the reaction kinetics might be slower than for the other samples. No phase transitions occurred during the reduction experiments.

DISCUSSION AND CONCLUSIONS

Our work confirms previous observations of aluminosilicate fibers in rose quartz and extends it to numerous localities around the world. After separation from the host quartz, these insoluble fibers are the same color as the initial rose quartz. Thus, we argue that the color of rose quartz itself arises from these fibrous inclusions. Several experiments indicate that these fibers are related to dumortierite. However, there are significant differences between their spectroscopic signatures and those of dumortierite. Nevertheless, dumortierite remains a valid point of comparison to the properties of these fibers.

Dumortierite itself is commonly associated with quartz in hydrothermal and pegmatitic environments. It is common for dumortierite to contain traces of Fe and Ti which are associated with its color (Alexander et al. 1986). An absorption band in the dumortierite spectrum centered at about 500 nm has been attributed to Fe^{2+} - Ti^{4+} IVCT by Ignatov et al. (1990) who also associated the color of dumortierite in association with rose quartz to the color of their sample of rose quartz. Our work supports their proposal for the origin of rose color in dumortierite.

Because the fibers we recovered from rose quartz always show traces of Ti and Fe, we propose that the same Fe-Ti charge transfer mechanism operates in the dumortierite-related fibrous phase extracted from rose quartz. Smith et al. (1978) had previously proposed that a Fe-Ti charge transfer mechanism is responsible for the color of rose quartz but thought that it originated with substitutional components within the quartz itself.

Heating experiments in open air showed that the fibers could easily be rendered colorless. Because we were able to return color to the fibers by heating them under reducing conditions, we believe that oxidation and reduction of iron ($Fe^{2+} \leftrightarrow Fe^{3+}$) in Fe-Ti IVCT centers are responsible for the change of the fiber color from pink to colorless and back. Hemingway et al. (1990) have speculated that the color change that occurs in dumortierite may reflect oxidation of iron and loss of charge transfer among Fe^{2+}, Fe^{3+} and Ti^{4+} rather than dumortierite decomposition. Our experiments demonstrate this mechanism in the fibers.

Our FTIR study of fibers extracted from rose quartz after heating to 750°C showed that the fibers remained structurally unaltered, even though dumortierite reportedly decomposes above ~ 700°C at atmosphere pressure (Werding and Schreyer, 1996).

Ignatov et al. (1990) showed that the color of quartz with the macroscopic dumortierite inclusions is stable below 500°C at 1 atm. and does not depend on the duration of the heating. By contrast, our heating experiments revealed, that there is a time dependence to the color stability of the heated fibers. Fibers lose their color within a few hours when heated at 500°C, whereas decoloration takes several days at 430°C.

Fading of rose quartz

The stability of the color of the fibers appears inconsistent with the often reported fading of the color of some fraction of rose quartz after prolonged exposure to the sun in mine dumps. We have not observed this process in any of our samples and have no direct experimental results to bear on this problem. We speculate that the photo oxidation of iron in the fibers is a plausible but unlikely process. It is further possible, but unproven, that common massive rose quartz could contain a component of the photosensitive phosphorous center found in crystalline pink quartz. This would not explain the lore that some faded rose quartz regains its color when soaked in water. Another, more conservative, explanation for the fading of massive rose quartz would be the solar heat-induced expansion and shattering of CO_2 inclusions causing microfractures and scattering of light near the surface of the quartz.

Origin of the fibers

The origin of the fibers is, in part, related to the origin of rose quartz. A study of primary fluid inclusions in the rose quartz from Black Hills, SD (the locality of the sample GRR1820), shows that crystallization of the quartz occurred in the temperature range 400° to 450°C, at 3.5 to 4 kbars pressure (Sirbescu, 1997, pers. comm., 1998). Because these temperatures are in or near the temperatures at which the rose color was lost in our heating experiments, it seems unlikely that the pink fibrous phase was captured during the growth of the quartz.

Another scenario is that an initially colorless fibrous phase grew within quartz and rose color was gained after crystallization. The lack of response of the colorless fibers to irradiation appears to rule out color generation from a radiation-induced color center. Sirbescu's (pers. comm., 1998) work shows that the composition of the primary inclusions in this quartz is mainly CO_2 with minor CH_4. While the latter indicates plausible reducing conditions in the fluid during the quartz crystallization or crystallization of the inclusions that might affect the oxidation state of Fe, this scenario also seems unlikely.

Our favored explanation is that the pink fibrous phase exsolved from crystallized quartz at temperatures below 430°C. There are many reports of asterism in rose quartz. The most detailed was that of Kalkowsky (1915-20). The asterism in rose quartz implies orientation of fibers perpendicular to *c*- axis and along three equivalent crystallographic directions, which, presumably, is diagnostic of exsolution.

Fine differences between the FTIR and Raman spectra of the fibers and dumortierite could also be due to the presence of an impurity phase. For example, the fibrous mineral inclusions could be a mixture of true dumortierite and a related phase. To address these questions, a more detailed HRTEM and AEM investigation of the chemistry and structure of individual crystals of these fibers is in progress (Chi Ma et al., in prep.).

ACKNOWLEDGMENTS

We thank the White Rose Foundation for their support of our research on color in minerals. We also thank John Brady, Milka de Brodtkorb, Rock H. Currier, Richard V. Gaines, George Harlow, Brian D. Hicks, Lothar Jung, Knut E. Larsen, Taijing Lu, Ole Peterson, Gunnar Raade, Ed Swoboda, Matt Taylor, and Jer Wednt for their interest in our work and for providing quartz samples. We also thank A.N. Platonov for multiple discussions regarding his work, and Liz Arredondo for assistance with laboratory measurements, George Harlow and an anonymous reviewer for valuable comments and Jeffrey Post for the editorial review of the manuscript.

REFERENCES CITED

Alexander, V.D., Griffen, D.T., and Martin T.J. (1986) Crystal chemistry of some Fe- and Ti-poor dumortierites. American Mineralogist 71, 786-794.

Applin, K.R. and Hicks, B.D. (1987) Fibers of dumortierite in quartz. American Mineralogist 72, 170-172.

Bailey, Phillip, and Well, J. (1991) EPR study of the $[SiO_4/Li]^O$ centre in _-Quartz. J. Chem. Soc. Faraday Trans. 87(19), 3143-3146.

Balitsky, V.S., Makhina, I.B., Emelchenko A.G., et al. (1996) Experimental'noe izuchenie usloviy obrazovaniya kristallov rozovogo fosforosoderzhaschego kvarca i prichiny ego redkoy vstrechaemosti v prirode. [Trans. title: Formation of rose phosphorus-bearing quartz and causes of its rarity in nature - an experimental-study]. Geokhimiya, 11, 1074 - 1081 (in Russian).

Cassedanne, J.P. and Roditi, M. (1991) Crystallized and massive rose quartz deposits in Brazil. Journal of Gemmology 22, 5, 273-286.

Cohen, A.J., and Makar, L.N. (1984) Differing effects of ionizing radiation in massive and single crystal rose quartz. Neues Jahrbuch für Mineralogie-Monatshefte 11, 513-521.

Cohen, A.J., and Makar, L.N. (1985) Dynamic biaxal absorption spectra of Ti^{3+} and Fe^{2+} in a natural rose quartz crystal. Mineralogical Magazine 49, 709-715.

Dennen, W.H. and Puckett, A.M. (1971) On the chemistry and color of rose quartz. Mineralogical Record 3, 226-227

Folk, R.L. (1989) Internal structuring of quartz as revealed by boiling concentrated hydrofluoric acid. Journal of Geological Education 37, 250-260.

Gordon, S.C. (1945) The inspection and grading of quartz. American Mineralogist, 30, 269-295.

Hemingway, B.S., Anovitz, L.M., Robie, R.A. and McGee, J.J. (1990) The thermodynamic properties of dumortierite $Si_3B[Al_{6.75}[]_{0.25}O_{17.25}(OH)_{0.75}]$. American Mineralogist 75, 1370-1375.

Holden, E.F. (1924a) The cause of color in rose quartz. American Mineralogist 9(4), 75-89.

------- (1924b) The cause of color in rose quartz (concluded). American Mineralogist 9(5), 101-108.

Hoskins, B.F., Mumme, W.G. and Pryce, M.W. (1989) Holtite, $(Si_{2.25}Sb_{0.75})B[Al_6Al_{0.43}Ta_{0.27})[]_{0.30})O_{15}(O,OH)_{2.25}]$; crystal structure and crystal chemistry. Mineralogical Magazine 35, 457-463.

Ignatov, S.I., Platonov, A.N., Sedenko, V.S., and Taran, M.N. (1990) Pozheve zabravlennya kvarcu, zvyazane z mikrovklyuchennyami dumortyeritu. [Trans. title: Pink coloration of quartz related to dumortierite microinclusions.] Dop. AN URSR. Ser. B. him. ta biol. nauki 7, 23-26 (in Ukranian).

Kalkowsky, E. (1915-20) Opalezierender Quarz. [Trans. title: Opalescent quartz] Zeitschrift für Krystallographie und Mineralogie, 53, 23-50 (in German).

Lehmann, G. (1969) Zur Farbe von Rozenquarz. [Trans. title: On the color of rose quartz] Neues Jahrbuch für Mineralogie-Monatshefte, 222-225 (in German).

Maschmeyer, D. and Lehmann, G. (1983) A trapped-hole center causing rose coloration of natural quartz. Zeitschrift fur Kristallographie 163, 181-196.

Moore, P.B. and Araki, T. (1978) Dumortierite, $Si_3B[Al_{6.75}[]_{0.25}O_{17.25}(OH)_{0.75}]$: A detailed structure analysis. Neues Jahrbuch fur Mineralogie Abhandlungen, 132, 231-241.

Platonov, A.N., Langer, K., Chopin, C., Andrut, M. and Taran, M.N. (2000) Fe^{2+} -Ti^{4+} charge-transfer in dumortierite, European Journal of Mineralogy, 12, 521-528.

Rossman, G.R. (1994) Colored varieties of the silica minerals. In P.J. Heaney, C.T. Prewitt, and G.V. Gibbs, Eds., Silica. Physical Behavior, Geochemistry and Material Applications. Reviews in Mineralogy 29, Mineralogical Society of America, Washington, D.C., p. 433-462.

Sirbescu, M-L. C. and Nabelek, P.I. (1997) Fluid evolution in a simple pegmatite from the Black Hills pegmatite field, South Dakota, Geological Society of America, 1997 annual meeting, Abstracts with Programs - Geological Society of America, 29, p. 457-458, 1997. Geological Society of America, 1997 annual meeting, Salt Lake City, UT, United States, Oct. 20-23, 1997.

Smith, G., Vance, E.R., Hasan, Z., Edgar, A., and Runciman, W.A. (1978) A charge transfer mechanism for the colour of rose quartz. Physica Status Solidi (A) 46, K135-K140.

Vultee, J. von (1955) Über die orientierten Verwachsungen von Rutil in Quartz. [Trans. title: The intergrowth of the oriented rutile inclusons in quartz.] Neues Jahrbuch Fur Mineralogie-Abhandlungen 87, 389-415 (in German).

Vultee, J. von and Lietz, J. (1956) Über die Rolle des Titans als Farbungsursache von Blau- und Rosenquarzen.[Trans. title: About the role of Ti in the pegmentation of the blue and rose quartz.] Neues Jahrbuch für Mineralogie-Monatshefte, 49-58 (in German).

Werding, G. and Schreyer, W. (1990) Synthetic dumortierite, its PTX-dependent compositional variations in the system Al_2O_3-B_2O_3-SiO_2-H_2O. Contributions to Mineralogy and Petrology 105, 11-24.

--------- (1996) Experimental Studies on Borosilicates and Selected Borates. In E.S. Grew and L.M. Anovitz (eds), *Boron. Mineralogy, Petrology and Geochemistry. Reviews in Mineralogy* **33**, Mineralogical Society of America, Washington, D.C., p. 117-159.

Wright, PM., Weil, J.A., Buch, T., and Anderson, J.H. (1963) Titanium colour centers in rose quartz. Nature 197, 246-248.

TABLE 1. Sample locations and descriptions.

Sample ID	Location, City	State, Country	Type of deposit (if known)
GRR-1790a[*]	Alto da Pitora, Galileia	Minas Gerais, Brazil	Pegmatite
GRR-1811	Anza Valley	California, USA	Weathered pegmatite
GRR-1815		Madagascar	Pegmatite
GRR-1818		Namibia	Pegmatite
GRR-1819	Olivera dos Brejinhos	Bahia, Brazil	
GRR-1820	Scott Mine, Custer	South Dakota, USA	Massive vein
GRR-1821	Tobacco Root Mnts	Montana, USA	Massive vein
GRR-1822	Ramshorn Gulch, Tobacco Root Mnts	Montana, USA	Massive vein
GRR-1845	Miass	Ural Mnts, Russia	Pegmatite
GRR-1855	Custer	South Dakota, USA	Pegmatite
GRR-1856c	Shirley Meadows, Kern County	California, USA	Massive vein
GRR-1861		Bahia, Brazil	
GRR-1864	Joai'ma	Minas Gerais, Brazil	
GRR-1871	Obrazek Quarry, Pisek	Czech Republic	Granitic Pegmatite
GRR-1874	Lavra Schupp, Joai'ma	Minas Gerais, Brazil	
GRR-1877	Bedford	New York, USA	Pegmatite
GRR-1885	Madeleine, La Toma	San Luis, Argentina	Massive vein
GRR-1896	Gronoy	Nordland, Norway	Granitic pegmatite
GRR-1897	Amdal	Aust-Agder, Norway	Granitic pegmatite
GRR-1899	Samiresy, Antsirabe	Madagascar	
GRR-1900	Tsaramanga (Tongafeni), Mahaiza	(Fivondronana) Betafo, Madagascar	
GRR-1903	Rossing Berge	Namibia	
GRR-1904	Tammela	Finland	Granitic Pegmatite
GRR-1905	Ilvafjord, Julianehab Fjord	Greenland	
GRR-1906	Rabenstein	Bayern, Germany	Granitic Pegmatite
GRR-1907		China	
GR-7	Schinder Mine, Riverside County	California, USA	Granitic Pegmatite
GR-8	Feno Mine, Riverside County	California, USA	Granitic Pegmatite
CIT-2998	Santa Cruz County	Arizona, USA	
CIT-10416	Washoe County	Nevada, USA	

[*] This specimen is the single-crystal pink quartz.

TABLE 2. XRD d-spacings.

ICDD 12-0270	Dumortierite (Dehesa, CA)	GRR-1815	*hkl*
5.85 (100)	5.84 (100)	5.87 (100)	1 3 0
5.06 (90)	5.07 (85)	5.06 (85)	1 4 0
4.26 (50)	4.27 (60)	4.25 (50)	1 1 1
3.84 (50)	3.83 (55)	3.83 (45)	2 4 0
3.43 (60)	3.43 (85)	3.44 (85)	2 2 1
3.22 (60)	3.21 (80)	3.15 (50)	2 3 1
2.91 (60)	2.90 (75)	2.90 (50)	2 6 0
2.54 (20)	2.54 (55)	-	4 4 0
2.09 (80)	2.09 (90)	2.08 (90)	3 7 1
1.33 (50)	1.34 (70)	1.33 (50)	1 12 2

d-spacings are in Ångstroms, relative intensity (brackets) in %.

FIGURE CAPTIONS

Figure 1. SEM backscattered-electron images of the purified fibrous residue obtained after dissolution of rose quartz. a) sample GRR-1820 (Custer, SD), low resolution image showing the large length-to-width ratio of the fibers; b) sample GRR-1820, higher resolution of a separate cluster of fibers. Individual fibers in this strand are about 100 nm wide.

Figure 2. FT infrared spectra of a) the natural dumortierite (Dehesa, CA), and b) fibrous material from sample GRR-1815 (Madagascar) before and c) after the heating as described text. The intensity differences observed in the 1000 and 500-600 cm^{-1} regions between the standard and the fibers were observed in the spectra of all fibers examined.

Figure 3. Raman spectra of a) dumortierite (Dehesa, CA) crystal, b) dumortierite (Dehesa, CA) acid-treated powder; and fibrous mats from the samples c) GRR-1811, d) GRR-1815, e) GRR-1861. Vertical dashed lines help to illustrate differences in the position of the bands. The spectra of fiber samples are nearly identical, whereas the apparent differences in the 350-600 cm^{-1} region between the dumortierite standard and the fibers are observed.

Figure 4. The optical absorption spectra of the extracted fibrous mat and corresponding crystal of rose quartz from GRR-1815 (Madagascar). The two spectra, offset vertically for clarity, both have an absorption band at about 500 nm. The spectrum of dumortierite from Dehesa, CA, is shown for comparison.

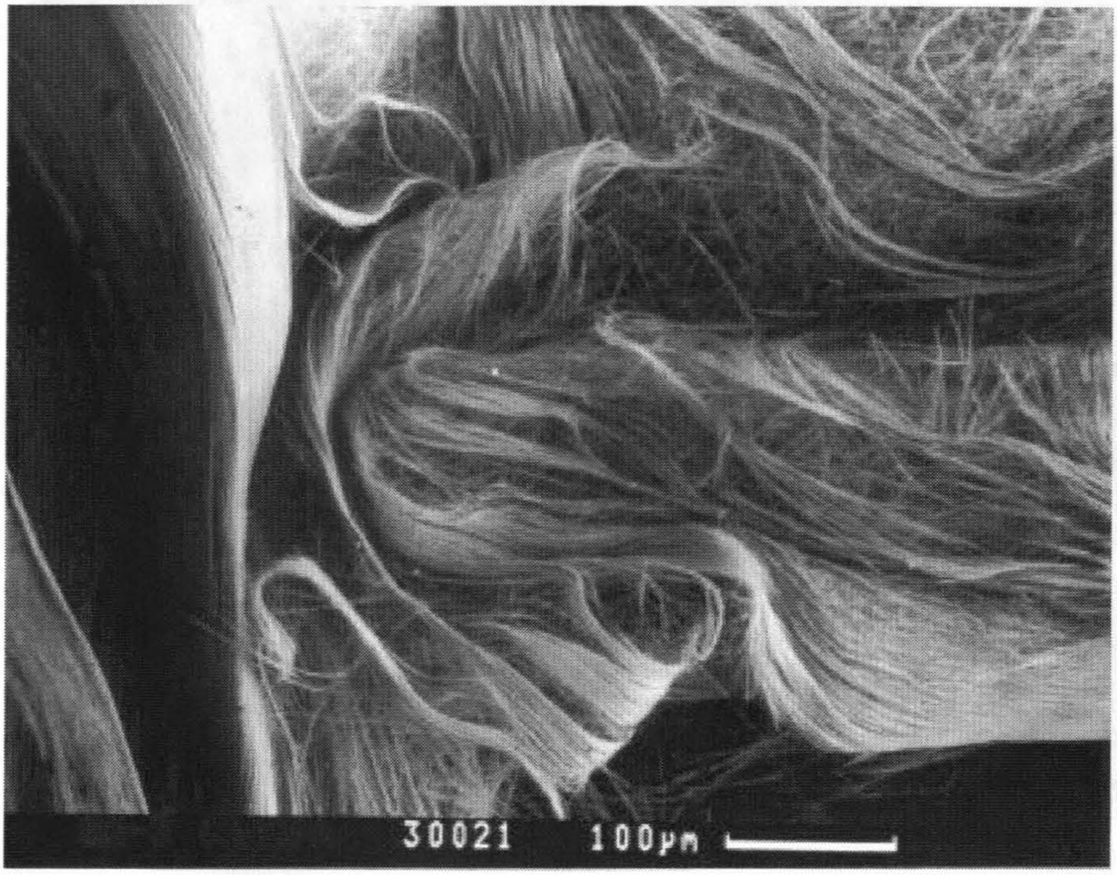

Figure 1a.

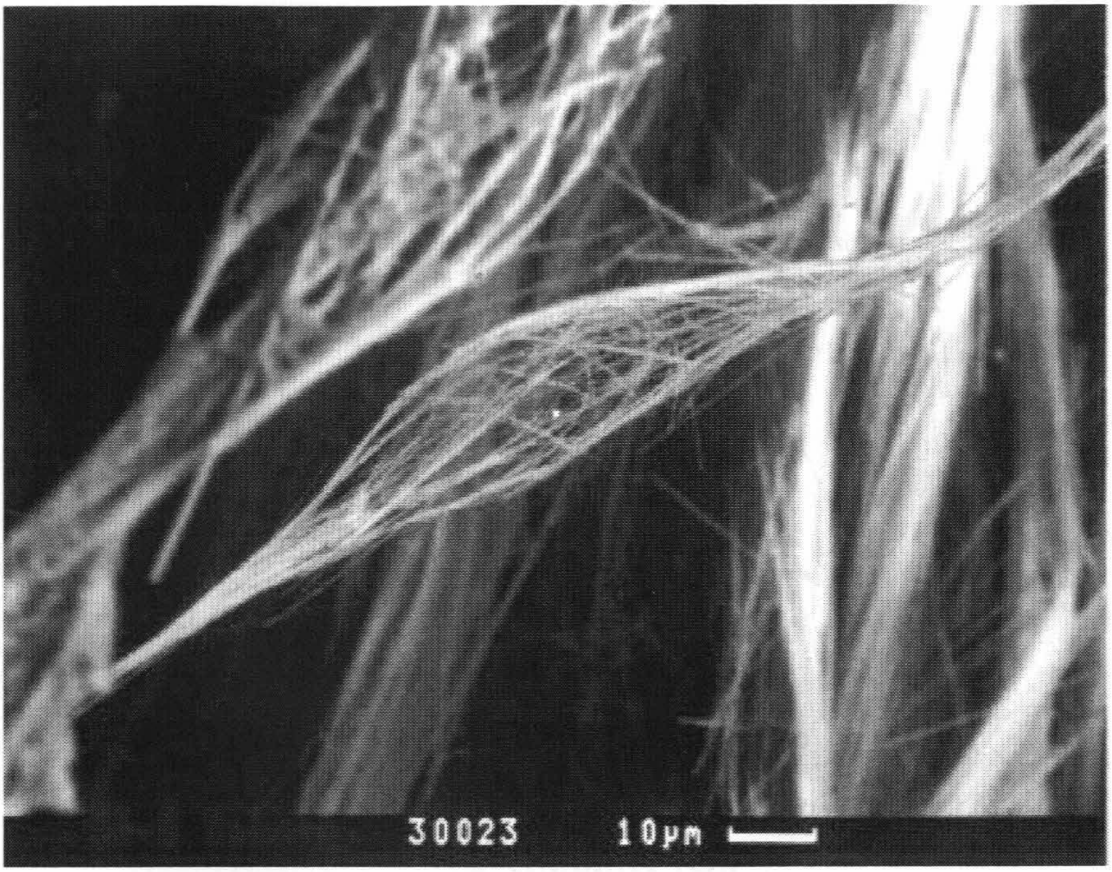

Figure 1b.

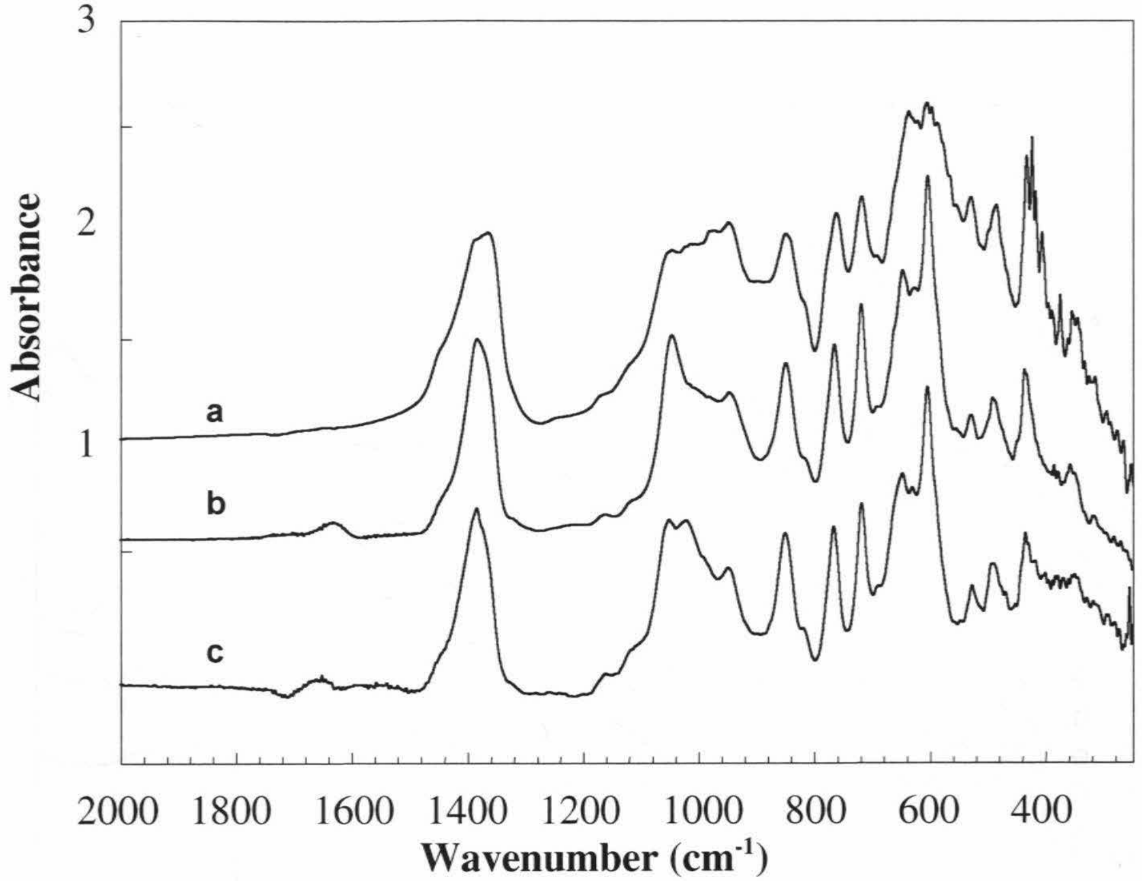
3
2
1
Absorbance
a
b
c
2000
1800
1600
1400
1200
1000
800
600
400
Wavenumber (cm^{-1})

Figure 2.

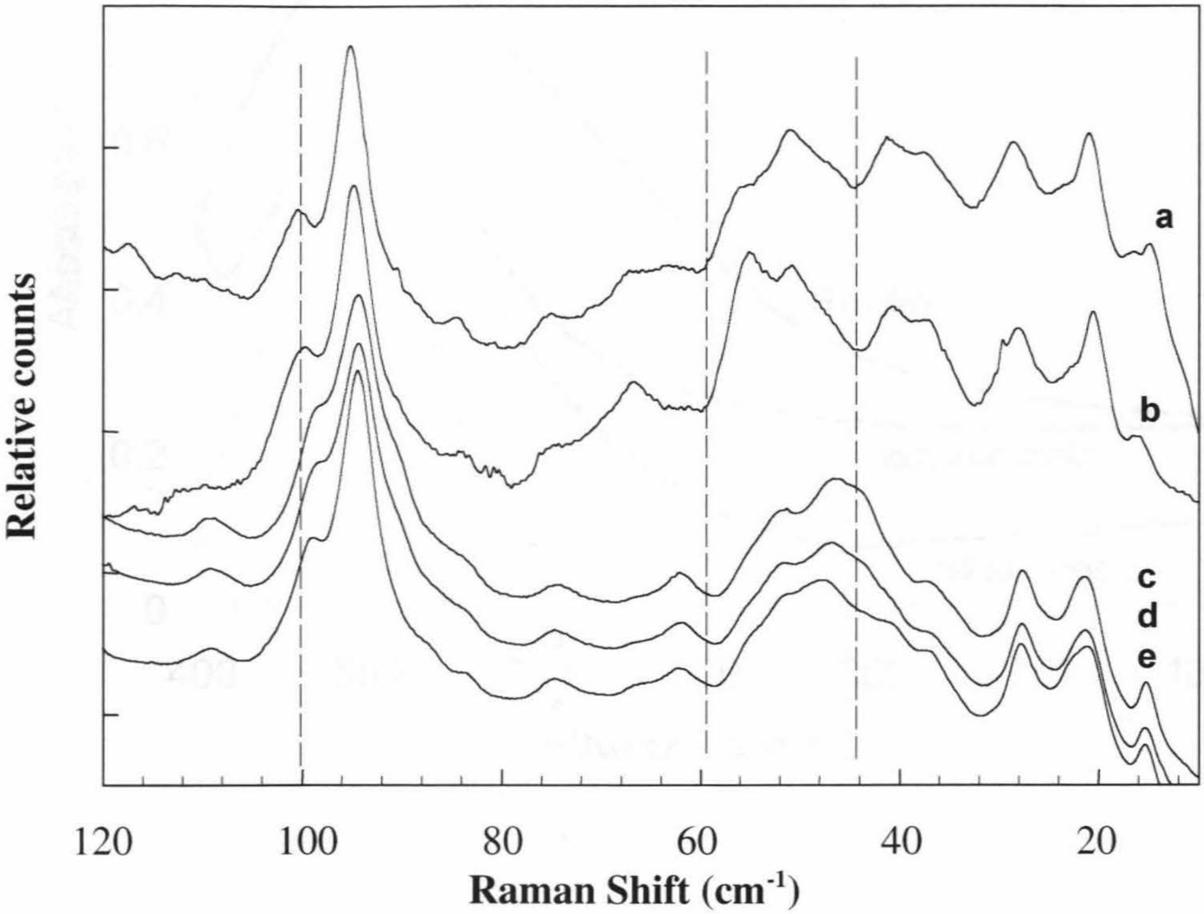

Figure 3.

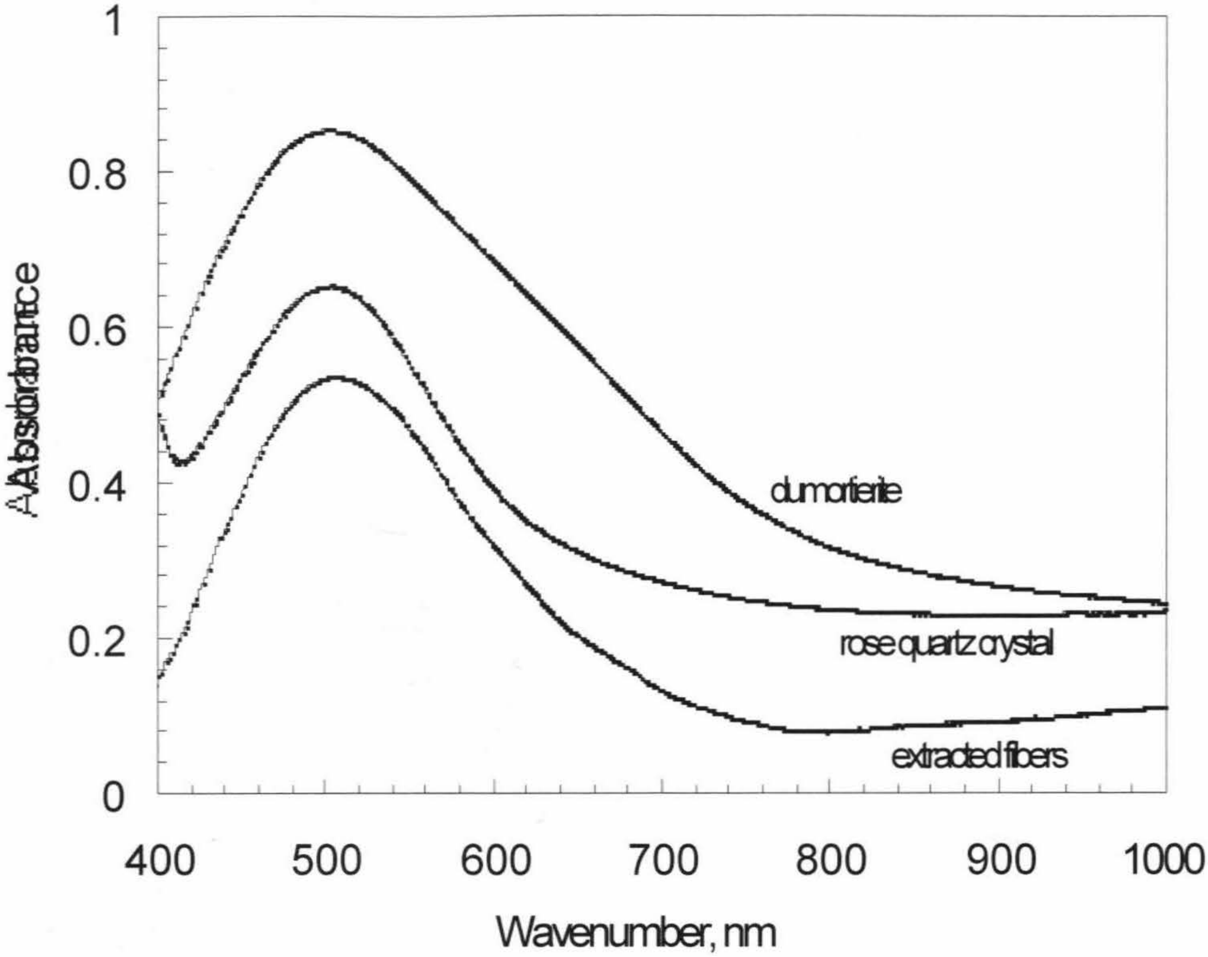
1
0.8
0.6
0.4
0.2
0
Absorbance
400
500
600
700
800
900
1000
Wavenumber, nm
dumortierite
rose quartz crystal
extracted fibers

Figure 4

Appendix II. Fibrous nanoinclusions in massive rose quartz. Part II: HRTEM & AEM investigations.

This manuscript is to be submitted to the *American Mineralogist*, 2001.

Fibrous nanoinclusions in massive rose quartz.

Part II: HRTEM & AEM investigations

Chi Ma, Julia S. Goreva, and George R. Rossman

Division of Geological and Planetary Sciences

California Institute of Technology, Pasadena, CA 91125, USA

ABSTRACT

Pink fibrous crystals within massive rose quartz from localities in California, South Dakota, Brazil, Madagascar and Namibia were examined with high-resolution transmission electron microscopy (HRTEM) and analytical electron microscopy (AEM). This study reveals that the nano-fibers in all samples are related to dumortierite. Selected-area electron diffraction (SAED) patterns and HRTEM images indicate that the dumortierite-related fibers have a superstructure with a doubled repetition period along the $\underline{x}$- and $\underline{y}$- axes of dumortierite, giving cell parameters $a = 2a_{\text{dum}} = 2.36$ nm, $b = 2b_{\text{dum}} = 4.05$ nm, $c = c_{\text{dum}} = 0.47$ nm. Computer simulations suggest that periodic arrangements of two different M(1) site occupations in the octahedral face-sharing chains give rise to the superstructure. One type of M(1) site is occupied mainly by Al, whereas the other type is dominated by Ti and Fe. Simulated structural images based on our proposed model match the experimental structural images. Most of the fibers, elongated along the $\underline{z}$-axis, are free of defects. AEM analysis shows that the chemical composition of the dumortierite-related fibers is similar to well characterized dumortierite, but contains a greater amount of Fe substituting for Al in the M(1) sites. B was detected in all fibers examined by electron energy loss spectroscopy as well as in sillimanite crystals found as a minor component in one rose quartz from Brazil.

Key Words: Fibers, rose quartz, borosilicate, dumortierite, superstructure, sillimanite, HRTEM, AEM, SAED, Image simulation.

INTRODUCTION

Fine fibers in massive rose quartz have been observed and, since the 1930's, were generally presumed to be rutile (reviewed by Rossman, 1994, and Goreva et al, 2000). Applin and Hicks (1987) concluded that the fiber phase in rose quartz from a Montana locality is dumortierite based on their TEM and powder XRD analyses. However, their fibers' XRD peaks are not well matched with dumortierite's peaks in many details. Our XRD on bulk fibers from rose quartz from a variety of localities also show similar results (Goreva et al., 2000). Significant differences observed in the IR and Raman spectra of these fibers, however, cast doubt on their identification as dumortierite. These differences were the motivation for a more detailed TEM study of the fibers. Most fibers in massive rose quartz are less than 1 μm in thickness and ideal for TEM examinations (Fig. 1). Previously the only published TEM results on those fibers were those of Applin and Hicks who showed that the c-axis repeat of the fibers from the Montana locality was appropriate for dumortierite. We present here a detailed analysis of the structural nature of individual fibers based on HRTEM and AEM studies.

EXPERIMENTAL PROCEDURES

Samples

Rose quartz samples were selected from Madagascar (GRR1815), Olivera dos Brejinhos in western Bahia, Brazil (GRR1819), Joai'ma, Minas Gerais, Brazil (GRR1864), Rossing (not stated in the original sample description as received, but inferred from the sample), Namibia (GRR1818), Scott Mine, Custer, South Dakota (GRR1820), and Schindler Mine, Riverside County, California (GRR1996). All rose quartz samples are from pegmatite deposits. Under routine examination at 400x with an optical microscope, mineral inclusions were observed in only two of the samples selected for this study. In these two samples numerous (GRR1864) and occasional (GRR1819) needle-like crystals up to 10 μm in thickness are present.

Fibers were extracted by dissolution of the crushed quartz in HF and then were concentrated and purified. More information on these specimens and fiber purification procedure is given in Goreva et al. (2000). For comparison, detailed, parallel studies were conducted on a well-characterized blue dumortierite standard from Saharina, Madagascar (GRR347), studied by Moore and Araki (1978). Electron diffraction patterns were also obtained from pink dumortierite from Dehesa, San Diego County, California (GRR122), and blue dumortierite from the Cargo Muchacho Mountains, Imperial County, California (CIT14110).

Transmission electron microscopy

A JEOL Atomic Resolution Microscope (ARM) operated at 800 kV and an In-situ JEOL 200CX TEM in the National Center for Electron Microscopy (NCEM), Lawrence Berkeley Laboratory (LBL), a Philips EM430 STEM operated at 300 kV at Caltech and an ISI TEM operated at 200 kV at the Jet Propulsion Laboratory were used for HRTEM imaging and/or electron diffraction analysis. AEM analysis was performed with a JEOL 200CX at the NCEM, LBL. The JEOL 200CX is equipped with a high angle energy dispersive x-ray spectrometer (EDS) and a Gatan 666 electron energy loss spectrometer with parallel detection (PEELS) capable of routinely achieving 1.5eV resolution. The *k* factors for the fiber quantitative EDS analysis were obtained using dumortierite, sillimanite, titanite and andradite as standards under the same analytical conditions.

TEM specimens of the fibers were prepared in two ways: (1) crushed fiber particles dispersed on a carbon film supported by a copper grid so the elongation of fibers is almost parallel to the film, (2) sectioning with a diamond microtome to produce thin sections of the fiber normal to the electron beam. The dumortierite standard was prepared by dispersing crushed crystals on a carbon film. Nearly 1000 photos were recorded during this study, allowing confidence that the observations are representative.

HRTEM simulations

Computer simulations of HRTEM images and electron diffraction patterns were preformed using the *NCEMSS (version 1.6)* software package provided by Dr. Roar Kilaas. The calculations were carried out with a *Sun* workstation. The input structure parameters for dumortierite (*Pmcn*, a = 1.1828 nm, b = 2.0243 nm, c = 0.47001 nm) and sillimanite (*Pbnm*, a = 0.7479 nm, b = 0.7670 nm, c = 0.5769 nm) were based on Moore and Araki (1978) and Peterson and McMullan (1986), respectively. Two-dimensional structural images were simulated with the multi slice approach for a typical range of microscope defocus values, crystal thicknesses, and crystal orientations, using a set of optical constants appropriate for the ARM, Philips EM430 and JEOL 200CX microscopes. The simulated and experimental images are compared visually for interpretation. Figure 2 illustrates computed HRTEM images of the dumortierite structure at different orientation, thickness and defocus conditions. The simulations show that image details are highly sensitive to defocus, orientation and the calculated range of specimen thickness. Hundreds of simulated images were generated in this study to assist in interpreting experimental atomic images.

RESULTS

Electron diffraction

Selected-area electron diffraction (SAED) patterns of the zone-axes were obtained from a number of single fiber crystals. Figure 3 shows representative zone-axis SAED patterns of single fibers from rose quartz, comparing with same zone-axis patterns of the dumortierite standard. The SAED patterns, obtained from different orientations of the fibers, are assigned to [100], [010], [110], [111] and [001] zone-axis electron diffraction patterns based on a dumortierite structural model. The [010], [110] and [111] patterns were observed from the same area of a single fiber through tilting. The [100] zone-axis pattern is almost identical to the dumortierite pattern. However, the [110] and [111] zone-axis patterns of the fibers show weak but relatively sharp reflections along the [1-10]* direction at _(1-10)$_{\text{dum}}$*. This indicates that the fiber has a periodicity along [1-10]* = 2d(1-10)$_{\text{dum}}$, which implies a superstructure of dumortierite with a doubled repetition period along both the $\underline{x}$- and the $\underline{y}$-axes (i.e., $a_{\text{super}} = 2a_{\text{dum}} = 2.38$ nm; $b_{\text{super}} = 2b_{\text{dum}} = 4.05$ nm). The [110] zone-axis pattern of a fiber can be easily mistaken for a [100]-zone pattern (Fig. 3A). However, the intensity distributions of the reflections are different. This superstructure was observed in the electron diffraction pattern of fibers from all localities examined. It was not observed in any of the electron diffraction patterns of the dumortierite samples.

Figure 4A contains a series of computed electron diffraction patterns from a well-oriented dumortierite crystal with uniform 10 nm thickness. The almost identical [100] zone-axis patterns from a fiber and from the dumortierite standard (Fig. 3) are not well matched with the simulated [100]-zone pattern of dumortierite (Fig. 4A) since dynamic diffraction causes the presence of forbidden reflections such as (001) and (0*k*0) where *k* = 2n+1 in the experimental SAED patterns.

The [001] zone-axis SAED patterns of the fibers and dumortierite are also similar and are matched closely with the simulated pattern of dumortierite (Fig. 3 & 4A).

SAED patterns show that nearly all fibers in rose quartz have a superstructure of the dumortierite structure, and are elongated along the *z*-axis. Few [11*l*]-zone single-crystal SAED patterns indicate that a very small number of fibers might have the dumortierite structure because there are no weak reflections along the [110]* direction at _(110)*. Such patterns, however, might be from a thin domain where the superstructure information has weakened and/or has been damaged by the electron beam. The zone-axis SAED patterns of reference dumortierite (GRR347) examined in this study reveal that the dumortierite crystal has the ideal structure proposed by Moore and Araki (1978) (e.g., Fig. 3B and 4A). These patterns are consistent with the simulated dumortierite electron diffraction patterns.

Most SAED patterns of single fiber crystals are clear without diffusive streaking. This indicates that most fiber crystals have an ordered structure. Only a few electron diffraction patterns revealing the superstructure show weak streaking (e.g., Fig. 3A) along [1-10]*. The HRTEM images show that the streaking was not derived from stacking faults but more likely was from uneven cation occupations in the M(1).

Convergent-beam electron diffraction patterns were also obtained from some dumortierite-related fibers. Figure 5 illustrates a [010]-zone whole pattern of a fiber showing a weak First-Order Laue Zone (FOLZ) and a sharp Second-Order Laue Zone (SOLZ). The FOLZ reveals that the repeat along [010] is 4.05 nm (i.e., the periodicity of the fiber along the $\underline{y}$-axis = $2b_{\mathrm{dum}}$).

HRTEM imaging

Bright-field images at low-magnification reveal the fibers' morphology (Fig. 1). In general, the fibers vary in thickness mainly from 100 nm to 800 nm but can be up to 1200 nm. Two-dimensional structural images from a number of single fibers were obtained along with their zone-axis SAED patterns.

HRTEM images indicate that the fibers are almost free of stacking faults, deformation and dislocations. HRTEM images (Fig. 6) of single fibers corresponding to the orientation of the [110] and [111]-zone SAED patterns (Fig. 3A) show that the true periodicity along the [110] direction is 2.04 nm and the subperiodicity of 1.02 nm appears in the thin area. Figure 7 illustrates the [100] zone-axis images showing sub-periodicity of 2.02 nm along [010]. Cross-sections of the fibers (Fig. 8) reveal (010), (100), (110) and (140) surface planes indexed according to the dumortierite superstructure. A single (110) twin was observed in only one fiber.

The irregular-shape of the surface layer (< 2 nm thick) of the fibers in Figure 6B, is likely caused by electron beam damage. In general electron beam damage on the fiber phase is not serious although the knock-on damage plays a role in degrading its structural ordering.

Chemistry

AEM analysis on individual fibers shows that in all samples the fibers from rose quartz are aluminum-borosilicates, having a chemical composition similar to dumortierite. Mean structural formulae of the fibers are given in Table 1. EDS analysis reveals that the fibers contain a small amount of Ti and Fe substituting for Al. The Fe content varies slightly. The contents of Ti and Fe are slightly higher than in blue dumortierite (Fig. 9), but overlap the range of these elements in pink dumortierite (Alexander et al. 1986). In the fibers from rose quartz, Ti content is generally greater than Fe content. Ti and Fe are believed to occupy the M(1) sites in dumortierite (Platonov et al. 2000). The composition of the fibers is plotted together with the compositions of dumortierites in Figure 9. FTIR analyses on bulk, extracted fibers, including those used in this study, reveal that borate is present in about the same B to Si ratio as in dumortierite (Goreva et al. 2000). PEELS analysis reveals that B is present in each single fiber from rose quartz (Fig. 10A). Although attempts to obtain reproducible quantitative PEELS analyses were, in part, frustrated by the irregular shape and thickness of the individual samples, these analyses also show that the B content of the fibers is comparable to that of dumortierite (Fig.10B).

Other fibers and phases

In several recent books and articles, rutile fibers (TiO_2) are still considered to be the cause of color in rose quartz. A control experiment with light yellow rutilated quartz (CIT 5585, Minas Gerais, Brazil) demonstrated that fine rutile needles (1.5 μm wide -

identity verified by Raman spectroscopy) survive our acid dissolution process intact. Thus, if rutile fibers were present in rose quartz in significant numbers, we should detect them. However, rutile fibers were not found in any of our rose quartz samples. Along with the dumortierite-related fibers, a significant proportion of acicular sillimanite nanocrystals (~ 10%) were admixed with the fibers extracted from one sample of Brazilian rose quartz (GRR1864). Figure 11 illustrates a HRTEM image of a sillimanite crystal with its [110] zone-axis SAED pattern, which is closely matched to the calculated image and electron diffraction pattern. The composition of the sillimanite crystals is almost identical to Al_2SiO_5 (Table 1). PEELS analysis shows that boron occurs in the sillimanite (Fig. 10C). The B content appears not to be caused by contamination of dumortierite-related fibers, or inclusions in sillimanite of borosilicates with BO_3 groups. This is consistent with a prior observation of boron in macroscopic sillimanite (Grew and Rossman 1985). Similar, but larger (up to 15 μm wide) acicular Al_2SiO_5 crystals were observed as a minor component in the SEM images of fibers extracted from samples GRR1819 and GRR1820 of Goreva et al. (2000) and were presumed to also be sillimanite.

The intensity of the boron K edge in the PEELS spectrum of the sillimanite nanocrystals is visually as evident as it is for dumortierite (Fig. 10). However, this does not necessarily indicate that B content of the sillimanite needles is as high as it is in dumortierite because the PEELS spectra were obtained under different conditions (e.g., crystal thickness, orientation).

DISCUSSION

Experimental TEM results in this study indicate most fibers from rose quartz are a superstructure of dumortierite with a doubled repetition period along both the *x*- and the *y*-axes. The superstructure can be modeled based on a periodic variation of the M(1) position in the dumortierite structure. The ideal dumortierite structure consists of three chain types (each built of AlO_6 octahedra) which run parallel to the *z*-axis: $^{1}_{\times}[M(1)O_3]$ face-sharing chain, $^{1}_{\times}[M(4)_4O_{12}]$ double chains, and $^{1}_{\times}[M(2)_2M(3)_2O_{12}]$ chains (Moore and Araki 1978). The M(2), M(3) and M(4) sites are occupied totally by Al. The M(1) site is occupied mainly by Al and cation vacancies in a 3:1 ratio in normal dumortierite (Moore and Araki 1978), and by Mg in magnesiodumortierite (Chopin et al. 1995). The AEM analyses of individual fibers show the presence of Ti and Fe (Table 1). These two cations are assigned to the M(1) site in dumortierite (Alexander et al. 1986). We suggest that there are two types of cation occupations in the M(1) site; they are

Type I: Al,

Type II: Ti + Fe.

On this crystal-chemical basis, a model for the superstructure is constructed, as illustrated in Figure 12. In this model, viewed down the [001] direction, the Type II site is surrounded by Type I sites along the [100], [110] and [010] directions of the dumortierite structure. The superstructure derives from the regular distribution of these two types of cation occupations in the M(1) site. In the superstructure unit, three quarters of the M(1) sites are Type I (Al) and one quarter are Type II (Ti and Fe). The stoichiometry of this model, $[Al_6(Al_{0.75})^{I}(Ti,Fe)^{II}_{0.25}]Si_3BO_{18}$, comes close to predicting the experimentally determined composition of the fibers in Table 1. The model does not exclude minor amounts of Ti and Fe in the Type I Al position nor does it exclude cation vacancies in either the Type I or Type II cation sites.

The simulated electron diffraction patterns of this model model (*Pmcn*, $a = 2.3656$ nm, $b = 4.0486$ nm, $c = 0.47001$ nm) (Fig. 4B) match well with the experimental SAED patterns of the dumortierite-related fibers (Fig. 3A). The simulated HRTEM images also closely match the experimental images of the fibers (Fig. 13). These simulations indicate that the superstructure occurring in the fibers indeed has such a cation configuration.

The streaking along the [110] direction in some SAED patterns of single fibers might correspond to some cation disordering in the M(1) sites. The chemistry of the fibers (Table 1) shows an average $Al_{0.66}$ $Ti_{0.18}$ $Fe_{0.13}$ per formula in the M(1) site, which suggests that about 20% of the Ti and Fe are located in the Type I position with Al. It is likely that uneven distribution of those Ti and Fe in the Type I position give rise to the streaking along [1-10]* on some of the fibers' SAED patterns.

It is apparent that Ti and Fe in the Type II position of the M(1) site are disordered along the $\underline{z}$-axis, whereas Al in the Type I position is ordered in the M(1) site or partly disordered when minor Ti, Fe or vacancies are present in the Type I position along with Al. This model predicts that in the fibers $c = c_{\text{dum}} = 0.47$ nm without a doubled or tripled repetition, as is observed in the experimental electron diffraction results.

If Al, Ti and Fe are randomly distributed in the M(1) site along z*, the dumortierite structure occurs. This might be the case for a few fibers whose [11*l*] SAED patterns are almost identical to these of ideal dumortierite crystals.

Our model indicates that the pink color of the fibers results from intervalence charge transfer between Fe^{2+} and Ti^{4+} in the M(1) site. A similar mechanism has previously been proposed as the cause of color of dumortierite (Alexander et al., 1986; Platonov et al., 2000). Although the fibrous borosilicate phases observed by HRTEM may seem volumetrically insignificant in rose quartz (Goreva et al. 2000), they are crucial to the very definition of rose quartz.

It is possible, that the fine acicular sillimanite crystals extracted from GRR1864 are cogenetic with the comparably sized dumortierite-like fibers. This would indicate that both phases were formed by exsolution from the quartz. However, formation of larger sillimanite crystals microscopically observed in GRR1864, and in samples GRR1819 and GRR1820 of Goreva et al. (2000) were most likely incorporated through crystal capture during the growth of the quartz. Ironically, these microscopically visible needles that captured the attention of many researchers appear to have no relationship to the origin of color of rose quartz.

These observations raise the question of whether the ordering we observe in the fibers is a result of growth at a lower temperature than usual for dumortierite. It is reasonable to expect that exsolved phases might display higher ordering than their directly crystallized counterparts because lower temperature formation generally leads to higher order. In our case, exsolution presumably occurred at a temperature below 400°C. In this respect, it would be interesting to find a locality with multiple generations of dumortierite formed at different temperatures and examine the state of ordering in the mineral.

CONCLUSIONS

Borosilicate fibers exist in massive rose quartz from vein deposits and pegmatites worldwide and they are the cause of the pink color of rose quartz (Goreva et al. 2000). These sub-micrometer wide, pink fibers are related to dumortierite. Nearly all of them have a previously uncharacterized superstructure of dumortierite with a doubled repetition period along both the $\underline{x}$-and the $\underline{y}$-axes. Computer simulations show that the superstructure is due to an ordered arrangement of two types of cation occupations on the dumortierite M(1) site. We propose that the color of the fibers is due to Fe^{2+} - Ti^{4+} intervalence charge transfer in one of the M(1) sites.

ACKNOWLEDGMENTS

We thank Ulrich Dahmen and Christian Kisielowski for allowing us to access the ARM and the JEOL 200CX microscopes at the National Center for Electron Microscopy, Lawrence Berkeley National Laboratory, Roar Kilaas for helping with the NCEMSS image simulation program, Chengyu Song for assisting with the ARM operation, and Thomas George for allowing us to use the ISI 200 kV HRTEM at the Jet Propulsion Laboratory. Lothar Jung (Quartz Technology, Inc.), Rock H. Currier (Jewel Tunnel Imports) and Edward Swobota (Beverly Hills, CA) provided quartz samples used for this study. Funding for this project was provided by the White Rose Foundation.

REFERENCES CITED

Alexander, V.D., Griffen, D.T., and Martin, T.J. (1986) Crystal chemistry of some Fe- and Ti-poor dumortierites. American Mineralogist, 71, 786-794.

Applin, K.R., and Hicks, B.D. (1987) Fibers of dumortierite in quartz. American Mineralogist, 72, 170-172.

Chopin, C., Ferraris, G., Ivaldi, G., Schertl, H.-P., Schreyer, W., Compagnoni, R., Davison, C., and Davis, A.M. (1995) Magnesiodumortierite, a new mineral from very-high-pressure rocks (western Alps). II. Crystal chemistry and petrological significance. European Journal of Mineralogy, 7, 525-535.

Goreva, J., Ma, C., and Rossman, G.R. (2000) Fibrous nanoinclusions in massive rose quartz. Part I: The source of rose coloration. (Submitted to the American Mineralogist).

Grew, E.S., and Rossman, G.R. (1985) Co-ordination of boron in sillimanite. Mineralogical Magazine, 49, 132-135.

Moore, P.B., and Araki, T. (1978) Dumortierite, $Si_3B[Al_{6.75}[]_{0.25}O_{17.25}(OH)_{0.75}]$: A detailed structural analysis. Neues Jahrbuch fur Mineralogie Abhandlungen, 132, 231-241.

Peterson, R.C., and McMullan, R.K. (1986) Neutron diffraction studies of sillimanite. American Mineralogist, 71, 742-745.

Platonov, A.N., Langer, K., Chopin, C., Andrut, M., Taran, M.N. (2000) Fe^{2+}-Ti^{4+} charge transfer in dumortierite. European Journal of Mineralogy, 12, 521-528.

Rossman, G.R. (1994) Colored varieties of the silica minerals. In: Silica Physical Behaviour, Geochemistry and Materials applications. Heaney, P.J., Prewitt, C.T. and Gibbs, G.V. (editors). Reviews in Mineralogy, 29, 433-467.

Table 1. Mean chemical formula of the fibers in rose quartz and reference dumortierite by AEM (EDS) analysis.

Sample No.	Locality	Dumortierite-related fibers[*]
GRR1815	Madagascar	$(\mathrm{Al}_{6.71}\,\mathrm{Ti}_{0.15}\,\mathrm{Fe}_{0.13})\,\mathrm{Si}_{3.00}\,\mathrm{B}\,\mathrm{O}_{18}$
GRR1818	Namibia	$(\mathrm{Al}_{6.64}\,\mathrm{Ti}_{0.17}\,\mathrm{Fe}_{0.15})\,\mathrm{Si}_{3.02}\,\mathrm{B}\,\mathrm{O}_{18}$
GRR1819	Bahia, Brazil	$(\mathrm{Al}_{6.68}\,\mathrm{Ti}_{0.17}\,\mathrm{Fe}_{0.13})\,\mathrm{Si}_{3.01}\,\mathrm{B}\,\mathrm{O}_{18}$
GRR1864	Minas Gerais, Brazil	$(\mathrm{Al}_{6.58}\,\mathrm{Ti}_{0.25}\,\mathrm{Fe}_{0.09})\,\mathrm{Si}_{3.02}\,\mathrm{B}\,\mathrm{O}_{18}$
GRR1996	Schindler Mine, CA	$(\mathrm{Al}_{6.68}\,\mathrm{Ti}_{0.17}\,\mathrm{Fe}_{0.13})\,\mathrm{Si}_{3.01}\,\mathrm{B}\,\mathrm{O}_{18}$
		Reference Dumortierite[*]
GRR347	Saharina, Madagascar	$(\mathrm{Al}_{6.86}\,\mathrm{Ti}_{0.06}\,\mathrm{Fe}_{0.06})\,\mathrm{Si}_{3.02}\,\mathrm{B}\,\mathrm{O}_{18}$
		Sillimanite microcrystals[†]
GRR1864	Minas Gerais, Brazil	$\mathrm{Al}_{1.98}\,\mathrm{Fe}_{0.02}\,\mathrm{Si}_{1.00}\,\mathrm{O}_{5}$

[*] Formulas are normalized to BO_{18}.

[†] Normalized to O_5.

Table 2. Representative cell parameters

Cell parameters	dumortierite*	fibers (GRR 1815)	superstructure model
a_0	1.1828 nm	2.36 nm	2.3656 nm
b_0	2.0243 nm	4.05 nm	4.0486 nm
c_0	0.47001 nm	0.47 nm	0.47001 nm

* From Moore and Araki (1978)

Figure Captions

Figure 1. Low-magnification bright field image showing the dispersed crushed fibers on a carbon film. The fibers are from a rose quartz from Madagascar (GRR1815).

Figure 2. Simulated HRTEM images of dumortierite with different orientations and at different thickness and defocus conditions using optical constants for the Philips EM430. (A) [100]-zone, (B) [110]-zone.

Figure 3. (A) Representative zone-axis SAED patterns of single fibers obtained from different orientations: [100], [010], [110], [111] and [001]. (B) Zone-axis SAED patterns of the dumortierite standard from [100], [110], [111] and [001]. All indices are based on the dumortierite structure determined by Moore and Araki (1978).

Figure 4. (A) Simulated electron diffraction patterns of dumortierite in perfect orientations with uniform 10 nm thickness from [100], [010], [110], [111] and [001]. (B) Simulated electron diffraction patterns of the superstructure model (see Discussion) with uniform 10 nm thickness from [100], [010], [110], [112] and [001].

Figure 5. The [010]-zone whole pattern of a fiber from GRR1819 showing the First-Order Laue Zone (FOLZ) and the Second-Order Laue Zone (SOLZ).

Figure 6. HRTEM images of single fibers showing 2.04 nm real-periodicity along the [110]* direction and 1.02 nm subperiodicity at a thinner area. (A) The [110]-zone, (B) the [112]-zone.

Figure 7. HRTEM images of single fibers down the [100] zone-axis showing only subperiodicity along the [010] direction. That is $d(020)_{\text{super}} = b_{\text{dum}}$.

Figure 8. [001] zone-axis HRTEM images of a fiber from GRR1815 showing its cross section.

Figure 9. Octahedral cation contents in the fibers from rose quartz (this study), classic dumortierite (Alexander et al. 1986) and magnesiodumortierite; Chopin et al. 1995).

Figure 10. PEELS spectrum of (A) a dumortierite-related fiber (GRR1819), (B) the dumortierite standard (GRR347), and (C) a sillimanite nanocrystal (GRR1864). The boron K edge is evident in all spectra.

Figure 11. (A) A thin sillimanite crystal from GRR1864. (B) [110] zone-axis HRTEM image of the sillimanite crystal from GRR1864 and its SAED pattern.

Figure 12. The superstructure model ($a = 2a_{\mathrm{dum}}$, $b = 2b_{\mathrm{dum}}$, $c = c_{\mathrm{dum}}$). The superstructure is strongly psuedohexagonal, with $\underline{z}$ the pseudohexad axis. There are two types of M(1) chain: Type I filled with Al and Type II occupied by Ti and Fe.

Figure 13. HRTEM images of single fibers viewed down the (A) [112] and (B) [110] directions, matched with the inserted simulated images using the superstructure model.

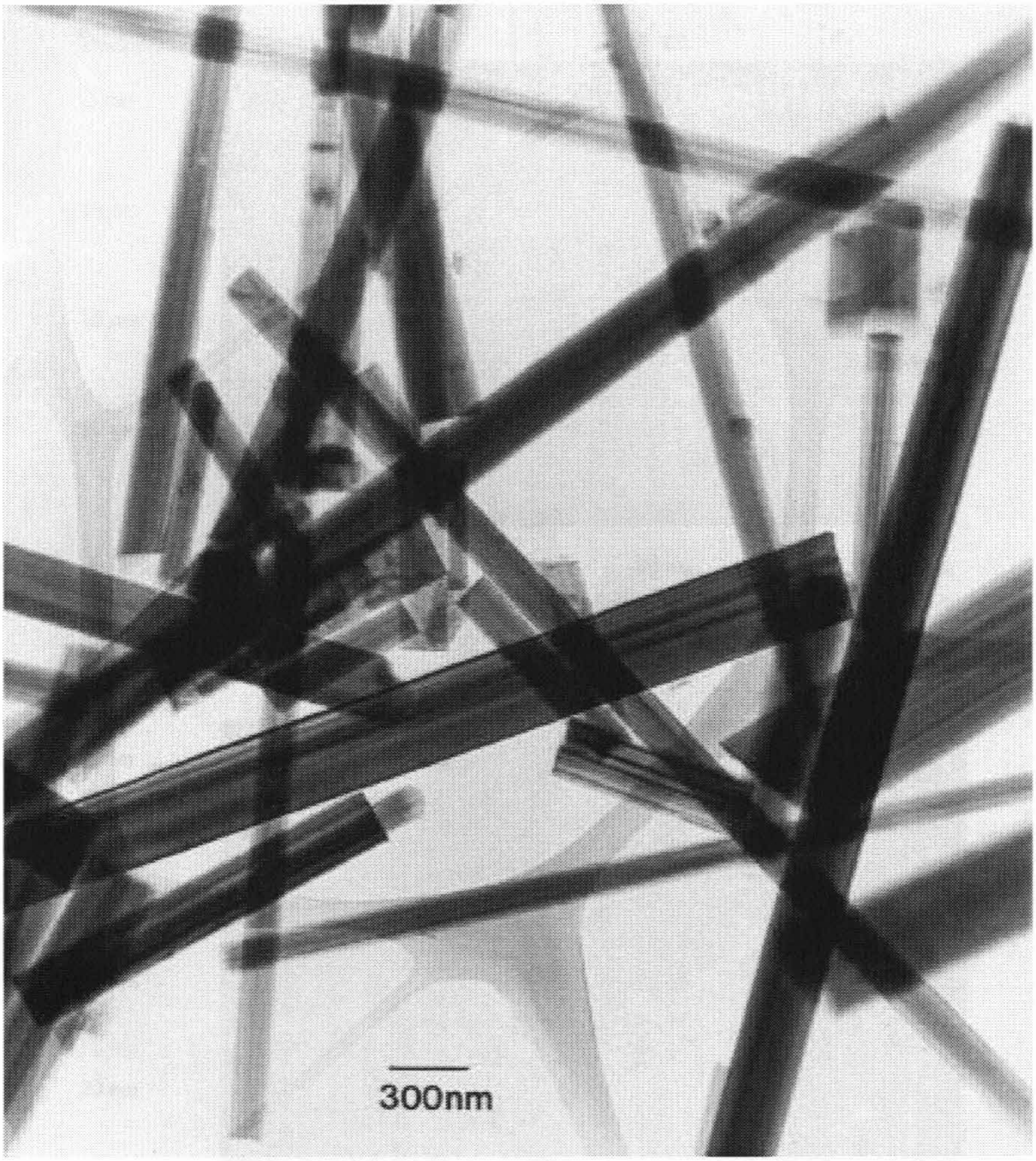

Figure 1

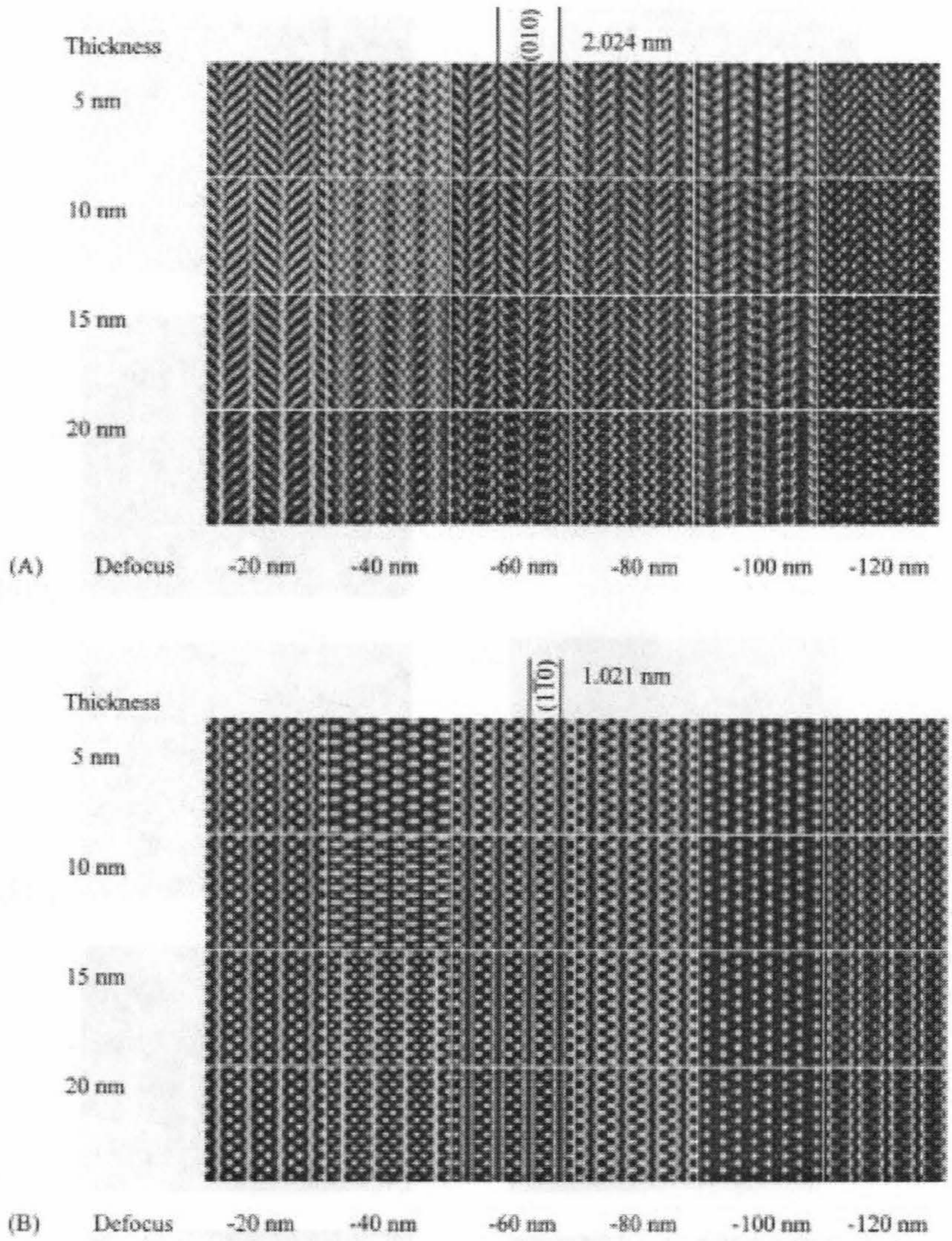
(010)
2.024 nm
Thickness
5 nm
10 nm
15 nm
20 nm
(A)
Defocus
-20 nm
-40 nm
-60 nm
-80 nm
-100 nm
-120 nm
(110)
1.021 nm
Thickness
5 nm
10 nm
15 nm
20 nm
(B)
Defocus
-20 nm
-40 nm
-60 nm
-80 nm
-100 nm
-120 nm

Figure 2

Figure 3 (A) Fiber (B) Dumortierite

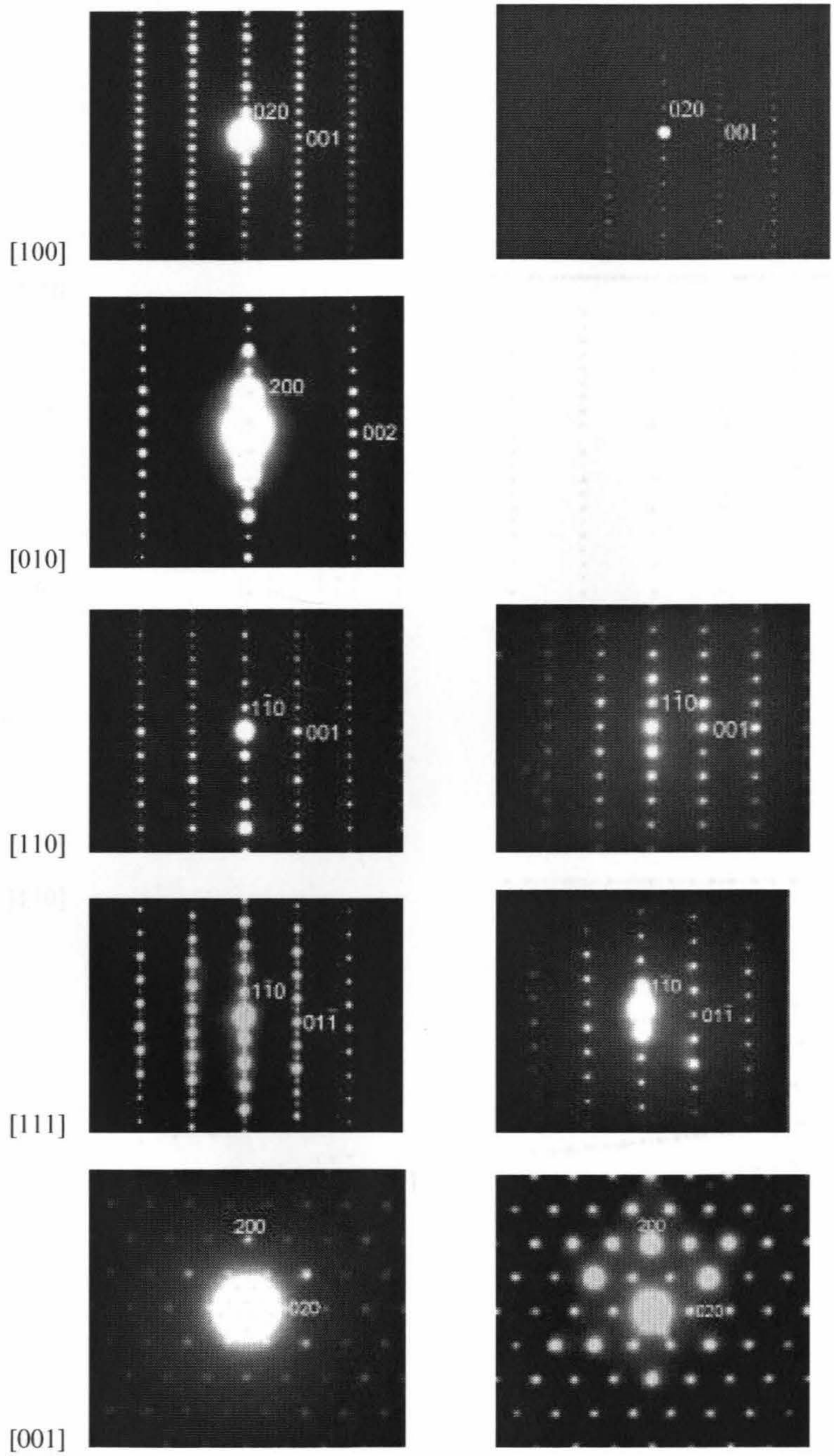

Figure 4 (A) Dumortierite (B) Superstructure

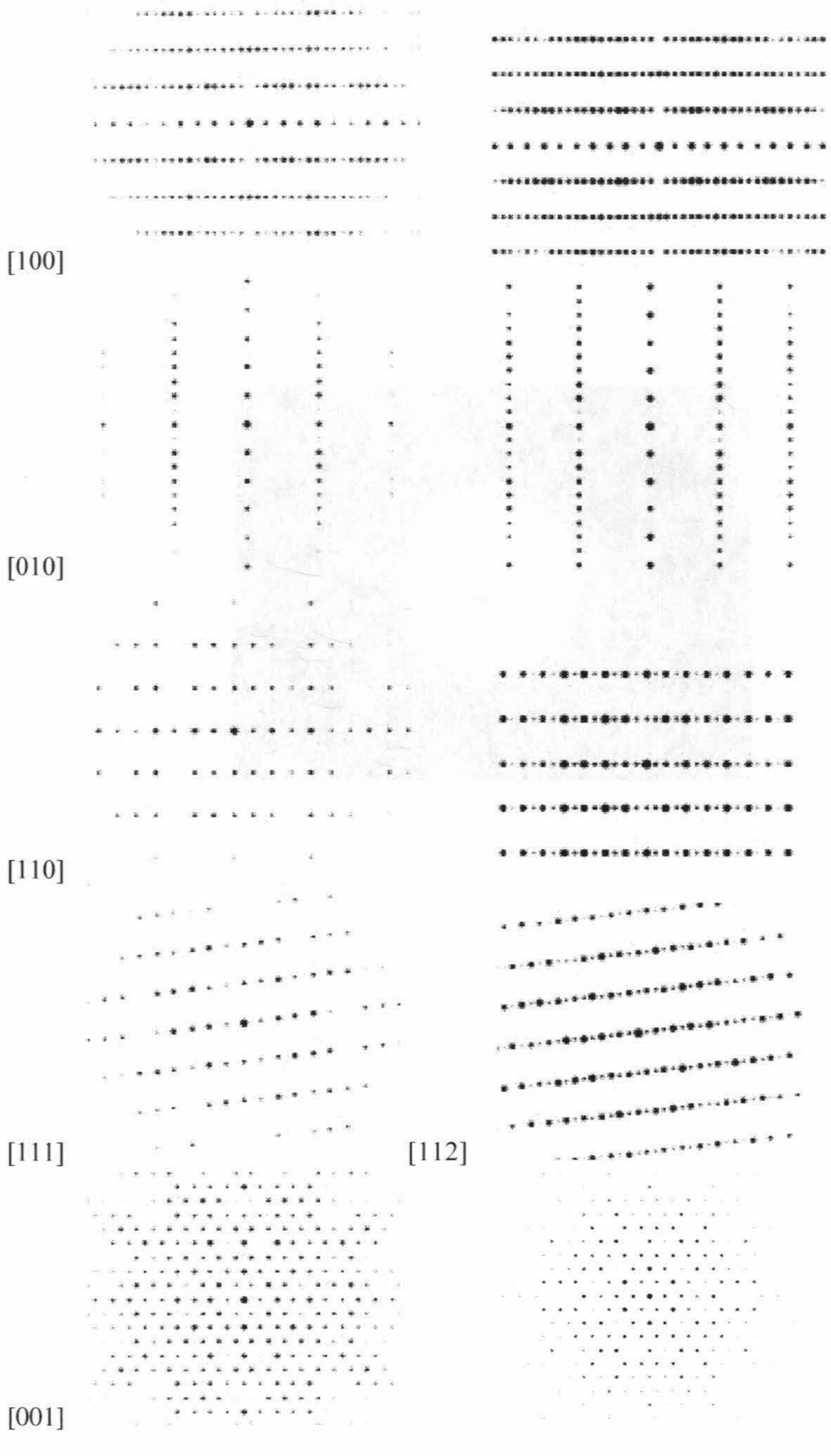

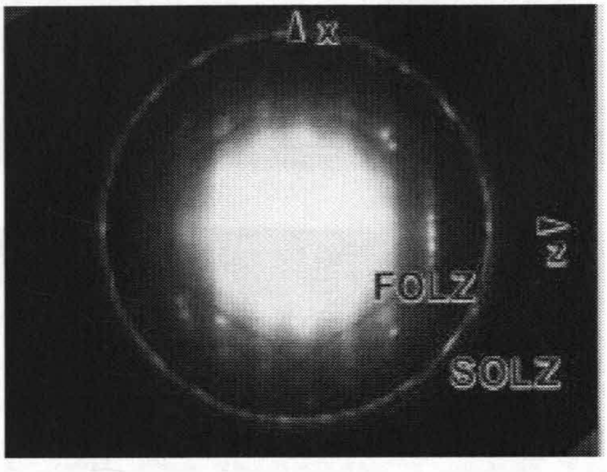

Figure 5

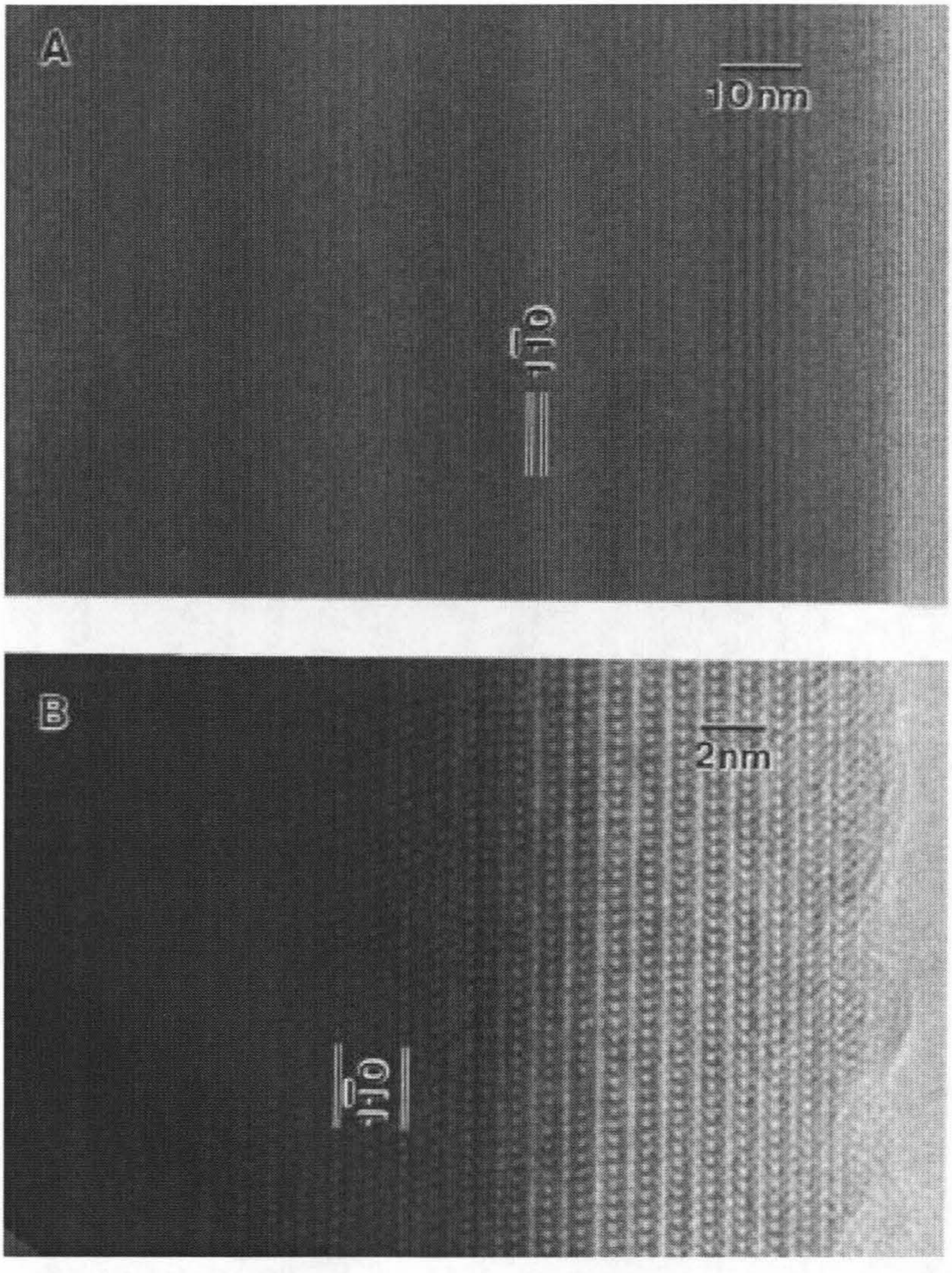

Figure 6

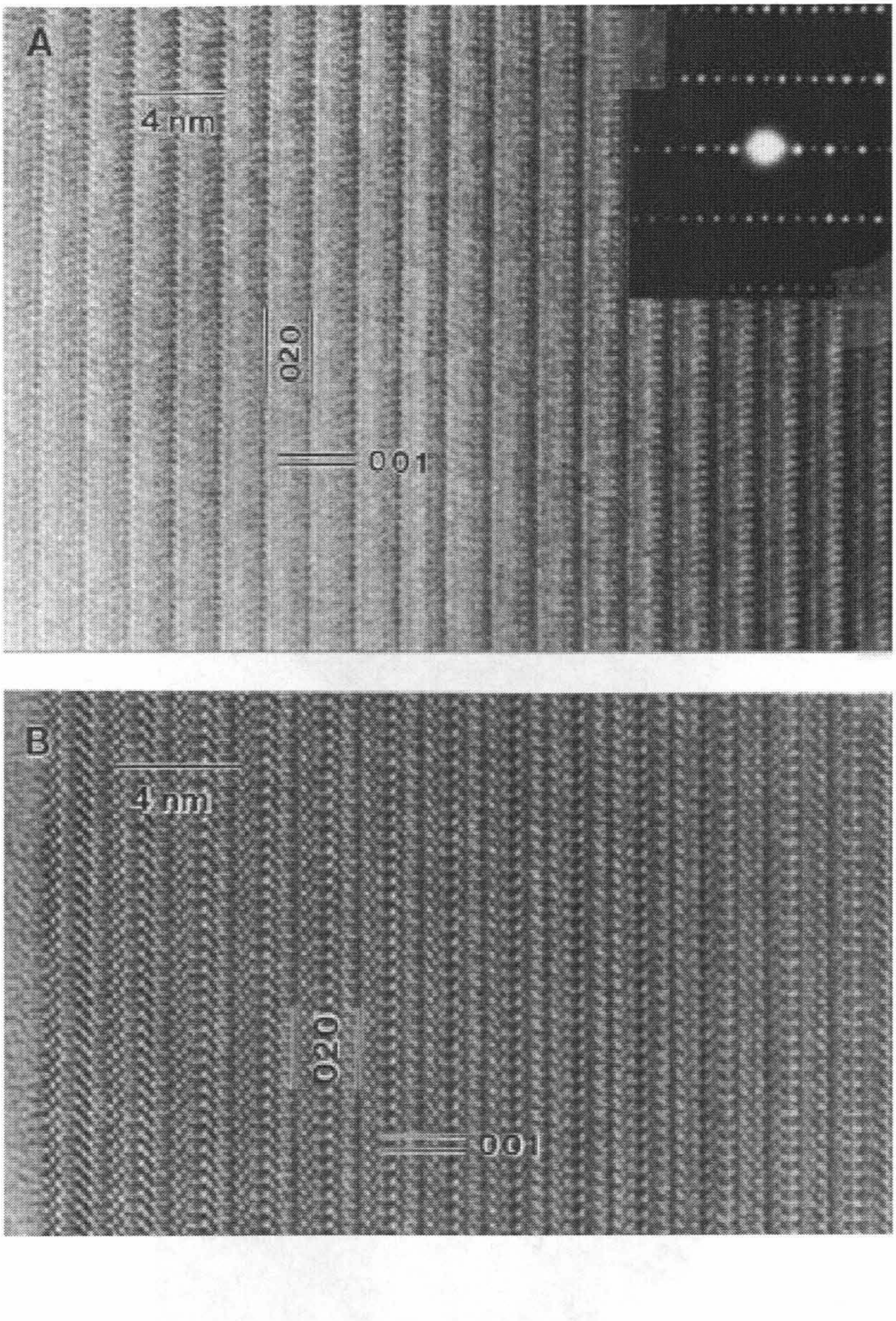

Figure 7

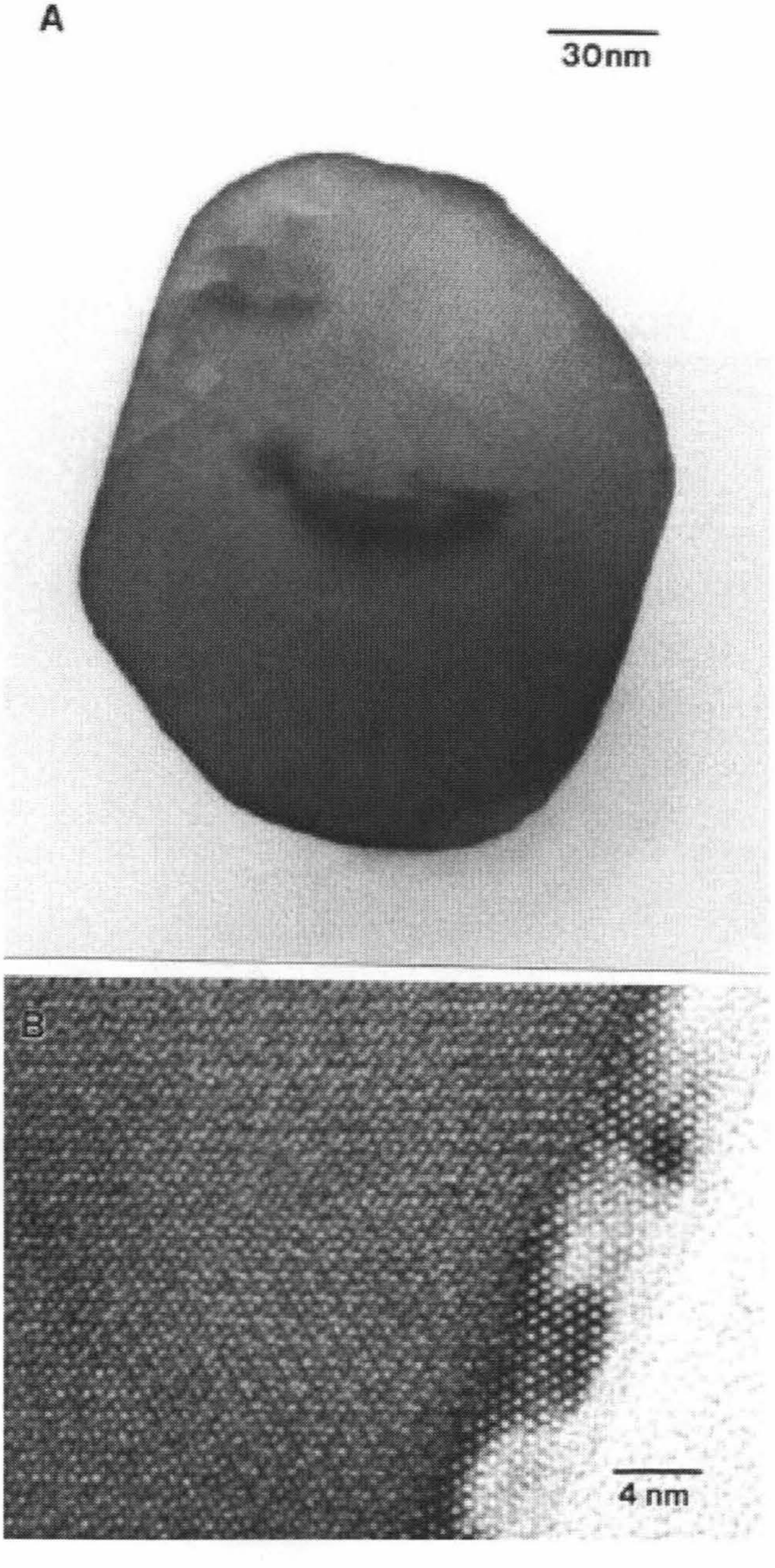

Figure 8

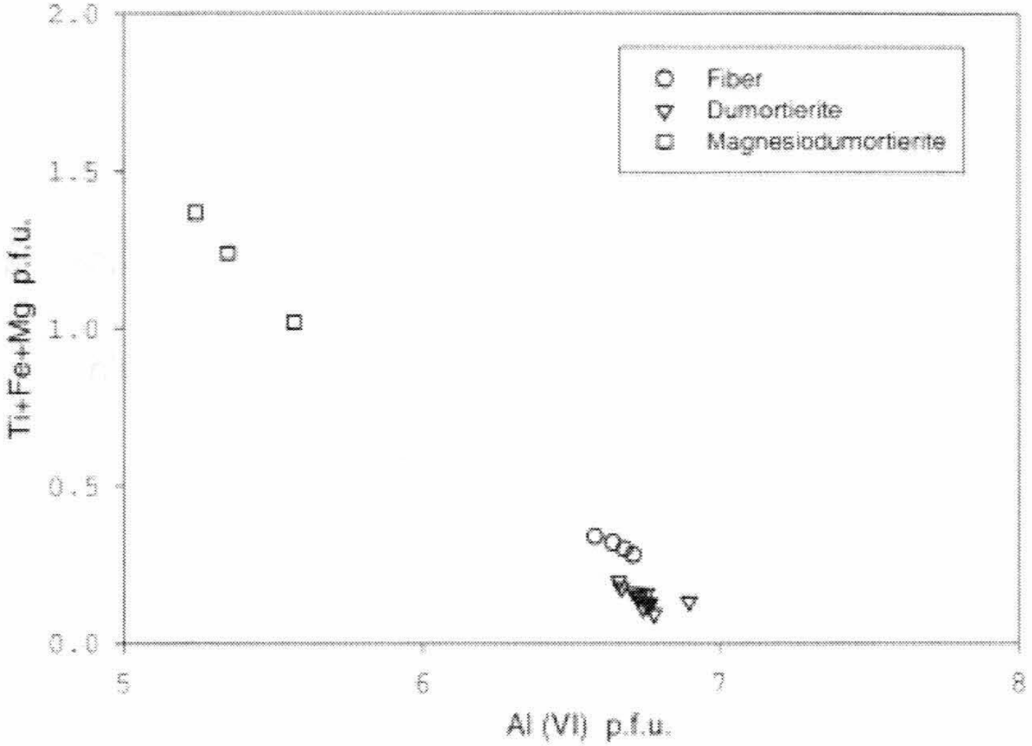
Fiber
Dumortierite
Magnesiodumortierite
Ti+Fe+Mg p.f.u.
Al (VI) p.f.u.
2.0
1.5
1.0
0.5
0.0
5
6
7
8

Figure 9

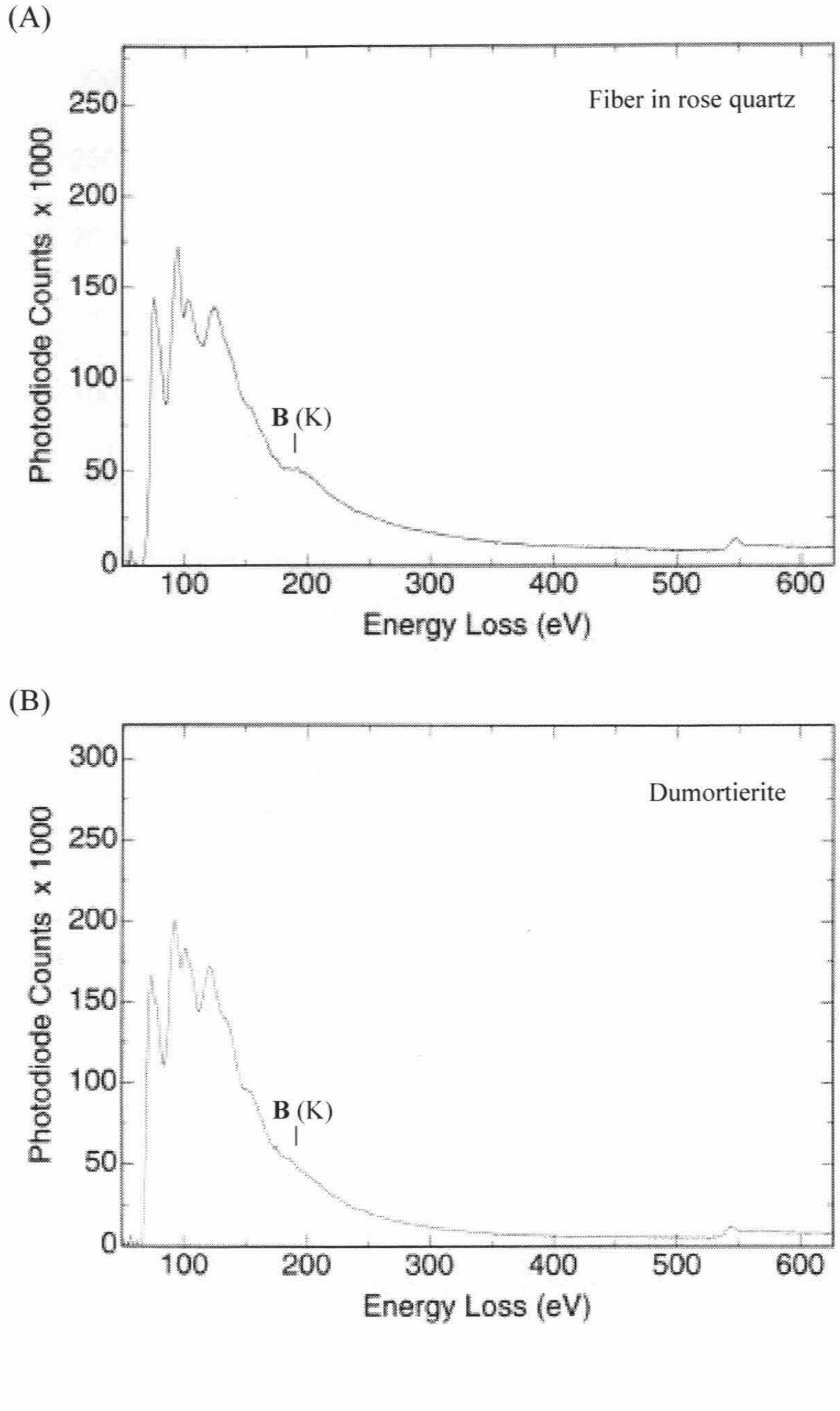
(A)
Fiber in rose quartz
B (K)
Photodiode Counts x 1000
0
50
100
150
200
250
100
200
300
400
500
600
Energy Loss (eV)
(B)
Dumortierite
B (K)
Photodiode Counts x 1000
0
50
100
150
200
250
300
100
200
300
400
500
600
Energy Loss (eV)

Figure 10a,b

(C)

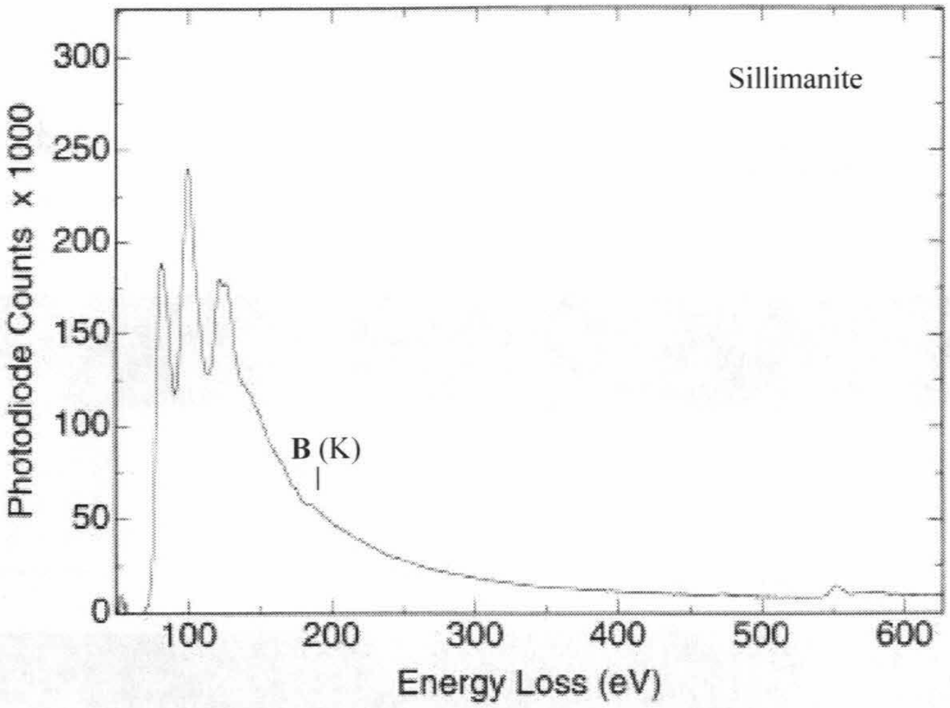
Sillimanite
B (K)
Photodiode Counts x 1000
0
50
100
150
200
250
300
100
200
300
400
500
600
Energy Loss (eV)

Figure 10c

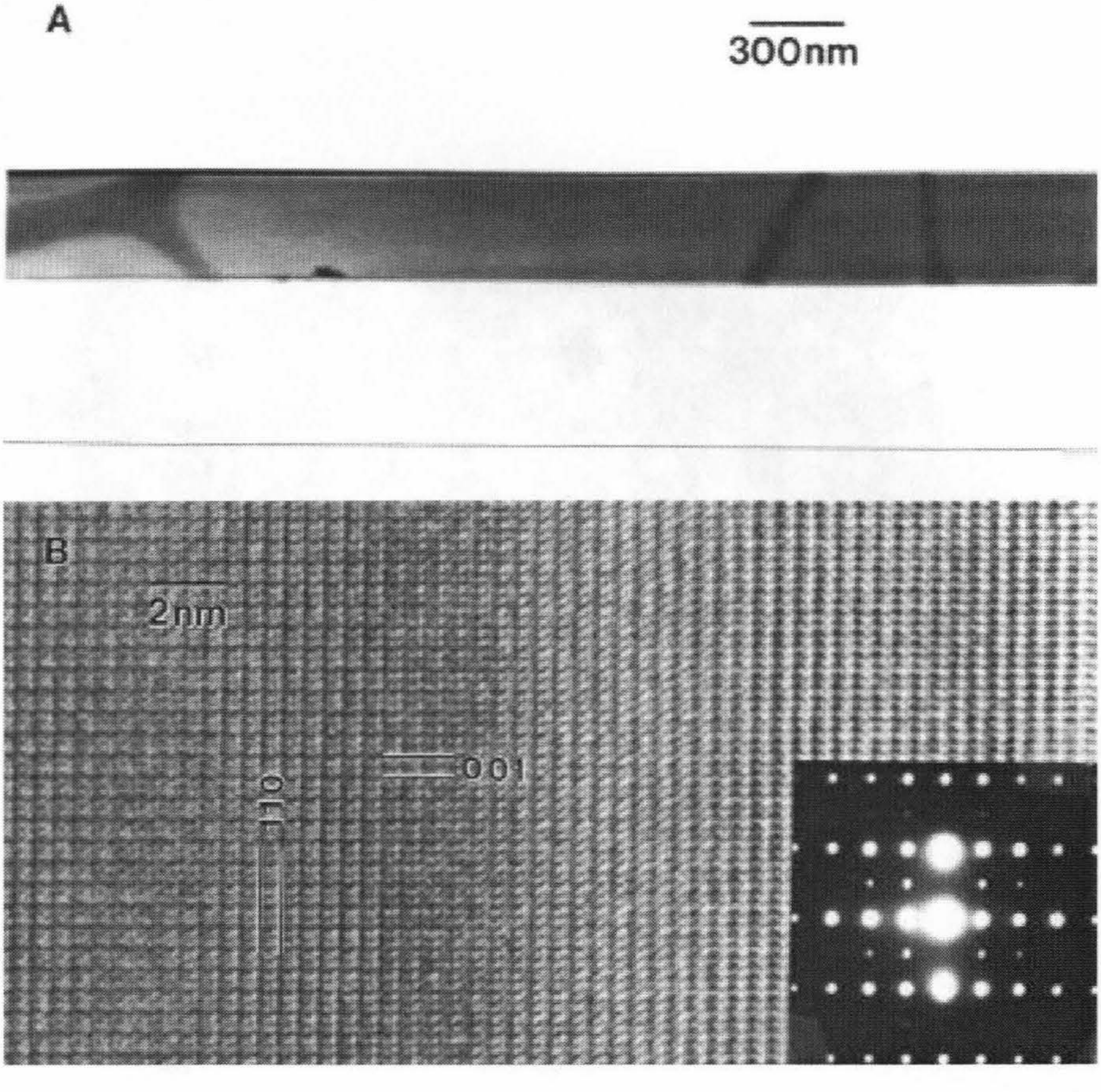

Figure 11

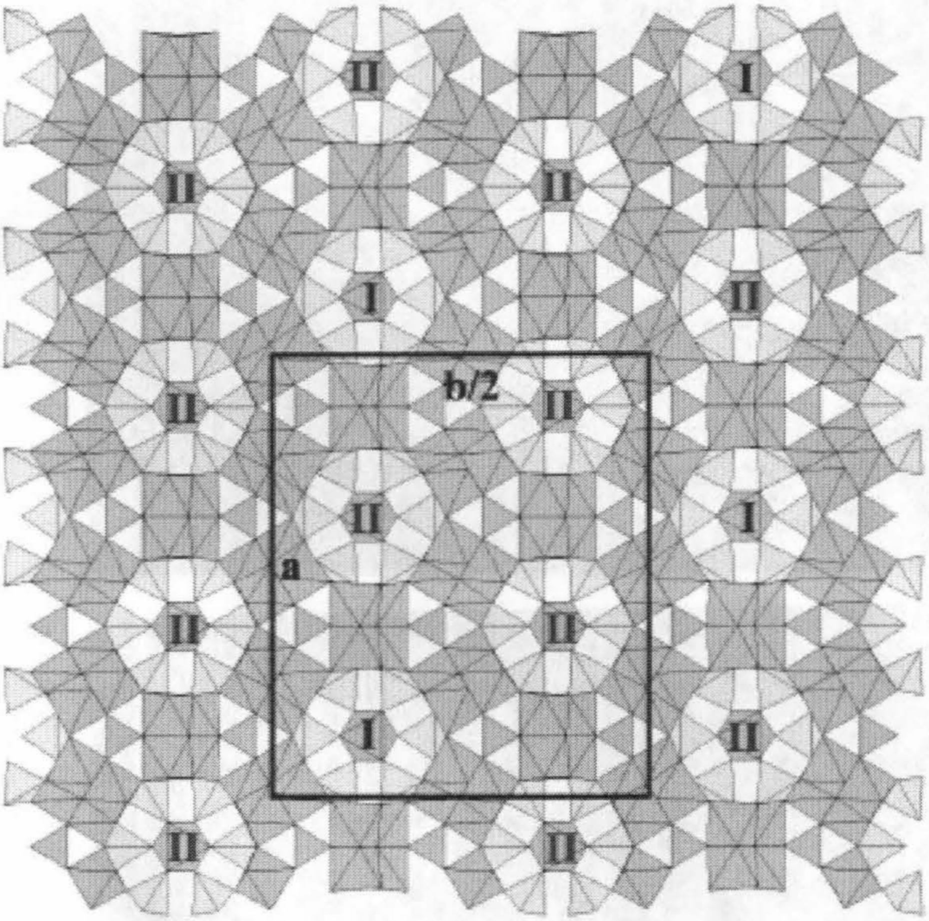

Figure 12

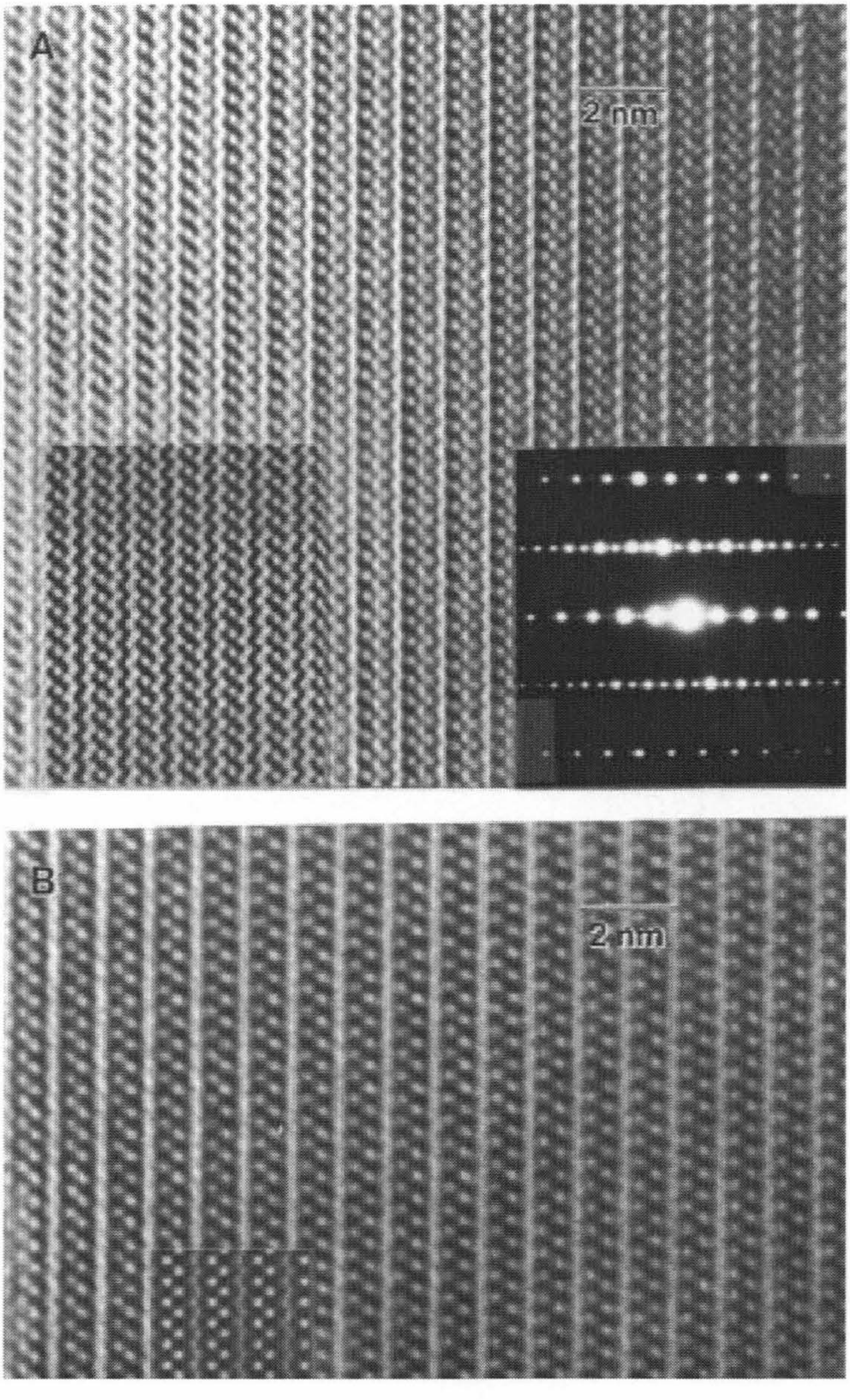

Figure 13